



UNIVERSITÀ DEGLI STUDI DI NAPOLI
“Federico II”

DOTTORATO DI RICERCA IN
FISICA
Ciclo XXXV

Coordinatore: Prof. Vincenzo Canale

**Search for proton decay in Super-Kamiokande and
perspectives in the Hyper-Kamiokande experiments**

Settore Scientifico Disciplinare FIS-01/FIS-04

Dottorando:
Nicola Fulvio Calabria

Tutore:
Prof. Gianfranca De Rosa

ANNI 2019/2022

Contents

1	Physics motivation	1
1.1	The Standard Model of particle physics	1
1.2	Grand Unified Theories	3
1.2.1	Minimal SU(5) GUT	3
1.2.2	SUSY SU(5) GUT	4
1.2.3	SO(10) GUT	5
1.3	Proton decay searches	6
2	The Super-Kamiokande detector	8
2.1	Introduction	8
2.2	Principles of detection	8
2.2.1	Cherenkov effect	9
2.2.2	Photomultiplier tubes	10
2.3	Detector overview	11
2.3.1	SK data taking phases	12
2.3.2	Inner Detector (ID) and Outer Detector (OD)	13
2.3.3	Water and air purification	18
2.3.4	Electronics and data acquisition	19
2.4	ID calibration	22
2.4.1	SK Coordinate axis system	22
2.4.2	Calibration of ID PMTs	23
2.4.3	Water properties measurement	28
2.4.4	PMT and black sheet reflectivity measurement	30
3	SK Data	33
3.1	Official FC reduction process	33
3.1.1	First reduction (FC1)	33
3.1.2	Second reduction (FC2)	34
3.1.3	Third reduction (FC3)	34
3.1.4	Fourth reduction (FC4)	38
3.1.5	Fifth Reduction (FC5)	40

3.1.6	Human eye scan of FC events	41
3.1.7	The final FC cut	42
3.1.8	Generation of the atmospheric neutrino Monte Carlo FC sample	42
3.1.9	Atmospheric neutrino flux	42
3.1.10	Neutrino interactions	43
3.2	Final State Interactions	45
3.2.1	Pion FSI	46
3.3	Detector simulation	47
3.4	Generation of the Proton Decay (PDK) Monte Carlo sample	48
4	Reconstruction algorithms	51
4.1	Introduction: <i>APFit</i> and <i>fiTQun</i>	51
4.2	<i>APFit</i>	52
4.2.1	Vertex fitting	52
4.2.2	Ring counting	54
4.2.3	Particle Identification (PID)	56
4.2.4	Momentum determination	61
4.2.5	<i>Michel electron</i> search	61
4.3	<i>fiTQun</i>	61
4.3.1	The likelihood function	62
4.3.2	Predicted charge	63
4.3.3	Unhit probability	68
4.3.4	Charge likelihood	68
4.3.5	Time likelihood	69
4.3.6	Vertex pre-fitting	69
4.3.7	Hit clustering	70
4.3.8	Single-ring fitter	71
4.3.9	Multi-ring fitter	74
4.4	Performance comparison between <i>APFit</i> and <i>fiTQun</i>	78
4.5	Neutron tagging	80
4.5.1	Neutron tagging algorithm	80
5	Search for $p \rightarrow \nu K^+$ in SK-IV using <i>fiTQun</i>	83
5.1	Simulated samples used	83
5.2	Proton decay mode	83
5.2.1	Decay kinematics	84
5.2.2	Definition of visible energy	85
5.3	Event selections	86
5.4	Distributions along cut parameters	86
5.4.1	Number of reconstructed rings distributions	87

5.4.2	Number of reconstructed e-like rings distributions . . .	87
5.4.3	Tagged <i>Michel electrons</i> distributions	88
5.4.4	Reconstructed π^0 mass and momentum distributions .	88
5.4.5	Reconstructed π^+ momentum distributions	89
5.4.6	Reconstructed K^+ mass and momentum distributions .	90
5.4.7	Number of tagged neutrons	90
5.5	Results	91
5.5.1	Remaining background events	93
5.5.2	Sideband check	97
5.6	Estimation of systematic error	97
5.6.1	Physics model uncertainties for signal efficiency	98
5.6.2	Physics model uncertainties for remaining background .	105
5.6.3	Detector uncertainties	107
5.6.4	Hybrid sample	110
5.6.5	Summary of systematic errors	118
5.7	Lifetime limit calculation	119
5.8	Conclusions and perspectives	122
6	Perspectives: Hyper-Kamiokande	123
6.1	Detector overview	123
6.1.1	Water tank	124
6.1.2	Water purification and circulation system	125
6.1.3	Inner Detector (ID)	127
6.1.4	Outer Detector (OD)	130
6.1.5	Electronics	130
6.1.6	DAQ	132
6.2	HK data	133
6.2.1	Proton decay kinematics	133
6.2.2	Proton decay event generation	134
6.2.3	Detector simulation	136
6.2.4	Reconstruction	137
6.3	First study: fitQun performance	138
6.3.1	Event selections	139
6.3.2	Distributions along cut parameters	139
6.3.3	Results	141
6.4	Second study: tuning of fitQun ring counting for proton decay	143
6.4.1	Manual check of ring correction	145
6.4.2	Results	146

Introduction

The Standard Model of particle physics (SM) is an incredibly successful theory which describes how all known particles interact with each other via electromagnetic, strong and weak forces, leaving gravitational force out. However, several experimental hints pointing at physics beyond the SM have been discovered, leading to the development of Grand Unification Theories (GUTs) of which the SM is a subgroup. While protons in the SM are described as stable, this constraint is absent in GUTs: the search for proton decay is an excellent test to rule out and lead the development of new theories based on experimental lifetime limits or, hopefully, direct observation of the event. Protons are estimated to have an average lifetime of up to 10^{33-34} years: proton decays are expected to be extremely rare events requiring a large amount of protons and a low noise environment to be detected, such as the Super-Kamiokande and Hyper-Kamiokande water Cherenkov detectors. In this thesis we search for $p \rightarrow \nu K^+$ proton decay by looking at the kaon decay products $\pi^+\pi^0$ in water in Super-Kamiokande. Chapter 1 describes the physics theory behind the search, Chapter 2 describes the Super-Kamiokande detector, Chapter 3 describes data reduction and simulation process, Chapter 4 describes reconstruction algorithms and Chapter 5 reports the actual search in the full span of SK-IV (3244.4 days) real data. We took advantage of the π^+ fitter included in the reconstruction algorithm *fiTQun* to reconstruct the kaon kinematics and achieve a low-background search. Furthermore, we built a control sample to evaluate detector systematic error using the hybrid technique, generating events from real data merged with simulated data. Finally, in Chapter 6 we describe the perspectives in Hyper-Kamiokande and two preliminary studies to evaluate *fiTQun* performance and ring counting tuning with $p \rightarrow e^+\pi^0$ search.

Chapter 1

Physics motivation

1.1 The Standard Model of particle physics

The Standard Model (SM) of particle physics is a quantum field theory based on the gauge symmetry group

$$SU(3)_C \times SU(2)_L \times U(1)_Y \quad (1.1)$$

with three generations of fermions, and a scalar Higgs boson: the $SU(3)$ part describes strong interactions carried by eight gauge bosons ($G_{1\sim 8}$ known as *gluons*) while the $SU(2)_L \times U(1)_Y$ describes electro-weak interactions mediated by four gauge bosons ($W_{1\sim 3}$ and B).

As stated by Noether's theorem, each of these symmetries has an associated conserved quantity: $SU(3)_C$ conserves color charge, $SU(2)_L$ conserves the third component of weak isospin (T_3) and $U(1)_Y$ conserves weak hypercharge (Y).

The matter content is divided in *quarks* which interact strongly and *leptons* which don't. We can further classify the SM fermions by weak isospin, as doublets and singlets and their hypercharge Y (Table 1.1). The L and R subscripts stand for left and right handed chirality states respectively.

All of the SM particles enter the theory as massless: the W^\pm and Z^0 bosons and all fermions, with the exception of neutrinos, acquire their mass via the Higgs mechanism after the spontaneous breaking of the electro-weak symmetry $SU(2)_L \times U(1)_Y$ into the electromagnetic gauge symmetry $U_{EM}(1)$, which is associated to the conservation of the electric charge Q . The following relation is valid:

$$Y = 2Q - 2T_3 \quad (1.2)$$

The SM is a very successful theory: in summer 2012 its missing piece, the Higgs boson, was discovered by the ATLAS [8] and CMS [21] experiments.

Table 1.1: SM fermion generations by weak isospin T and hypercharge Y .

(T, Y)	quarks			leptons	
	$(1/2, 1/3)$	$(0, 4/3)$	$(0, -2/3)$	$(1/2, -1)$	$(0, -2)$
I generation	$\begin{pmatrix} u \\ d \end{pmatrix}_L$	u_R	d_R	$\begin{pmatrix} \nu_e \\ e^- \end{pmatrix}_L$	e_R^-
II generation	$\begin{pmatrix} c \\ s \end{pmatrix}_L$	c_R	s_R	$\begin{pmatrix} \nu_\mu \\ \mu^- \end{pmatrix}_L$	μ_R^-
III generation	$\begin{pmatrix} t \\ b \end{pmatrix}_L$	t_R	b_R	$\begin{pmatrix} \nu_\tau \\ \tau^- \end{pmatrix}_L$	τ_R^-

But there are many unresolved issues that suggest that there is physics beyond the SM, such as:

- neutrinos cannot gain mass via the Higgs mechanism but we know from neutrino oscillations [32] [29] [28] that they are massive;
- the SM does not include a description of gravity;
- there are no suitable dark matter candidates in the SM;
- the SM doesn't provide an explanation to the baryon asymmetry of the Universe. Understanding the origin of baryon (B) and lepton (L) number violation is crucial to explain the origin of neutrino masses, the mechanism for the matter-antimatter asymmetry in the Universe and possible baryon and lepton number violating processes;
- the SM doesn't explain the values of the electric charges of quarks and leptons.

Finally, the values of the three running coupling constants in the SM get closer to each other in a very high energy region $> 10^{14}$ GeV, suggesting that there is a larger gauge group which is approximated by the SM group in a low energy limit. Such models are called Grand Unified Theories (GUTs).

1.2 Grand Unified Theories

Grand Unified Theories are extensions of the SM: they predict a single coupling constant for all three interactions at energies $\sim 10^{16}$ GeV (GUT scale). GUT models incorporate quarks and leptons into common multiplets: they predict proton decay as a direct transition between quarks and leptons and consequently, the unification of interactions and unification of quark and lepton, thus with the possibility of transition from quark to lepton, that violates baryon and lepton numbers. Proton decay features the violation of baryon number, thus it is a fundamental test and source of information for GUT theories. Several GUT models based on different gauge symmetries have been proposed, here we list those relevant for this thesis.

1.2.1 Minimal SU(5) GUT

The minimal choice for unification is $SU(5)$ [34]: it's the smallest group that can contain $SU(3) \times U(1)$ as a subgroup. $SU(5)$ has 24 generators, so 12 new gauge bosons (X and Y) are required in addition to those of the SM. Each generation of fermions in $SU(5)$ and gauge bosons have $\mathbf{10} + \bar{\mathbf{5}}$ and $\mathbf{24}$ representations respectively:

$$\bar{\mathbf{5}} : \begin{pmatrix} d_1^c \\ d_2^c \\ d_3^c \\ e \\ -\nu_e \end{pmatrix}, \quad \mathbf{10} : \begin{pmatrix} 0 & u_3^c & -u_2^c & u_1 & d_1 \\ u_3^c & 0 & u_1^c & u_2 & d_2 \\ u_2^c & -u_1^c & 0 & u_3 & d_3 \\ -u_1 & -u_2 & -u_3 & 0 & e^c \\ -d_1 & -d_2 & -d_3 & -e^c & 0 \end{pmatrix} \quad (1.3)$$

where 1, 2, 3 are the color charge indexes and c is charge conjugation, and

$$\mathbf{24} : \begin{pmatrix} G_1^1 - \frac{2B}{\sqrt{30}} & G_2^1 & G_3^1 & \bar{X}_1 & \bar{Y}_1 \\ G_1^2 & G_2^2 - \frac{2B}{\sqrt{30}} & G_3^2 & \bar{X}_2 & \bar{Y}_2 \\ G_1^3 & G_2^3 & G_3^3 - \frac{2B}{\sqrt{30}} & \bar{X}_3 & \bar{Y}_3 \\ X^1 & X^2 & X^3 & \frac{W^3}{\sqrt{2}} + \frac{3B}{\sqrt{30}} & W^+ \\ Y^1 & Y^2 & Y^3 & W^- & -\frac{W^3}{\sqrt{2}} + \frac{3B}{\sqrt{30}} \end{pmatrix} \quad (1.4)$$

where G , W and B are the SM gauge bosons. The charge operator Q is traceless, since it's a linear combination of generators which are traceless, then this model can explain electric charge quantization as follows:

$$\sum_{a=1}^5 Q_a = 3Q_{d^c} + Q_e + Q_{\nu_e} = 0 \quad \rightarrow \quad Q_d = -Q_{d^c} = -\frac{1}{3} \quad (1.5)$$

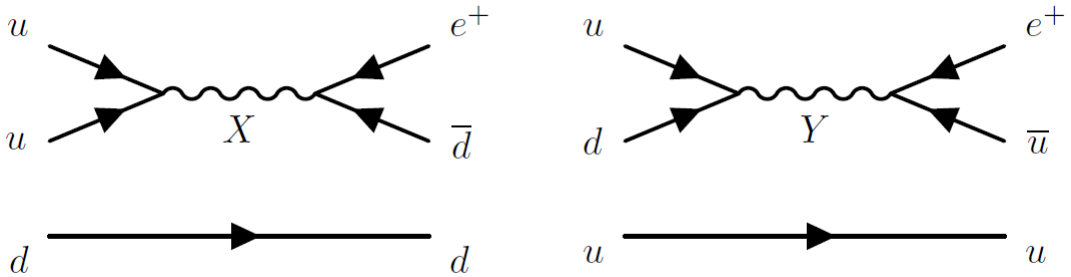


Figure 1.1: Feynman diagrams of proton decay $p \rightarrow e^+ \pi^0$ via X (on the left) and Y (on the right) bosons.

The predicted dominant proton decay mode is $p \rightarrow e^+ \pi^0$ (Figure 1.1) with a partial lifetime $\tau/B(p \rightarrow e^+ \pi^0) \sim 10^{31 \pm 1}$ years, already excluded by several experiments [26] [27] [31] [30]. This model predicts a value for $\sin^2(\theta_W) = 3/8$, where θ_W is the Weinberg angle but this value is excluded by experiments as well [45].

Notably, this model also fails to explain neutrino masses since no right-handed neutrino helicity state is contained.

1.2.2 SUSY SU(5) GUT

This model introduces into the SU(5) model a symmetry between fermions and bosons, known as *SUper-SYmmetry* (SUSY). This symmetry associates a super-symmetric partner to each SM particle (Table 1.2). These new particles are expected to exist in a range of masses between 1 and 10 TeV: none of them has been detected so far.

Table 1.2: SM particles and their SUSY partners.

SM particle	Spin	SUSY partner	Spin
q quark	$\frac{1}{2}$	\tilde{q} squark	0
l lepton	$\frac{1}{2}$	\tilde{l} slepton	0
g gluon	1	\tilde{g} gluino	$\frac{1}{2}$
W W boson	1	\tilde{W} wino	$\frac{1}{2}$
Z Z boson	1	\tilde{Z} zino	$\frac{1}{2}$
γ photon	1	$\tilde{\gamma}$ photino	$\frac{1}{2}$
H higgs	0	\tilde{H} higgsino	$\frac{1}{2}$

In this model the three running coupling constants can match at around

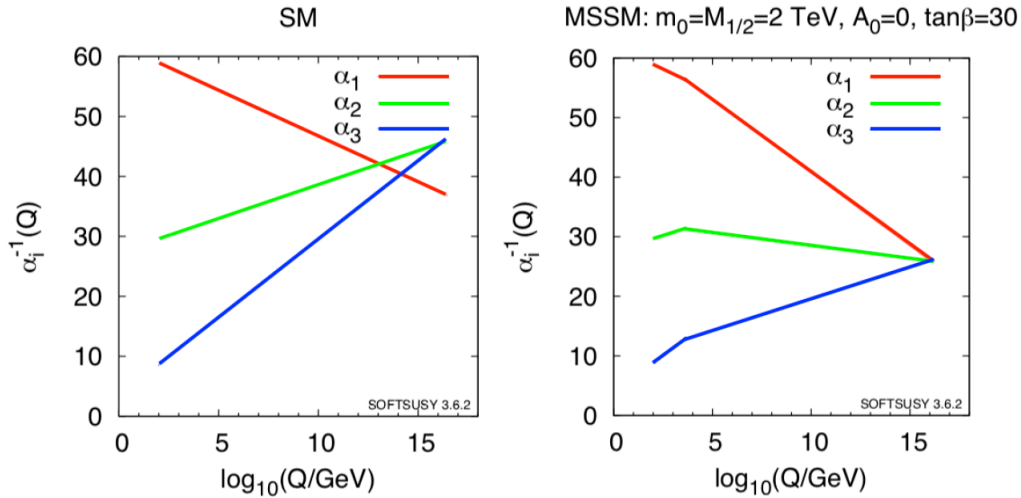


Figure 1.2: Inverse of the running coupling constants in SM (left) and Minimal Susy Standard Model (MSSM) (right) as a function of the logarithm of the energy scale. Taken from [60].

2×10^{16} GeV (Figure 1.2) [24] [44] [39].

In the minimal SUSY SU(5) mode the predicted dominant proton decay mode is $p \rightarrow \nu K^+$ (Figure 1.3), mediated by SUSY particles, with a predicted partial lifetime $< 2.9 \times 10^{30}$ years: this model is excluded by Super-Kamiokande results [51].

1.2.3 SO(10) GUT

The SO(10) GUT model can explain neutrino masses via the *seesaw* mechanism, by including a right-handed neutrino [49] [64] [47]. All fermions from one generation have a representation $\mathbf{16} = \mathbf{10} + \mathbf{5} + \mathbf{1}$.

Several models can be implemented, with different symmetry breaking patterns and with or without SUSY.

The predicted dominant decay mode in SO(10) GUT is $p \rightarrow e^+ \pi^0$ with a lifetime in the range $10^{32} - 10^{39}$ years [53] [4].

SUSY GUTs based on SO(10) [43] [46], together with non-minimal SUSY SU(5) GUTs [42], are interesting because they predict partial lifetimes for $p \rightarrow \nu K^+$ in the range of 10^{32} to 10^{35} years which are still under experimental investigation.

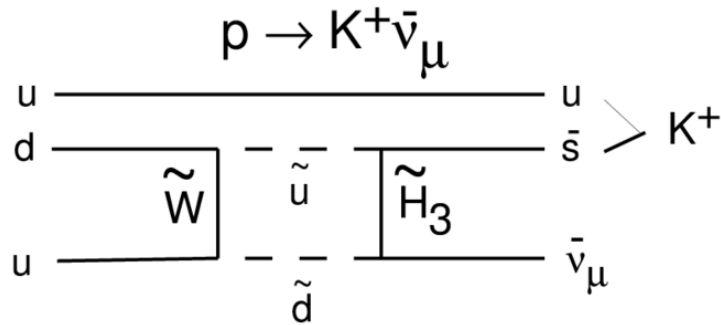


Figure 1.3: Diagram of proton decay $p \rightarrow \nu K^+$. In the diagram \tilde{H}_3 stands for color-triplet higgsino.

1.3 Proton decay searches

Historically, many attempts to find proton decay have been conducted, some before that SU(5) were formulated in 1974. The first experimental search was performed in 1954 by M. Goldhaber [33], by looking for fission products of Th^{232} induced by proton decay and set a lower lifetime limit of 10^{20} years. Another attempt was made by Reines et al. [33] by looking for particles with kinetic energy above 100 MeV in 300 liters of liquid scintillator at 200 meters of water equivalent depth. The formulation of GUTs guided and motivated new experimental searches: Learned et al. [38] fixed the first partial lower lifetime limit for $p \rightarrow e^+ \pi^0$ at 6×10^{29} years using liquid scintillators placed underground. Figure 1.4 shows proton lifetime predictions according to several theoretical models. Any proton decay search must involve a large sample of protons to improve the probability of occurrence of a proton decay within the time span of the experiment, the experiment must run for a long time, usually years, and its efficiency for proton decay is crucial since only a few events are expected even under the most optimistic assumptions. For these reasons, water Cherenkov detectors are a good choice for proton decay searches: they are relatively easy and cost-effective to scale, since water is cheap and abundant and the progression Kamiokande, Super-Kamiokande and Hyper-Kamiokande confirms this, indeed.

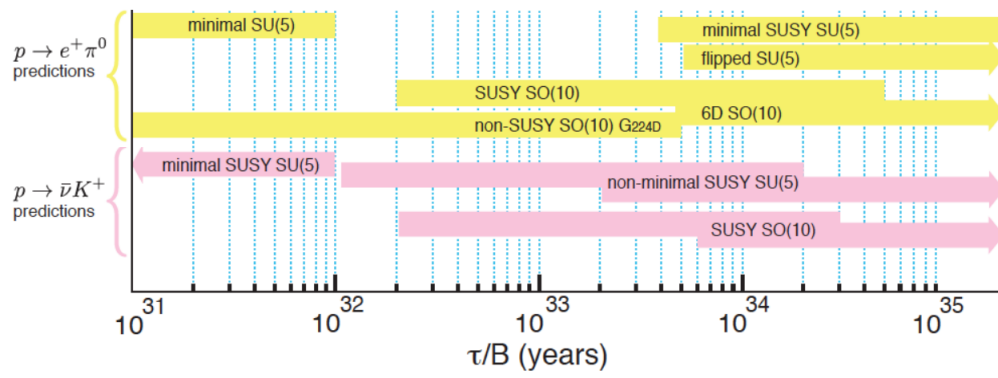


Figure 1.4: Proton lifetime predictions according to several theoretical models.

Chapter 2

The Super-Kamiokande detector

2.1 Introduction

Super-Kamiokande (SK) is the largest underground water Cherenkov detector in the world.

Since its operation begun in 1996, the Super-Kamiokande detector has been successfully improving scientific knowledge in many research fields: it recorded the first unambiguous evidence of atmospheric neutrino oscillations, it confirmed the solar neutrino deficit with real-time neutrino imaging of the Sun, it measured the solar neutrino energy spectrum above 5 MeV for the first time, it set the world's highest lower limits on partial lifetimes for proton decay modes [22].

The detector is managed and operated by the Super-Kamiokande Collaboration, involving 200 people and about 50 institutes from 11 countries of the world, including Italy, supported by the Kamioka Observatory of the Institute of Cosmic Ray Research (ICRR, Tokyo University).

2.2 Principles of detection

Super-Kamiokande is a Cherenkov detector: it's made of about 11000 photomultiplier tubes which look for Cherenkov light produced in water by charged particles that meet their momentum threshold.

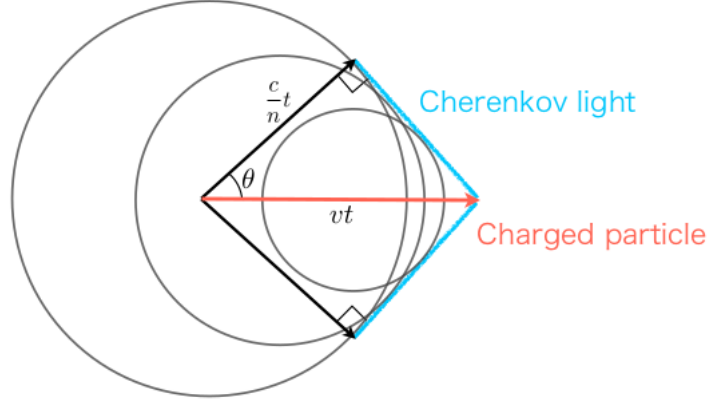


Figure 2.1: Schematic view of the Cherenkov effect.

2.2.1 Cherenkov effect

An electrically charged particle emits light when it travels in a dielectric medium with refractive index n with a velocity $v = \beta c$ greater than the phase velocity of light in that medium $v_p = c/n$. This is known as the *Cherenkov effect* (Pavel A. Cherenkov, Nobel 1958) [3] and the light emitted is known as *Cherenkov light*.

Cherenkov light is emitted in a cone-shaped flash (Figure 2.1) whose vertex lies on the particle track and with an opening angle θ_C with respect to the particle momentum vector. The Cherenkov angle θ_C is given by

$$\cos \theta_C = \frac{1}{n\beta} \quad (2.1)$$

from which we can calculate the threshold β_{th}

$$\frac{1}{n\beta} \leq 1 \implies \beta_{th} = \frac{1}{n} \quad (2.2)$$

The corresponding threshold on momentum p_{th} for a particle with rest mass m_0 is given by:

$$p_{th} = cm_0\beta_{th}\gamma_{th} = cm_0\beta_{th} \frac{1}{\sqrt{1-\beta_{th}^2}} = cm_0 \left[\frac{1}{n} \frac{1}{\sqrt{1-\left(\frac{1}{n}\right)^2}} \right] \quad (2.3)$$

In water n is about 1.34 and for a particle with $\beta \sim 1$ the Cherenkov angle $\theta_C \sim 42^\circ$. Table 2.1 shows momentum thresholds for some relevant charged particles in water.

Table 2.1: Momentum thresholds for various particles in water.

	e	μ	π^\pm	K^\pm	p
Momentum (MeV/c)	0.57	118	156	560	1052

Finally, the number of Cherenkov photons emitted per unit track length x and per wavelength λ is given by

$$\frac{\partial^2 N}{\partial x \partial \lambda} = \frac{2\pi\alpha}{\lambda^2} \left(1 - \frac{1}{n^2\beta^2} \right) \quad (2.4)$$

where α is the fine structure constant. A charged particle traveling at $\beta \sim 1$ in water is expected to produce 340 photons/cm with wavelength between 300 nm and 600 nm.

2.2.2 Photomultiplier tubes

Photomultiplier tubes (PMTs) are vacuum tubes with an internal photocathode, exposed to light through a transparent glass window (Figure 2.2). If an incident photon extracts an electron (*photoelectron*) from the photocathode due to *photoelectric effect* (Albert Einstein, Nobel 1922) [6], it is accelerated and multiplied by a set of dynodes and finally collected by the anode where it produces an electric signal which is digitized and stored by the front-end electronics.

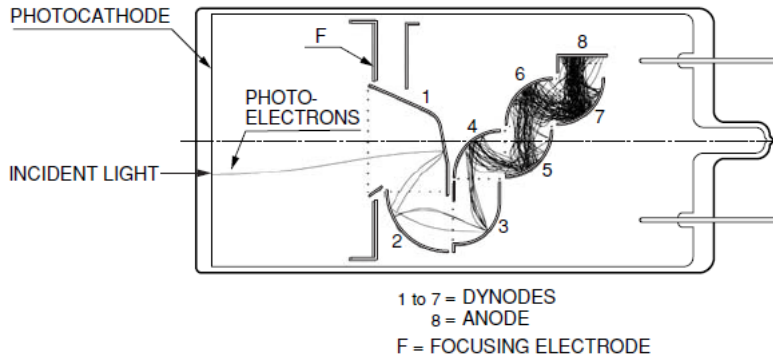


Figure 2.2: Simplified schema of a generic photomultiplier tube.

The output signal amplitude depends linearly from the number of extracted photoelectrons, making the measurement of the produced charge possible.

Characteristic parameters of PMTs

Quantum efficiency is defined as:

$$\text{Quantum Efficiency (Q.E.)} = \frac{\text{number of extracted photoelectrons}}{\text{number of incident photons}} \quad (2.5)$$

This parameter takes into account the failure in the conversion of photons into photoelectrons: incident photons can be blocked by the glass window, photoelectrons can fail their escape from the photocathode and so on. Quantum efficiency is usually given as a function of photon wavelength.

PMTs produce signals even in a perfectly dark environment, named *dark noise*. Some electrons in the conduction band of the photocathode may reach its surface with enough energy to escape from it, mimicking the emission of a photoelectron and contributing to noise: this contribution to noise is known as *thermoionic noise* and it's the major contribution to dark noise.

The signal timing distribution is determined by the differences between the paths each photoelectron has to walk in order to be multiplied and collected: the delay between the incidence of radiation and the peak of the signal is called *transit time*, the full width at half maximum (FWHM) of its distribution is called *transit time spread* (TTS).

2.3 Detector overview

The detector is located about 1000 m (2700 m water equivalent) in the depths of Mt. Ikeno, Kamioka, Japan, in the Mozumi mine, operated by the Kamioka Mining and Smelting Company. It is accessible from the surface via a 1.8 km long tunnel (Atotsu tunnel) or via a mine railway.

The rock surrounding the detector shields it from cosmic ray muons with energy less than 1.3 TeV. The muon flux is $6 \times 10^{-8} \text{ cm}^{-2} \text{ s}^{-1} \text{ sr}^{-1}$ on site, five orders of magnitude less than outside the mountain at sea level.

The detector is an upright self-supporting cylinder, 39.3 m in diameter and 41.4 m in height, made of welded stainless steel and it contains more than 50 kton of ultra-pure light water (H₂O). It is separated in two optically insulated sections: the Inner Detector (ID) and the Outer Detector (OD) (Figure 2.3).

The ID has a diameter of 33.8 m and a height of 36.2 m and it contains 32 kton of water. More than 11000 50-cm PMTs are mounted on its wall, facing inwards and providing about 40% of photocatode coverage.

The OD contains 1885 20-cm PMTs mounted on the outside of the ID wall, behind the ID PMTs and facing outwards.

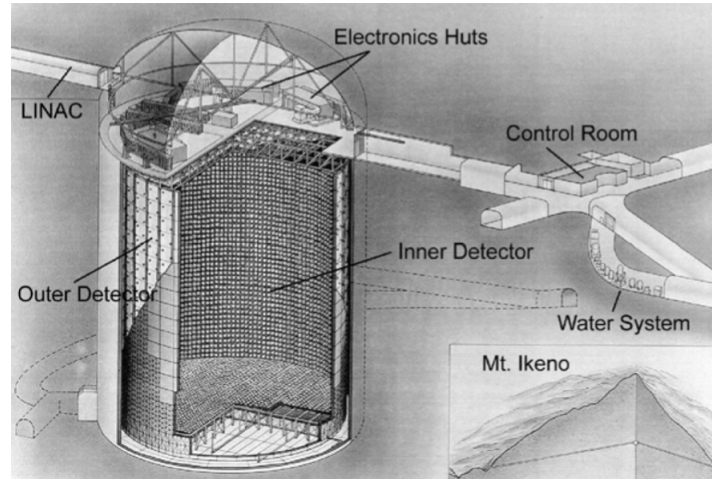


Figure 2.3: The Super-Kamiokande detector.

2.3.1 SK data taking phases

SK data are divided in six phases, each corresponding to a different detector configuration, including upgrades eventually. The first four phases, from SK-I to SK-IV, are summarized in Table 2.2.

Table 2.2: SK epochs.

		SK-I	SK-II	SK-III	SK-IV
Observation	Start	Apr. 1996	Oct. 2002	Jun. 2006	Sep. 2008
	End	Jul. 2001	Oct. 2005	Aug. 2008	May 2018
Live time (days)		1489.2	798.6	518.1	3244.4
Number of PMTs	ID	11146	5182	11129	11129
	OD	1885	1885	1885	1885
Photocathode Coverage		40%	19%	40%	40%
Fiber Reinforced Plastics (FRP) & Acrylic Case		No	Yes	Yes	Yes
Front-end electronics	ID	ATM	ATM	ATM	QBEE
	OD	OD QTC	OD QTC	OD QTC	QBEE
Trigger		Hardware	Hardware	Hardware	Software

In SK-V, some new PMTs that will be used in the Hyper-Kamiokande experiment were installed for testing and the preparation for gadolinium sulfate in water was started. In SK-VI 13.2 tons of gadolinium sulfate octahydrate ($\text{Gd}_2(\text{SO}_4) \cdot 8\text{H}_2\text{O}$) were dissolved in water to improve neutron tagging efficiency [48] while in SK-VII, which is still ongoing (2022), 26 more tons were

dissolved, bringing the concentration of Gd from 0.01% to 0.03%. This analysis has been designed for SK-IV only: we implicitly assume through all this thesis that the detector configuration is SK-IV.

2.3.2 Inner Detector (ID) and Outer Detector (OD)

The boundary between ID and OD is a stainless steel frame structure made of *supermodules* measuring 2.1 m in height, 2.8 m in width and 0.55 m in thickness. Each supermodule hosts 12 ID PMTs in a 3×4 layout on its inner side and 2 OD PMTs on its outer side (Figure 2.4).

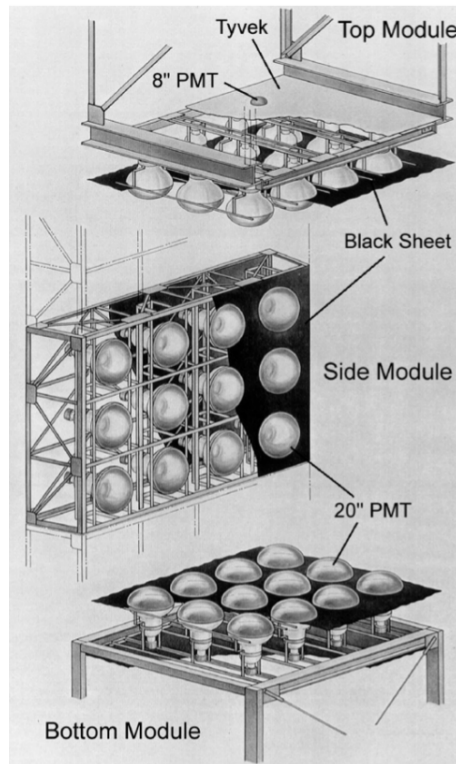


Figure 2.4: Schematic view of supermodules mounted inside the tank.

Opaque black polyethylene terephthalate (PET) sheets cover the gaps between the ID PMTs: they provide optical insulation between the ID and the OD space and improve event reconstruction by reducing indirect light inside the tank. A wavelength shifting plate is attached to each OD PMT and the OD volume is covered by reflective Tyvek sheets to improve light collection and classification efficiency of background events from penetrating particles like cosmic-ray muons and the products of radioactive decays from the detector surroundings.

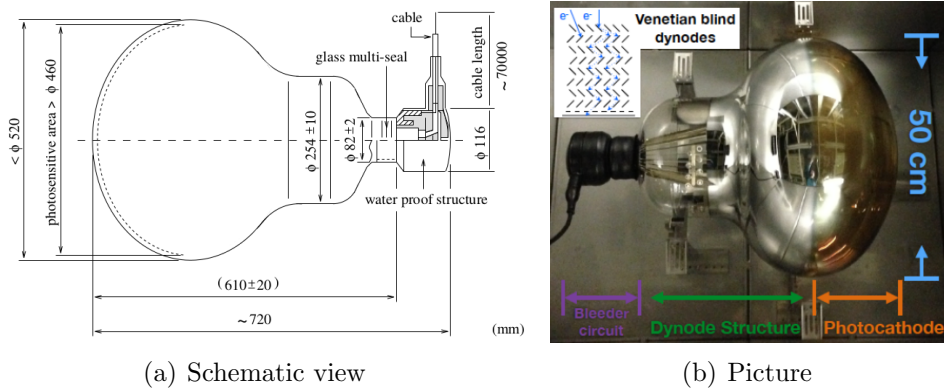


Figure 2.5: Hamamatsu R3600 photomultiplier tube.

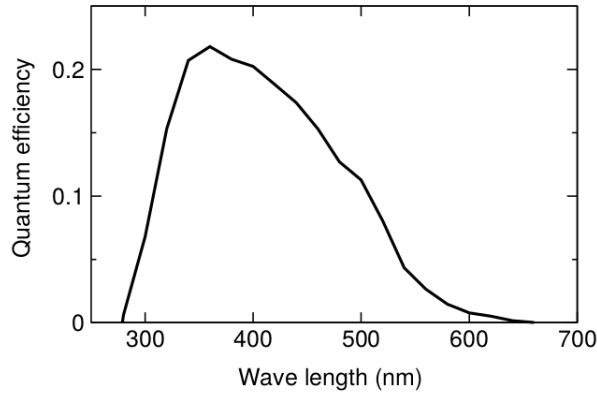


Figure 2.6: Quantum efficiency of an ID PMT as a function of wavelength.

ID PMTs

The ID wall hosts Hamamatsu R3600 50 cm PMTs: their dynode structure is a Venetian-blind type with 11 stages [7] (Figure 2.5(a)).

They have a bialkali (Sb-K-Cs) photocathode with a peak quantum efficiency of about 21% at 360-400 nm (Figure 2.6).

The collection efficiency for photoelectrons (pe) at the first dynode is over 70%. The transit time spread for a 1 pe signal is 2.2 ns (Figures 2.7 and 2.8). The average dark noise rate at 0.25 pe threshold used in SK is about 3 kHz. All figures and results are from [22].

The ID PMTs are fed with high voltage ranging from 1700 to 2000 V, corresponding to a gain of 10^7 . The neck of each PMT is coated with a silver reflector to block external light: anyway this doesn't prevent light from entering through the back of the hemispherical portion of the PMT

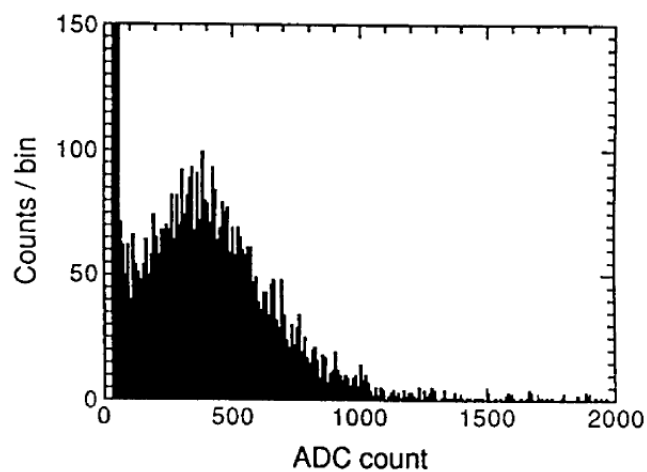


Figure 2.7: Single photoelectron pulse height distribution. The peak close to zero ADC count is due to PMT dark current.

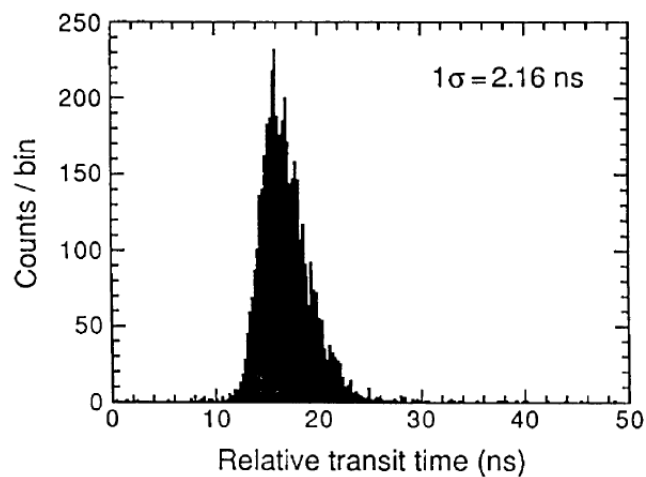


Figure 2.8: Relative transit time distribution for a typical PMT tested with 410 nm wavelength light at the single photoelectron intensity level.

(Figure 2.5(b)).

Fiber Reinforced Plastics (FRP) and Acrylic Cases

During the maintenance phase at the end of SK-I, about 60% of all ID PMTs happened to be destroyed in an accident. One ID PMT of the bottom sector imploded during the tank refilling process, producing a shockwave propagating inside the whole tank, causing a chain implosion of ID and OD PMTs, as well. As a temporary fix, the remaining PMTs were redistributed on the ID wall in order to ensure a suitable coverage for the incoming SK-II epoch. Broken OD PMTs were replaced. Before the beginning of SK-III, new ID PMTs were installed to restore the original coverage but in order to prevent new implosions all the PMTs were sealed inside a container consisting of two parts: the back one made of Fiber Reinforced Plastics (FRP), the front one of transparent acrylic (Figure 2.9).

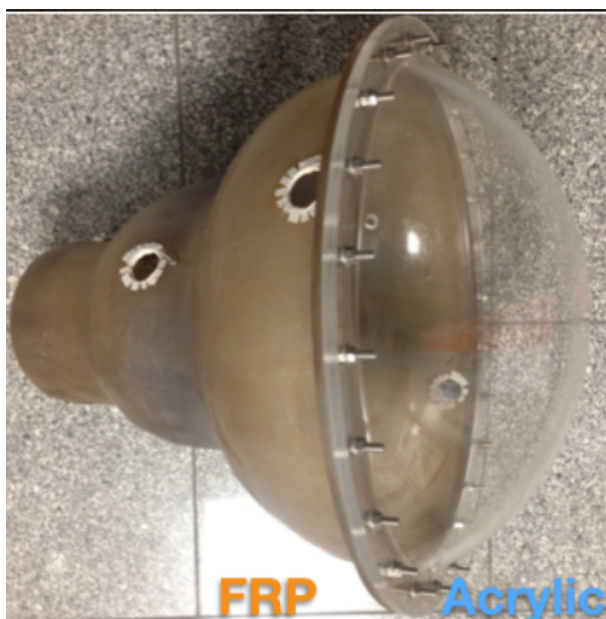


Figure 2.9: The FRB (left) and transparent acrylic parts (right) combined together to provide the sealed reinforcement case for the ID PMTs specifically designed to prevent accidental implosions.

The front acrylic cover brings two undesired effects: it reduces the amount of light reaching the photocathode and increases the amount of reflections inside the tank but they are small considering that the transmission coefficient for a photon incident at a normal angle on the acrylic surface with 350 nm of wavelength is about 96%.

OD PMTs

The OD wall hosts Hamamatsu R1408 20 cm PMTs. Light collection efficiency in the OD is enhanced by wavelength shifter (WS) plates attached to each OD PMT [18]. WS plates are square acrylic panels, 60 cm on a side and 1.3 cm thick, doped with 50 mg L^{-1} of bis-MSB (bis-Methylstyryl Benzole). The PMT is mounted into a machined hole at the center of the plate (Figure 2.10), optically coupled by direct contact or partially through water. The WS plates absorb UV light and radiate it back in the blue-green part of the spectrum, matching the sensitivity region of PMTs and improving light collection by a factor of 1.5.

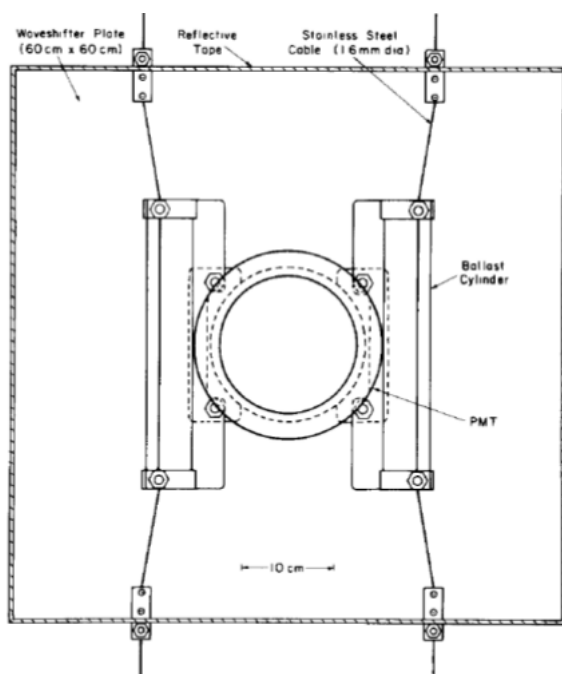


Figure 2.10: Schema of an OD PMT with its wavelength shifter plate. Taken from [18].

The plates do not degrade the timing resolution of the OD significantly, considering that the decay constant of fluor (4 ns) is small relative to the timing resolution of OD PMTs (13 ns): at single photoelectron illumination the timing resolution of OD PMT with plate is 15 ns (FWHM) [18]. This resolution is poor compared with the 2 ns resolution of ID PMTs, however the OD was designed to be used as a calorimeter and veto counter, rather than a particle tracker, so the extra photons are of importance while the increase in timing resolution is of little consequence. The OD volume is lined with

a reflective layer made from Type 1073B Tyvek[®] manufactured by DuPont. This inexpensive and tough paper-like material improves light collection in the wavelength range where OD PMTs are most sensitive since it has a measured light reflectivity of about 90% at 400 nm falling to 80% at about 340 nm [57]. It also minimizes the effect of dead OD PMTs by allowing multiple Cherenkov light reflections: Cherenkov light is spread over many PMTs reducing pattern resolution but increasing overall detection efficiency. Black and white liners that define the inner surface of the OD were specially made from a sandwich of Tyvek[®] facing the OD volume, a central layer of white Low-Density Polyethylene (LDPE) 25 mm thick and a 25 mm layer of black LDPE. This liner material provides a reflective surface on the OD side and a black absorptive surface facing the dead space between the OD and ID PMTs.

The dead space in between the ID and the OD

The thickness of the supermodules defines a dead space filled with water surrounded with light-proof lining and where the PMTs are connected to data and power supply cables. The OD PMTs are enclosed in water-proof housings which effectively block light from the dead space. The ID PMTs, instead, can detect some light propagating in this space since their backs are not fully covered.

Failing PMTs

PMTs can fail and this is taken into account during the operation of SK, since maintenance and replacement of any PMT is a task that can be performed only when the tank is empty. A very common reason for PMT failure is the flooding of the water-tight housing of their electrical connections. A PMT can also fail as a *flasher*: internal electrical discharges happen inside it and produce optical radiation and electrical noise which propagate inside the tank, requiring the PMT to be shut down. The rest of failing PMTs show a wide variety of electrical and other problems. Failed PMTs, once identified, are just left in place waiting for the next maintenance period to be replaced and their status is registered along with event data.

2.3.3 Water and air purification

Water in the tank must be very transparent to reduce attenuation of Cherenkov light along its path to the PMTs. The tank is filled with spring water from the mine after proper processing. Tank water is continuously purified and

circulated at a rate of about 30 tons/hour by a complex system consisting of several filters, a UV sterilizer and two degasifiers which remove particles larger than $0.2 \mu\text{m}$, bacteria, radon and oxygen dissolved in water respectively. Radon is an unwanted source of natural radioactivity, since it's a serious background event source for neutrinos analysis in the MeV energy range while oxygen is a bacterial growth promoter. The water temperature is controlled at around $13.5 \text{ }^\circ\text{C}$ by heat exchangers to reduce PMT dark noise and suppress bacterial growth. Typical radon concentrations in water coming into the purification system from the Super-Kamiokande tank are $< 2 \text{ mBq m}^{-3}$ and in water output by the system, $0.4 \pm 0.2 \text{ mBq m}^{-3}$. [22] The rocks in the mine leak radon that can end dissolved into tank water. In order to reduce radon induced background, the rock of the experimental hall is coated with a polyurethane cover and fresh air with a low radon concentration is continuously pumped from outside the mine into the experimental area through a processing facility at a rate of approximately $10 \text{ m}^3 \text{ min}^{-1}$: this flow keeps the experimental area slightly pressurized, minimizing the entry of ambient mine air. This constant radon-reduced air supply is needed by the degasifier section of the water purification plant to work properly as well. The fresh air intake opens 25 m above the Atotsu tunnel entrance where radon level concentration was found to remain at $10\text{-}30 \text{ Bq m}^3$ all year long. Air is pumped through a dehumidifier, a carbon filter tank, and finally through a 1.8 km air duct to the experimental area. All this equipment is housed inside the Radon Hut, a small building below the fresh air intake. Radon concentration inside the experimental area is kept at $30\text{-}50 \text{ Bq m}^{-3}$.

2.3.4 Electronics and data acquisition

Each PMT output in SK is connected to an electronic acquisition front-end channel via a 70 m long RG58 coaxial cable, one channel per PMT. If the negative signal pulse height fed into this input exceeds the trigger threshold level, the related PMT is tagged as *hit*. The trigger threshold for a PMT hit is -1 mV , corresponding to 0.25 photoelectrons. If the number of hit PMTs exceeds an event threshold, an event trigger is issued. The registered event consist of times and collected charges of hit PMTs within a given time window around the trigger timing. There are several event triggers depending on visible energy: Super Low Energy (SLE) trigger, Low Energy (LE), High Energy (HE), Outer Detector (OD) and so on. Since the data acquisition (DAQ) system which was used in SK-I to SK-III was upgraded for SK-IV, they must be discussed separately.

DAQ in SK-I to SK-III

The front end electronics of the ID PMTs for SK-I to SK-III is the analog timing module (ATM) (Figure 2.11) [9].

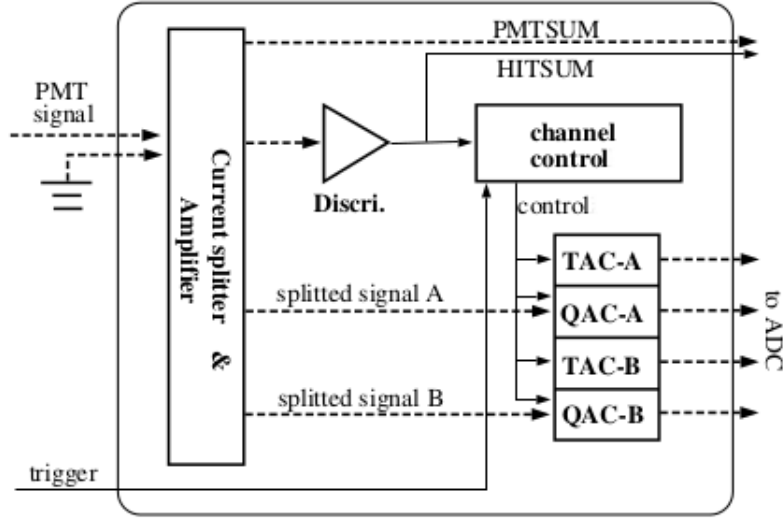


Figure 2.11: Schema of the analog input block of a single ATM channel. Dashed arrows show the PMT signal, its split signals and accumulated TAC/QAC signals. Solid arrows show the logic signals which control the processing of the analog signals.

One ATM has 12 channels: each channel records the integrated signal charge and the signal arrival time with a charge-to-analog converter(QAC) and time-to-analog converter (TAC) respectively. A total number of 960 ATMs were used. For each hit PMT, a 200 ns rectangular pulse with a 15 mV pulse height is generated by a discriminator stage. The ATM outputs the analog sum of all the rectangular pulses (HITSUM) from the PMTs connected to it. Then an event trigger is issued if the sum of HITSUMs from all ATMs exceeds a trigger threshold (Table 2.3). Once the event trigger has been issued, each ATM starts to digitize and record the time when the hit PMTs signal surpasses the threshold and the charge integrated in a 400 ns time window around the PMT trigger timing.

Two switching pair of both the QAC and TAC are included in each channel and managed by a *channel control* chip to avoid missing successive events as Michel electron, considering that the process time for one channel is 5.5 μ s. The time window for events is 1.3 μ s wide centered around the event trigger in a [-400 ns, +900 ns] fashion, where 0 ns corresponds to the event

Table 2.3: Hardware triggers used in SK-I to SK-III.

	SK-I	SK-II	SK-III
SLE	186 mV	110 mV	186 mV
LE	320 mV	152 mV	302 mV
HE	340 mV	180 mV	320 mV

trigger timing. The signal arrived from 400 ns to 900 ns after the hit is neglected in order to ignore a reflection pulse caused by an impedance mismatch between ATMs and PMTs. The ADC/TDC output data have 12 bit of resolution (4096 channels). The ATM has about 450 pC dynamic range for charge, with a resolution of 0.2 pC and about 1300 ns dynamic range in timing with a resolution of 0.4 ns. Conversion tables, instead of fitted linear functions, are used to maintain accuracy of the timing and charge information to convert ADC and TDC counts to pC and ns respectively. The temperature dependence of ADC and TDC pedestals (offsets) is linear and less than 3 count/ $^{\circ}\text{C}$ (0.6 pC/ $^{\circ}\text{C}$) and 2 count/ $^{\circ}\text{C}$ (0.8 ns/ $^{\circ}\text{C}$), respectively, in the typical ambient temperature range. Pedestal data are taken every 30 minutes during detector operation and the measured values are used to convert ADC and TDC counts within each half-hour period to take into account the effect of temperature dependence. Ambient temperature is kept at about ($27^{\circ}\text{C}\pm 0.5^{\circ}\text{C}$) in the electronics huts. The inaccuracies caused by temperature dependence are estimated to be less than 0.3 pC and 0.4 ns for the charge and timing information respectively. Signals from the OD PMTs are processed similarly by charge-to-time converter modules. When an event trigger is issued, the time and charge information are converted to digital by multi-hit time-to-digital converter modules (LeCroy 1877).

DAQ in SK-IV

SK-IV uses a new QTC-Based Electronics with Ethernet (QBEE) [10] front-end electronics, developed to improve dead time and fix the signal reflection issue, for both ID and OD PMTs. One QBEE module has 24 channels, each channel consists of a custom charge-to-time converter (QTC) and a multi-hit time-to-digital converted (TDC). The timing and charge resolutions of the QTC are 0.3 ns for 2 pC and about 0.2 pC for below 50 pC, respectively. The charge dynamic range of the QTC is 0.2-2500 pC and the charge non-linearity is better than 1% for the overall range. The QTC records all the hits and immediately integrates the charge from the signals in a 400 ns time window for each hit and TDC converts the QTC output into the digitized time and

charge. The digitized time and charge are recorded only after a software trigger has been issued. The software trigger is issued when the number of hit PMTs in a 200 ns sliding time window (N_{200}) exceeds a threshold (Table 2.4). In this system the SLE, LE and HE triggers are redefined. In addition to these triggers, the new Special High Energy (SHE) and After Trigger (AFT) are introduced: the AFT trigger is issued only for an event triggered by a SHE trigger without an OD trigger and saves an additional 500 μs of data.

Table 2.4: Software triggers used in SK-IV. The thresholds for the SLE and SHE triggers were lowered in May 2015 and September 2011 respectively.

Trigger type	N_{200} threshold	Time window (μs)
SLE	34 \rightarrow 31	-0.5 \sim +1.0
LE	47	-5 \sim +35
HE	50	-5 \sim +35
SHE	70 \rightarrow 31	-5 \sim +35
LE	47	-5 \sim +35
AFT	SHE without OD	+35 \sim +535
OD	22 in OD only	-5 \sim +35

2.4 ID calibration

Each PMT in the ID outputs two direct measurements: hit integrate charge and timing. PMT responses must be calibrated in order to collect reliable data: the charge and time response of each PMT must be the same for the same intensity and timing of the incident light. A proper calibration is required for simulation as well: transport of photons inside the tank must be characterized, assumptions about detector response like symmetry under rotations around its axis must be validated and so on. A detailed account of the official SK calibration procedures can be found in [12].

2.4.1 SK Coordinate axis system

The origin of the SK coordinate system is the exact center of the SK tank. The z axis is parallel to the cylindrical tank axis and points upwards towards the mountain surface. The x axis is perpendicular to the z axis and points towards the SK access tunnel that connects the dome experimental area to

the Atotsu mine tunnel. The y axis direction is calculated by cross product of the two other axis.

2.4.2 Calibration of ID PMTs

The gain of a PMT is defined as a conversion factor from the number of photoelectrons to charge (in units of pC). QE is defined as the product of the quantum efficiency and collection efficiency of photoelectrons onto the first dynode of the PMT [12].

Determination of high voltage (HV) setting for each ID PMT

The first step of calibration consists in setting the high voltage (HV) for each PMT in such a way that the output charge of each PMT is the same for the same light intensity. The light emission from a scintillator ball installed at the tank center is used: it is fed via an optical fiber with the light of a Xenon lamp passing through a UV filter. The calibration source is isotropic by construction: since the SK ID is cylindrical, there is a dependency between the PMT location and the intensity of calibration light arriving at it. A simple geometrical correction is not sufficient since there are important effects from photon propagation in water and ID reflections, then 420 *standard PMTs* were pre-calibrated in a laboratory inside the mine and then mounted in the ID at specific locations during the maintenance period between SK-II and SK-III (Figure 2.12).

The reproducibility of the observed charge for all standard PMTs with respect to their reference values was checked and evaluated as 1.3% RMS. The standard PMTs provide a reference for other PMTs which share the same geometrical relationship with the calibration light source.

Relative differences of gain

The gain of each ID PMT must be determined in order to interpret the output charge in number of photoelectrons. This is done in two steps. The first step is to determine the relative difference among PMTs, using an isotropic diffuser ball permanently placed in the middle of the tank as calibration light source. The ball is fed by a Nitrogen laser (USHO KEC-100, pulse width of 0.4 ns FWHM at a wavelength of 337 nm) shifted by a dye to 398 nm with 0.2 ns pulse width, whose output is monitored by a 2-inch PMT (Hamamatsu H2431-50, rise time 0.7 ns). The output wavelength is chosen to correspond to the maximum of the convoluted response with Cherenkov spectrum, light

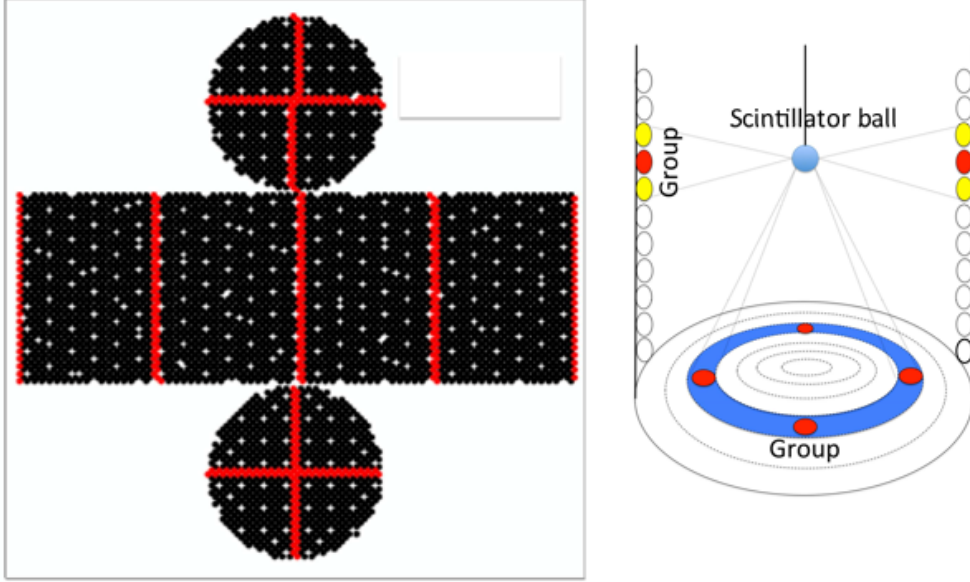


Figure 2.12: The location of standard PMTs inside the SK inner detector (left). The red points indicate the locations of the standard PMTs. These PMTs served as references for other PMTs belonging to the same group with similar geometrical relationship to the light source (right). Taken from [12].

absorption spectrum and quantum efficiency of the PMTs. The output light intensity can be adjusted using a set of neutral filters (Figure 2.13).

The first measurement uses high-intensity (I_H) light flashes, such that every PMT is reached by a several photons, and records the average observed charge $Q_{obs}(i)$ for each PMT i :

$$Q_{obs}(i) \propto I_H(i) \times a(i) \times \epsilon(i) \times G(i) \quad (2.6)$$

where $a(i)$ is the PMT light acceptance, $\epsilon(i)$ is the PMT quantum efficiency and $G(i)$ is the PMT gain. The second measurement uses low-intensity (I_L) flashes, such that only a few PMTs are hit per flash: it's reasonable to assume that these are single-photoelectron hits. The number of times $N_{obs}(i)$ that PMT i records a hit can be expressed as:

$$N_{obs}(i) \propto I_L(i) \times a(i) \times \epsilon(i) \quad (2.7)$$

Since the location of the light is unchanged the complicating factors in both expressions cancel out. The gain of each PMT can be derived from:

$$G(i) \propto \frac{Q_{obs}(i)}{N_{obs}(i)} \quad (2.8)$$

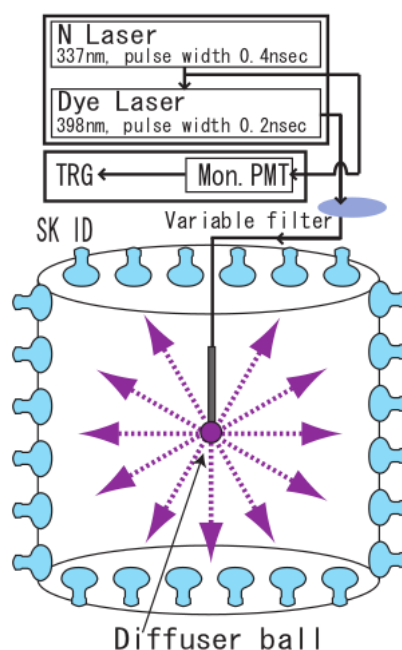


Figure 2.13: The apparatus used for PMT relative gain and timing calibration. A set of neutral filters is used to adjust the output intensity. Taken from [12].

Then the relative gain of each ID PMT can be calculated by normalization with the average gain over all PMTs.

Absolute gain conversion factor

The second step is to determine the average gain over the whole detector. Then the absolute gain of each ID PMT can be extracted. The calibration source is a Nickel sphere which emits 9 MeV gamma rays isotropically upon capturing the neutrons produced by a ^{252}Cf source placed in its centre. The sphere is placed at the centre of the ID and produces 0.004 photoelectrons/event at each PMT on average, 99% of hits are from single photoelectrons. After correcting for the relative gain variation for each PMT, the observed charge distribution for the single photoelectron hits is obtained by accumulating the hits from all PMTs (Figure 2.14).

From the average of this distribution, the conversion factor between the observed charge and the number of photoelectrons is determined to be 2.658 pC/photoelectron for SK-IV.

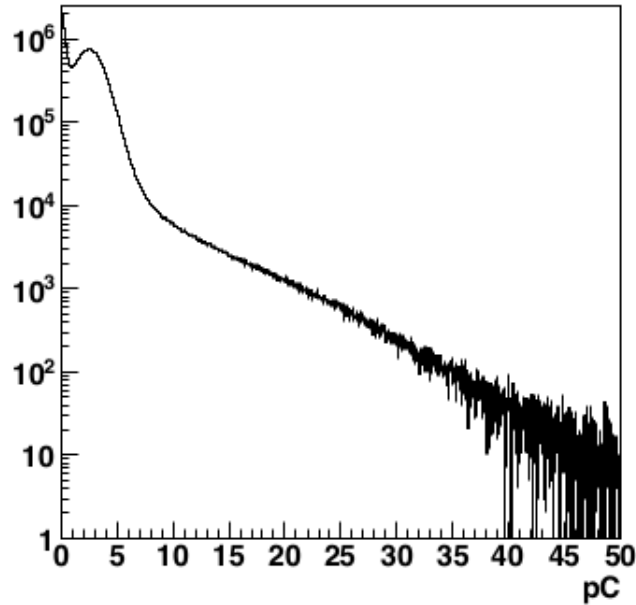


Figure 2.14: Number of hits versus charge produced with the Nickel source. Taken from [12].

PMT gain variation over time

The gain of ID PMTs changes over time. The PMT gain time variation is measured by using the cosmic-ray muons going through the detector, so-called *through-going* muons. Since muons deposit in water 2 MeV/cm regardless of their energy, the muon track can be considered as a standard light source. For SK-IV, the PMT gain time variation is evaluated by taking the early off timing hit distribution for each PMT in the *through-going* muon sample, in order to estimate the PMT absolute gain by looking at the single photoelectron peak: the PMT gain time variation depends from the PMT production year (Figure 2.15). This effect is corrected at reduction time.

Relative QE calibration

QE differs from one PMT to another one. The same NiCf source used for the absolute gain calibration is used for the relative QE calibration, producing hits whose probability is proportional to QE due to the low intensity of its light flashes. During this calibration, tank water is convected to ensure its uniformity over the ID volume. The number of photons reaching each PMT is estimated by Monte Carlo (MC) simulation. If the simulation models tank

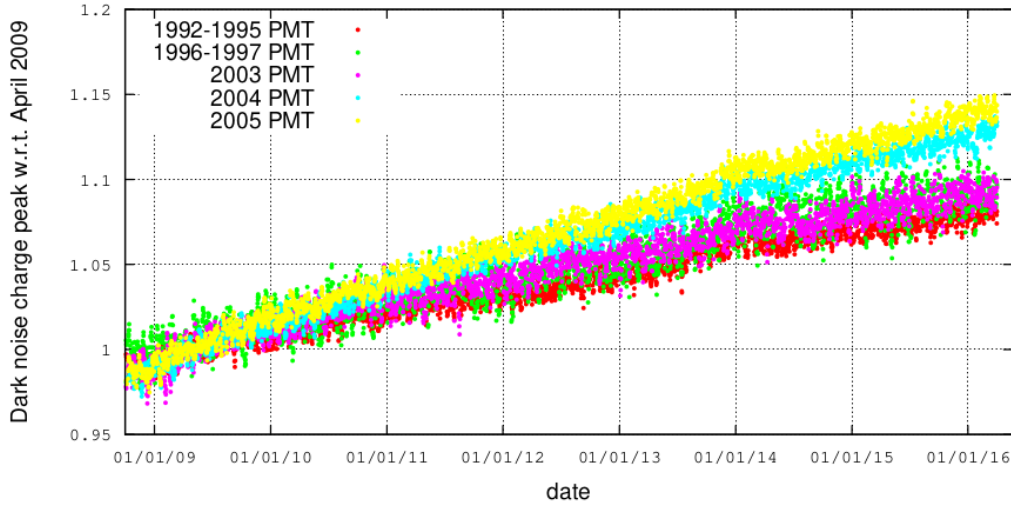


Figure 2.15: PMT production year dependence of the PMT gain time variation in SK-IV.

water properties, such as photon absorption and scattering and reflections inside the ID, the remaining difference between simulation and calibration data is due to the QE of individual PMTs. The ratio between the number of observed hits in data to MC is the PMT QE: it's stored in tables and used for simulation.

Timing calibration

The time response of each read-out channel must be calibrated for the differences in transit time of PMTs, length of coaxial cables and dependency of electronic processing time from collected charge (*time-walk* effect). Timing calibration is performed using the same source as the one used for relative gain calibration (Section 2.4.2). Time-of-flight (TOF) is defined for each ID PMT as the difference between ID PMT and monitor PMT hit times recorded after the emission of one flash: it takes into account the differences in light path between different ID PMTs by fixing the monitor PMT timing as a reference. Response times are corrected for relative timing differences by subtracting TOF from them. The same measurement is performed at different laser intensities to take into account timing dependency from collected charge. The result is plotted for each PMT as a 2D distribution known as *TQ plot* (Figure 2.16).

Each TQ distribution is fitted by an asymmetric gaussian in each charge bin, and the peak position of the gaussians is then fitted by a polynomial

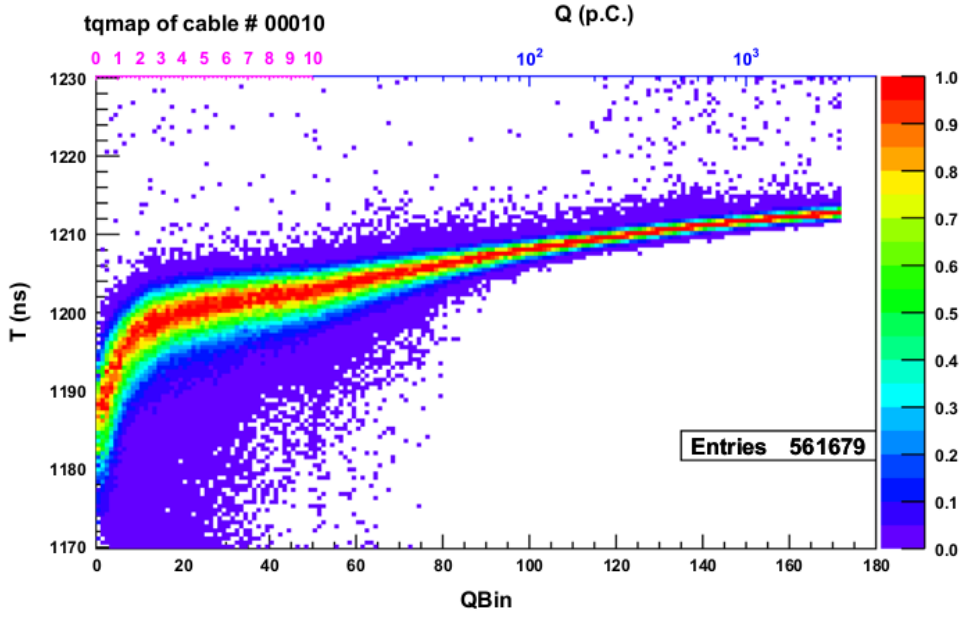


Figure 2.16: Example of the TQ plot for an ID PMT. The vertical and horizontal axes represent to the TOF subtracted hit timing and the hit charge, respectively. Taken from [12].

as a function of charge, named *TQ map*, which is used to correct PMT hit timings for charge dependency.

2.4.3 Water properties measurement

The light attenuation in tank water is modeled by the law:

$$I(\lambda) = \exp(-l/L(\lambda)) \quad (2.9)$$

where $I(\lambda)$ is the intensity of light at wavelength λ and l is the distance traveled in water. $L(\lambda)$ is the attenuation length in water at wavelength λ and it's defined as:

$$L(\lambda) = \frac{1}{\alpha_{sym}(\lambda) + \alpha_{asy}(\lambda) + \alpha_{abs}(\lambda)} \quad (2.10)$$

is the *symmetric scattering* amplitude which takes into account the effects of Rayleigh and symmetric Mie scattering, whose angular distribution depends from the photon scattering angle θ as $1 + \cos^2(\theta)$. α_{asy} is the *asymmetric scattering* amplitude which accounts for forward Mie scattering with angular distribution $\cos \theta$, forward only. Finally, α_{abs} is the *absorption coefficient*.

These coefficients are empirical functions of the wavelength λ which are measured using the laser injector system (Figure 2.17).

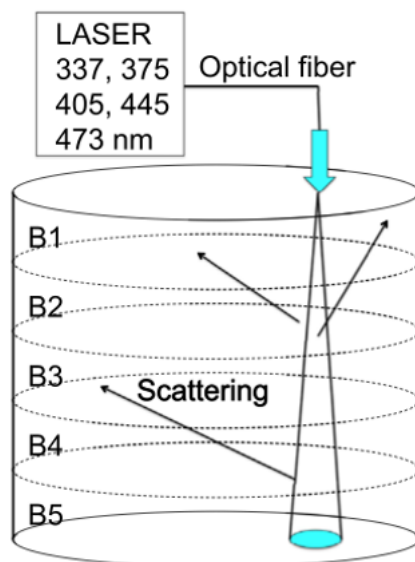


Figure 2.17: A schematic view of the laser injector system for measuring the water property and the reflectivity of the PMTs.

A collimated laser beam is injected into the tank vertically from its top: the light scattered in water and reflected from the bottom is detected by the PMTs on the side and top wall of the ID. The TOF-subtracted hit time distribution, calculated as the PMT hit timing distribution after subtracting the time required by photons to travel from the beam spot at the bottom to each PMT, for the PMTs in each detector region, as indicated in Figure 2.17, is shown in Figure 2.19. The sharp peaks on the right between 1830-1900 ns are due to the photons reflected at the beam spot from the bottom of the detector, whereas the hits at earlier times are caused by photons which scattered in water before reaching the bottom. Data before 1830 ns is used to tune the scattering and absorption coefficients at different wavelengths. Figure 2.18 shows the scattering and the absorption coefficients as functions of wavelength which are tuned using data taken in April 2009, and the red histograms in Figure 2.19 are the timing distributions for the best-tuned laser injection simulation.

The measurement leads to an overall attenuation length of ~ 120 m at 400 nm wavelength. The apparatus is permanently deployed in the detector and constantly takes data during SK operation so that water parameters are continuously monitored.

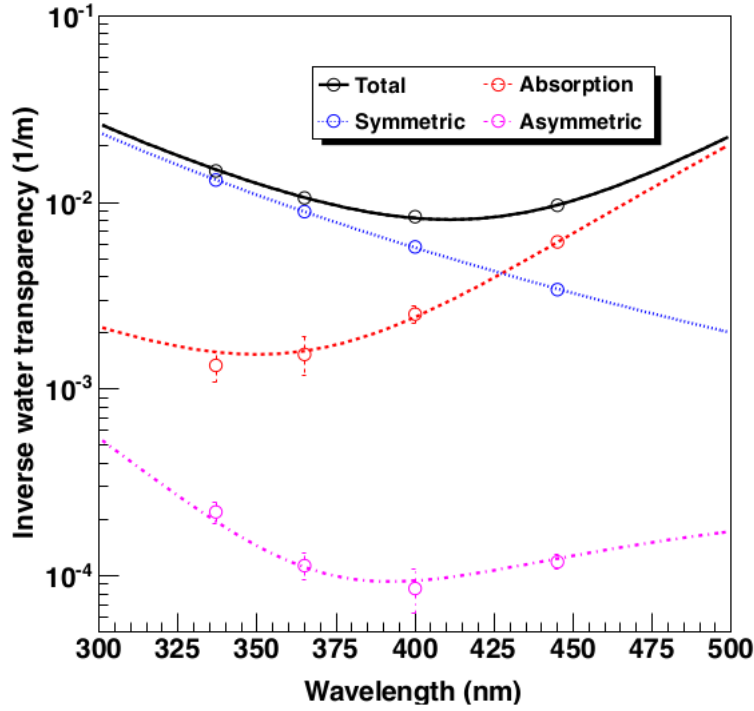


Figure 2.18: Light absorption and scattering coefficients as a function of wavelength. The data points are the data taken in April 2009 and the red, blue and magenta lines represent the tuned $\alpha_{abs}(\lambda)$, $\alpha_{sym}(\lambda)$ and $\alpha_{asy}(\lambda)$ respectively. The black line represents the sum of the three contributions, which is the inverse of the attenuation length $L(\lambda)$.

2.4.4 PMT and black sheet reflectivity measurement

Detector simulation models take into account PMTs reflectivity by ignoring reflections happening in their internal structure and considering interactions with four layers and their interfaces: tank water, PMT glass, photocathode and vacuum inside the tube.

Each layer is characterized by a wavelength-dependent refractive index and, since the photocathode layer absorbs light, a complex refractive index is assigned to the photocathode.

Using the laser injector data in the time range 1830-1900 ns, which contains the peaks from the light reflected at the tank bottom as shown in Figure 2.19, the complex refractive index of the photocathode is tuned such that the laser injector simulation best agrees with the measured data in this region. The tuning is performed at the wavelengths 337, 365, 400 and 420 nm.

The reflectivity of the black sheet is measured in the SK detector using

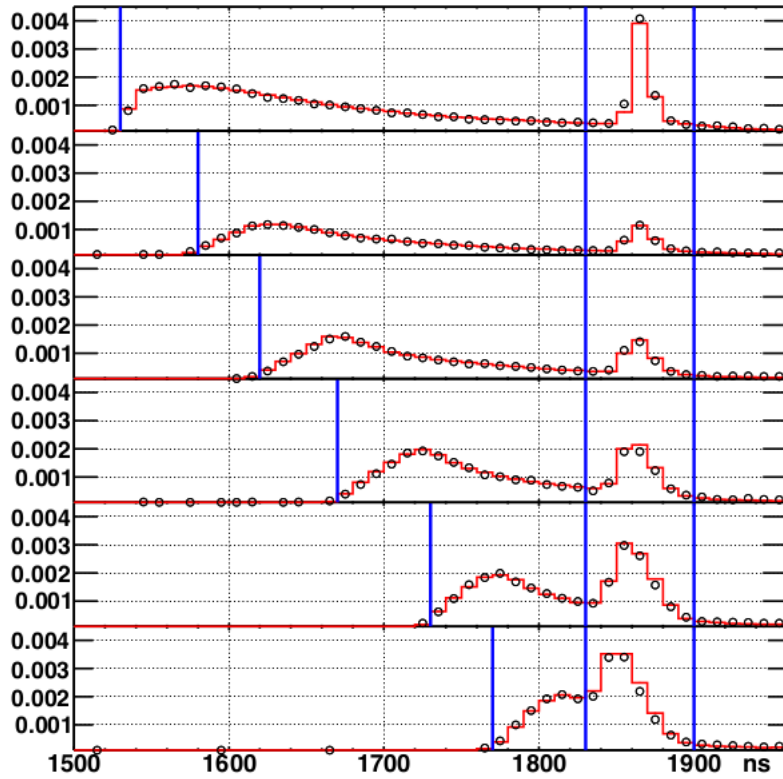


Figure 2.19: The TOF-subtracted hit time distributions for the laser injector data taken at 405 nm. The top plot is for the PMTs on the top wall and the following five plots correspond to the the five regions on the barrel as indicated in Figure 2.17. The black circles represent the measured data and the red histograms are the result from the laser injector simulation after tuning the water properties and PMT reflectivity to data. The data before 1830 ns and between the two vertical blue lines on the left is used for the water measurement and the data in the range 1830-1900 ns is used for tuning the PMT reflectivity.

the apparatus shown in Figure 2.20: a laser injector unit to which a specimen of the black sheet is attached is placed in the centre of the water tank and the laser reflected from the black sheet is projected horizontally to the side of the ID. The intensity and the profile of the reflected light is then measured by the ID for each of the the incident angles 30° , 45° and 60° and for the wavelengths 377, 400 and 420 nm. The intensity of the injected light directly projected onto the wall without reflection is also measured for normalizing the reflected light data and the reflectivity calculated from the measured result is used in the detector simulation.

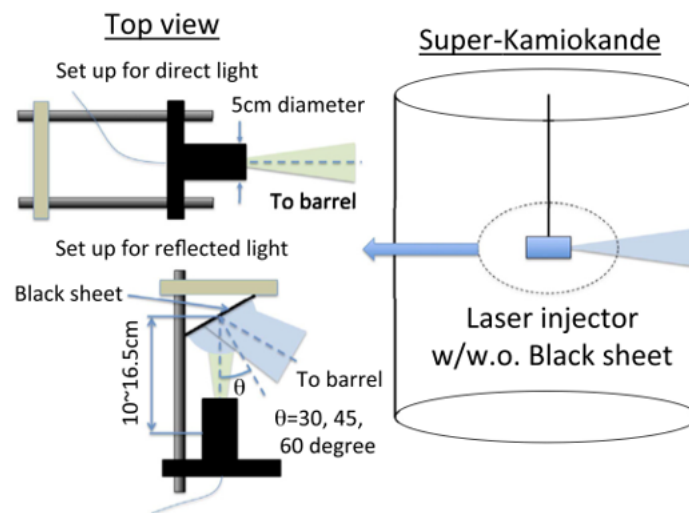


Figure 2.20: A schematic view of the apparatus for black sheet reflectivity measurement.

Chapter 3

SK Data

In a single day of operation, the SK detector is triggered about 10^6 times: only a small part of these events are interesting enough to be saved and stored for analysis. The process of selecting these events is known as *reduction*.

Events are classified in three categories:

- Fully Contained (FC): all the event energy is deposited in the ID;
- Partially Contained (PC): the event originates in the ID but a significant part of its energy is deposited in the OD;
- Up-going Muons (UPMU): high-energy muons produced by neutrino interactions happening inside the Earth, entering the detector from below the horizon.

This analysis is performed using real FC data spanning the full livetime of SK-IV, i.e. 3244.4 days equivalent to 200 kton*year of exposure.

A detailed reference for all the reduction processes can be found in [52] while further details for the FC process can be found in [35].

3.1 Official FC reduction process

An event is classified as FC if it passes five reduction steps, named from FC1 to FC5. These reduction steps aim at selecting high-energy events.

3.1.1 First reduction (FC1)

The purpose of this stage is to reject low-energy events from radioactive background and cosmic-ray muons. Events pass this stage if:

- $PE_{300} > 200$ where PE_{300} is the total number of photoelectrons counted in all the hit PMTs in a sliding 300 ns wide time window;
- $NHITA_{800} \leq 55$ where $NHITA_{800}$ is the total number of OD tubes hit within a (-500 ns, +300 ns) time window around the trigger time (0 ns).

The first condition checks if there is significant activity in the ID, equivalent to the activity produced by an electron with a 22 MeV/c momentum at least, removing most of the background events coming from low-energy radioactivity, from low-energy *Michel electrons*¹ and from solar neutrinos. The second condition removes most cosmic-ray muons and rules out PC and UPMU events. About 3000 events per day remain after this step.

3.1.2 Second reduction (FC2)

Events must meet these two conditions to pass:

- $NHITA_{800} < 25$ for events with $PE_{total} < 100000$ where PE_{total} is the total number of photoelectrons counted in the ID PMTs;
- $PE_{max}/PE_{300} < 0.5$ where PE_{max} is the maximum number of photoelectrons counted in a single ID PMT.

The first condition further reduces the number of low-energy cosmic ray muons by eliminating low-energy events with significant OD activity.

The second criterion reduces the number of electrical noise events caused by an electrical discharge in a PMT: it rejects an event if more than half of the total ID charge originates from a single PMT.

The average number of events passing this step is ~ 200 per day.

3.1.3 Third reduction (FC3)

This reduction step targets specific event categories: it aims, in particular, at reducing the remaining cosmic-ray muons, especially those with low OD activity and the remaining low-energy radioactivity background events.

Through-going muons

Through-going muons pass through the tank: they may produce low activity in the OD while leaving a significant energy deposit in the ID. Through-going muon event candidates are pre-selected by these two conditions:

¹A *Michel electron* is the electron produced in a muon decay.

- over 1000 hit PMTs in the ID;
- $PE_{\max} > 230$.

Passing candidates are processed by a dedicated fit algorithm. First, a clustering algorithm searches for the two largest clusters of contiguous hit OD PMTs and assumes that they correspond to the entrance and exit regions of the muon candidate. The position of the earliest hit OD PMT is taken as the entry point while the exit point is calculated as the centroid of the exit cluster. A Monte Carlo simulation is used to estimate a set of expected hit timings T_i and a goodness-of-fit value is calculated as:

$$g_{\text{fit}} = \frac{1}{\sum_i \frac{1}{\sigma_i^2}} \times \sum_i \frac{1}{\sigma_i^2} \exp\left[-\frac{(t_i - T_i)^2}{3\sigma_i^2}\right] \quad (3.1)$$

where t_i and σ_i are the hit timing and timing resolution of the i^{th} PMT.

The event is tagged as through-going muon and rejected if the following two criteria are met:

- $g_{\text{fit}} > 0.75$;
- $NHITA_{\text{in}} > 10$ and $NHITA_{\text{out}} > 10$ where $NHITA_{\text{in}}$ and $NHITA_{\text{out}}$ are the number of hit OD PMTs within 8 meters of the fitted entry and exit point respectively.

Hard muons

Critical energy of muons is about 1 TeV in water: above this threshold the almost constant ionization loss of 2 MeV/c becomes secondary with respect to other processes like bremsstrahlung and pair production, which produce a large number of hits in a short time. High-energy (> 1 TeV) cosmic-ray muons, known as *hard muons*, are identified by the following condition:

- $NHITA_{500} > 40$

where $NHITA_{500}$ is the number of hits in the OD in a sliding 500 ns wide time window and rejected.

Stopping muons

Stopping muons enter the tank from the outside and stop there. Stopping muons produce events similar to the ones produced by through-going muons, except for the absence of an exit cluster in the OD. The muon direction is reconstructed by maximizing the charge seen by the ID PMTs within a cone

with a 42° opening angle² having its vertex at the entry point. A goodness-of-fit g_{fit} value is calculated in a similar way to Equation 3.1. The following condition is used to identify stopping muons:

- $g_{\text{fit}} \geq 0$ and $\text{NHITA}_{\text{in}} \geq 10$.

If this condition is fulfilled the event is rejected.

Cable hole muons

The cables connecting OD and ID PMTs inside the tank to front-end electronics in the outside huts pass through twelve holes in the top section of the OD. These holes interrupt the OD coverage: down-going muons may pass through them and reach the ID without being detected in the OD, producing an event which would be erroneously categorized as FC. In order to mitigate this effect, four of the twelve holes have plastic scintillator veto counters installed beneath their openings (Figure 3.1).

An event is identified as cable muon event and rejected if:

- a cable veto counter is hit;
- the entry point or exit point is within 4 metres of the hit veto counter;
- $\text{PE}_{\text{total}} > 4000$;
- the entry point is within 2.5 meters of the nearest cable hole

and if the stopping muon fitter applied to the event returns results matching with these conditions:

- goodness-of-fit for stopping muon ≥ 0.4 ;
- the reconstructed zenith angle θ of the muon is more vertical than horizontal: $\cos \theta < -0.6$.

Flasher PMTs

A *flasher* is an event due to a repetitive electric discharge in the dynode stage of a PMT that may be detected by nearby PMTs as well. Such an event can be recognized from its abnormally broad hit timing distribution (Figure 3.2). In order to reduce flasher events, those ones presenting too much ID activity well after the trigger time are rejected. This procedure translates into the following condition:

²This choice corresponds to the Cherenkov angle for a $\beta \sim 1$ particle in water ($n = 1.34$) as shown in Section 2.2.1.

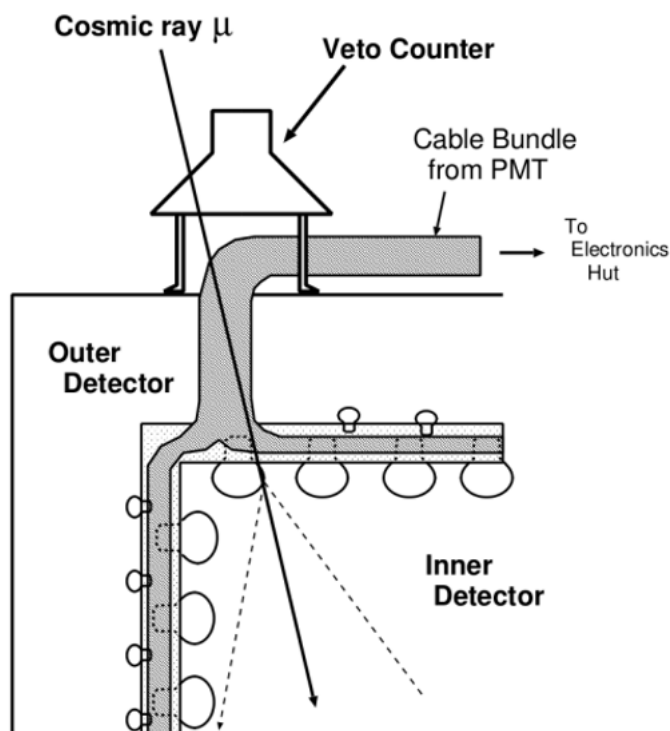


Figure 3.1: A schematic view of one of the cable holes and its veto counter. Taken from [35].

- $N_{MIN_{100}} \geq 20$.

Where $N_{MIN_{100}}$ is the number of ID PMTs hit in a 100 ns wide time window sliding in a range between 1200 ns and 1700 ns after the trigger time.

If an event meets this condition is rejected.

Coincidence muons

If a cosmic-ray muon enters the detector immediately after a low-energy event has issued a trigger, its activity is recorded together as well. The energy deposited by the muon may let the low-energy event pass the low-energy cuts, conversely it may pass the high-energy cuts due to the delayed muon OD activity with respect to the trigger time.

Events matching this condition are identified as coincidence muons and rejected:

- $N_{HITA} \geq 20$

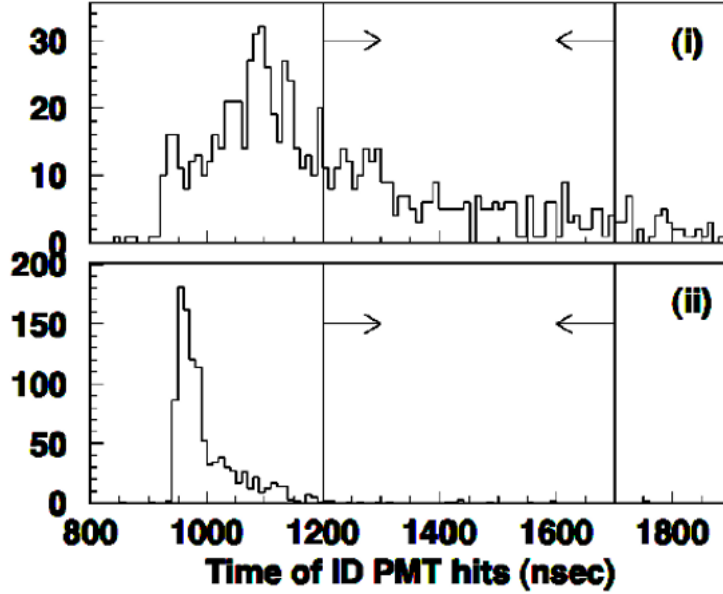


Figure 3.2: Typical distributions of $NMIN_{100}$ for a flasher (top) and an atmospheric neutrino MC event (bottom). The arrows indicate the region that is removed with the third reduction flasher cut. Taken from [35].

where $NHITA_{\text{off}}$ is the number of OD hits between 300 ns and 800 ns after the trigger time.

Low energy events

Finally, a cut to reduce remaining low-energy events is applied. An event is rejected if:

- $NHIT_{50} < 50$ (25 for SK-II)

where $NHIT_{50}$ is the number of hit ID PMTs within a sliding 50 ns wide time window. Hit times are corrected using a time-of-flight (TOF) fitter that assumes that all the photons detected come from a single vertex. This energy threshold corresponds to visible energy of 9 MeV. After this reduction ~ 45 per day remain.

3.1.4 Fourth reduction (FC4)

This step targets the remaining flasher events by detecting their typical highly-correlated charge pattern that spans several event timing windows. A typical flasher event is shown in Figure 3.3.

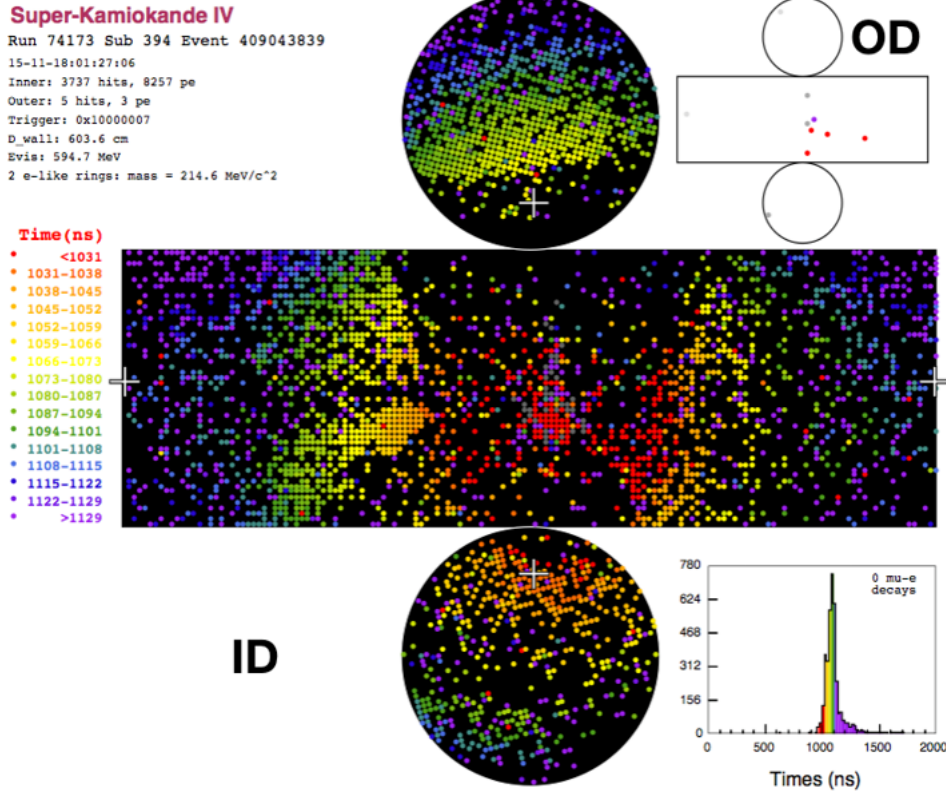


Figure 3.3: Typical flasher event display. A PMT in the middle of the ID barrel has flashed light in consequence of an electric discharge in its dynode stage. The PMT color indicates the hit timing (red: early hit, blue: late hit). Taken from [56].

The following algorithm is defined to check if two events (A and B) show correlated charge patterns in the ID:

- the ID tank wall is divided into 1450 roughly equal 4 m² partitions;
- the correlation r between event A and event B is calculated as:

$$r = \frac{1}{N} \sum_i \frac{(Q_i^A - \langle Q^A \rangle) \times (Q_i^B - \langle Q^B \rangle)}{\sigma_A \times \sigma_B} \quad (3.2)$$

where N is the number of partitions, i refers to the i^{th} partition, Q_i is the charge observed in the i^{th} partition and $\langle Q \rangle$ is the average charge per partition observed in an event with RMS σ ;

- the distance d_{\max} between the PMTs with the maximum charge in each event is calculated. For $d_{\max} < 0.75$ m, the correlation r is incremented:

$$r = r + 0.15 \quad (3.3)$$

- two events are defined as a match if their correlation exceeds a threshold r_{th} :

$$r_{\text{th}} = 0.168 \times \log_{10} \left(\frac{\text{PE}_{\text{tot}}^{\text{A}} + \text{PE}_{\text{tot}}^{\text{B}}}{2} \right) + 0.130 \quad (3.4)$$

where PE_{tot} is the total number of photoelectrons detected in an event. This threshold has been calculated by comparing correlation distributions of atmospheric neutrino Monte Carlo simulated events and hand-picked real flasher events.

The correlation value r is calculated for 10000 events near the target event and matching events are rejected: ~ 18 events per day remain after this step.

3.1.5 Fifth Reduction (FC5)

The fifth reduction targets three specific categories of remaining background: invisible muons, coincidence muons and long-tail flashers.

Invisible muons

Muons below Cherenkov threshold can decay inside the tank: they are invisible but their *Michel electron* can be detected. If some OD activity is detected, these events can be rejected as cosmic-ray muons. Events that meet these two conditions are rejected:

- $\text{PE}_{\text{total}} < 1000$;
- if $\text{Dist}_{\text{clust}} < 500$ cm then $\text{NHITAC}_{\text{early}} + \text{NHITAC}_{500} \geq 10$
else $\text{NHITAC}_{\text{early}} \geq 5$

where PE_{total} is the total number of photoelectrons detected in the ID, NHITAC is the number of hit PMTs in the OD largest cluster: $\text{NHITAC}_{\text{early}}$ is defined in a sliding 200 ns wide time window from -9000 ns to -200 ns prior to the primary trigger time, NHITAC_{500} counts the hits in the time interval corresponding to -200 ns to 300 ns with respect to the trigger time and $\text{Dist}_{\text{clust}}$ is the distance between the centroids of these clusters. These cuts correspond to the maximum photoelectron yield of a *Michel electron* with a significant early OD activity.

Coincidence muons

Remaining coincidence muons are targeted by the following cut: it searches for off-trigger OD activity in a longer time span than in the FC3 reduction step.

An event meeting the following criteria is rejected:

- $PE_{\text{total}} < 300$;
- $NHITA_{\text{late}} \geq 20$

where $NHITA_{\text{late}}$ is the number of hit PMTs in the OD in a sliding 200 ns wide time window from 300 ns to 2100 ns with respect to the trigger time.

Long-tail flashers

This cut targets the remaining flasher events using a TOF-fitter similar to the one described in Section 3.1.3, using its evaluated goodness-of-fit as a cut parameter. An event is rejected if the following criteria are met:

- $NMIN_{100} \geq 6$ with TOF goodness-of-fit < 0.4 ;

or

- $MIN_{100} < 6$ with TOF goodness-of-fit < 0.3

where $NMIN_{100}$ has the same definition as in Section 3.1.3.

Calibration related events cut

Some LASER or Xenon lamp calibration events may leak into the data set due to some errors in data management. They can be removed by checking if at least one of the dedicated reference PMTs is reported as hit. After this step ~ 16 events per day remain.

3.1.6 Human eye scan of FC events

In addition to the automated FC reduction, a real time check in the data quality is conducted by human operators by eye for the events after the third reduction. The scanners check the hit charge and timing distribution and the hit pattern for both the ID and OD using an event display tool, in order to judge if the reduction algorithm works properly or not and notify any unusual thing.

3.1.7 The final FC cut

The final FC sample is defined by these three last cuts, that can be applied only after a reconstruction algorithm has processed the event:

- $d_{\text{wall}} \geq 200$ cm
 d_{wall} is the distance of the reconstructed vertex from the nearest ID wall. This distance defines the Fiducial Volume (FV), containing 22.5 kton of water: keeping only the events inside this subregion of the ID ensures that the background from outside the tank is further reduced and that vertexes are well reconstructed;
- $\text{NHITAC} < 16$
 NHITAC is the number of hits in the OD. Such a low activity in the OD ensures that the event is, indeed, fully contained inside the ID;
- $E_{\text{vis}} \geq 30$ MeV
 E_{vis} is the *visible energy* i.e. the total energy of all reconstructed rings assuming that they are all produced by electrons.

These cuts are called the *FCFV cuts*: after these cuts ~ 8 events per day remain.

3.1.8 Generation of the atmospheric neutrino Monte Carlo FC sample

This analysis uses 500 years of Monte Carlo simulated atmospheric neutrino interactions in SK-IV to study the expected background. The sample used underwent the same reduction process as real data.

3.1.9 Atmospheric neutrino flux

Atmospheric neutrinos are produced in the interactions between primary cosmic rays, mainly protons and helium nuclei coming from outside the Solar System, or from solar flares, and atmospheric nuclei.

Cosmic rays with energies lower than 10 GeV in the laboratory frame are modulated by the solar wind, the expanded magnetized plasma generated by the Sun which decelerates and prevents part of the incoming charged particles from entering the inner Solar System: their flux shows a significant anticorrelation with solar activity, which follows an 11-year periodic cycle.

Cosmic rays in the GeV energy range are modulated by the geomagnetic field, which must be penetrated by them to reach the top layer of the atmosphere: this makes the composition of cosmic rays reaching the Earth surface dependent on both location and time.

Cosmic rays A_{cr} produce kaons and pions in their hadronic interactions with atmospheric nuclei A_{atm} .

$$A_{\text{cr}} + A_{\text{atm}} \rightarrow \pi^\pm, K^\pm, K^0, \dots \quad (3.5)$$

At low energies (≤ 1 GeV in the laboratory frame) K/π ratio is less than 7% [14], so the following decays are the dominating sources of neutrinos:

$$\begin{aligned} \pi^+ &\rightarrow \mu^+ \nu_\mu \\ \mu^+ &\rightarrow e^+ \nu_e \bar{\nu}_\mu \end{aligned} \quad (3.6)$$

$$\begin{aligned} \pi^- &\rightarrow \mu^- \bar{\nu}_\mu \\ \mu^- &\rightarrow e^- \bar{\nu}_e \nu_\mu \end{aligned} \quad (3.7)$$

By neglecting the contribution from kaon decays and assuming that all of the muons decay in flight before reaching the Earth surface, that is true for energies ≤ 5 GeV, and counting the number of neutrinos and antineutrinos produced for both flavors, this naive estimate can be made:

$$\frac{(\nu_\mu + \bar{\nu}_\mu)}{(\nu_e + \bar{\nu}_e)} = 2 \quad (3.8)$$

The observation of a lower-than-expected ratio for fluxes coming from below the horizon in Super-Kamiokande led to the experimental discovery of neutrino oscillations [61]: ν_μ may oscillate to ν_τ while passing through the Earth, causing a reduction in the ν_μ measured flux from those zenith angles. A detailed theoretical explanation of the oscillation phenomenon can be found in [2].

The neutrino flux at Super-Kamiokande location has been precisely modelled and calculated by M. Honda et al.: this model is known as the *Honda flux* [15] [16]. The Monte Carlo generator uses the Honda flux without considering neutrino oscillations: it provides an oscillation probability weight for each generated event allowing to apply it later during the analysis.

3.1.10 Neutrino interactions

Neutrino interactions inside the tank are simulated by the NEUT software [36]. The software simulates neutrino interactions with Oxygen and Hydrogen nuclei in water: the cross section with electrons is three orders of magnitude smaller than the cross section with nuclei, so neutrino interactions with electrons are neglected.

Neutrinos can interact weakly with nuclei via the exchange of a charged W boson or a neutral Z boson: the former interactions are known as **Charged Currents (CC)** since they involve an exchange of electric charge, conversely the latter ones are known as **Neutral Currents (NC)**.

The charged lepton produced in a neutrino CC interaction retains the neutrino flavor, making it identifiable by SK, while in NC interactions the flavor of the interacting neutrino is unknown. This is the reason why the CC interactions contribute to the signal for the analysis of neutrino oscillations while the NC interactions contribute to the background.

In proton decay search analysis both CC and NC interactions contribute to the background.

Finally, even if atmospheric neutrinos are generated only in the e and μ flavor, there is some ν_τ flux reaching SK due to neutrino oscillations that can interact producing τ leptons via CC interactions: the decay of τ leptons is complex and it's simulated by the software TAUOLA [23].

NEUT simulates the following neutrino interactions:

- elastic and quasi elastic scattering;
- resonant production;
- deep inelastic scattering.

Elastic and Quasi Elastic Scattering

In NC elastic scattering, a neutrino just scatters off a nucleon without producing any new particles. On the other hand, a neutrino converts into its corresponding charged lepton in CC Quasi-Elastic (CCQE) scattering:

$$\nu_x + N \rightarrow l_x + N' \quad (3.9)$$

where l is a lepton, charged in CCs or a neutrino in NCs, of the same flavor as the interacting neutrino, N is the initial state of the target nucleon and N' is its final state.

CCQEs may happen with nucleons other than the target affecting the final state [56]; this is known as Meson Exchange Current (MEC) interaction:

$$\nu_x + N + N' \rightarrow l_x + N'' + N''' \quad (3.10)$$

Resonant production

Production of a single meson in a neutrino interaction is modeled in NEUT primarily as a resonance production, in which a baryon resonance excitation

produces a single meson in the final state as in:

$$\begin{aligned}\nu_x + N &\rightarrow l_x + N^* \\ N^* &\rightarrow N' + m\end{aligned}\tag{3.11}$$

where N and N' are the nucleon in the initial and the final state, N^* is the intermediate baryon resonance and m is a meson, such as π , K and η , or a photon. Such interaction is considered in NEUT for $W < 2 \text{ GeV}/c^2$, where W is the invariant mass of the hadronic final state.

Pions can also be produced via coherent production: a neutrino interacts with the whole Oxygen nucleus and produces a pion as follows:

$$\nu_x + {}^{16}\text{O} \rightarrow l_x + {}^{16}\text{O} + \pi\tag{3.12}$$

Deep Inelastic Scattering (DIS)

In DIS interactions, the incident neutrino interacts with a constituent quark in the target nucleon producing one or more hadrons:

$$\nu_x + N \rightarrow l_x + N' + \text{hadrons}\tag{3.13}$$

In NEUT the process is considered for the cases with hadronic invariant mass $W > 1.3 \text{ GeV}/c^2$ and becomes the dominant process for $W > 10 \text{ GeV}/c^2$. For $W < 2 \text{ GeV}/c^2$ NEUT considers only pions as produced hadrons, for $W > 2 \text{ GeV}/c^2$ NEUT considers the production of heavier mesons (K and η), as well, and simulates them using PYTHIA/JETSET [55].

3.2 Final State Interactions

The products of a simulated neutrino interaction are propagated through the nuclear matter they encounter along their path. Hadrons produced in neutrino interactions are known to interact with the nuclear medium: this means that the particles observed in the final state may differ from the particles produced in the primary interaction. These interactions between the produced hadrons and the nuclear medium are known as Final State Interactions (FSIs): since their products are revealed in the detector, indeed, it's very important to simulate them accurately. NEUT simulates the emissions due to de-excitation of nuclei left in an excited state after an interaction has happened as well.

Mesons and nucleons FSIs are simulated by NEUT using cascade models tuned with data from several scattering experiments [62].

3.2.1 Pion FSI

Pions are the most observed hadrons in SK. Pion FSI are simulated by the NEUT pion cascade model [5]: pions are propagated classically in finite steps through a nuclear medium described by the Woods-Saxon nuclear density profile [63], starting from the generation point in the simulated direction.

The nuclear medium density ρ , according to the Woods-Saxon model, is [56]:

$$\rho(r) = \frac{\rho(0)}{1 + \exp\left(\frac{r-a}{b}\right)} \quad (3.14)$$

where r is the distance from the nuclear center, $a = 2.69$ fm is the radius³ of ^{16}O , $b = 0.41$ fm is the nuclear surface thickness⁴ and $\rho(0) = 0.48 \text{ m}_\pi^3$ where m_π is the invariant mass of charged pions.

Because of the Pauli exclusion principle, the nucleon final state should have a larger momentum than the Fermi surface momentum $p_F(r)$:

$$p_F = \left(\frac{3}{2}\pi^2\rho(r)\right)^{\frac{1}{3}} \quad (3.15)$$

Both distributions are shown in Figure 3.4.

At each step the pion position is increased by a unit length: NEUT determines if any interaction happens for each step, according to interaction probabilities known from models and data from other experiments. The following interactions are possible:

- quasi elastic scattering in which a single pion of the same charge remains after the interaction;
- charge exchange in which a charged pion is converted into a π^0 and vice-versa;
- pion absorption in which no pions remain after the interaction;
- pion production in which multiple pions are produced.

If no interaction happens, the particle is moved again. This process proceeds until an interaction occurs or the pion is moved outside the nucleus.

³The radius of a nucleus is defined as the distance from the nuclear center where nuclear density is 50% of the maximum value.

⁴The nuclear surface thickness is defined as the thickness of the region of a nucleus where the nuclear density falls from 90% to 10% of its maximum value.

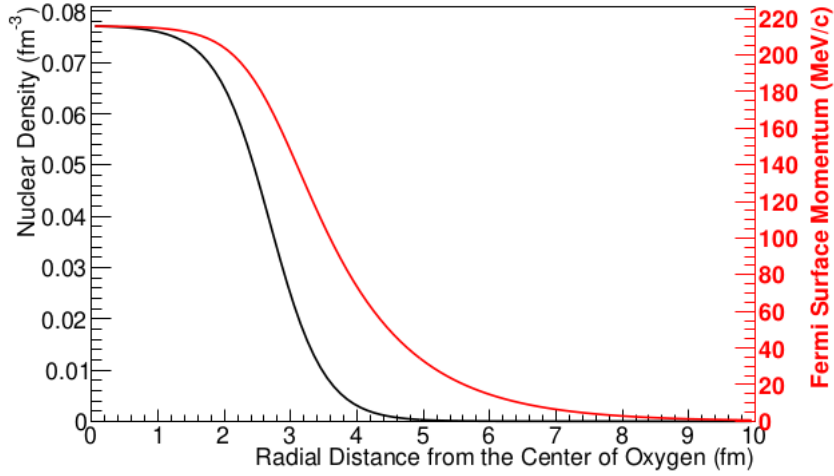


Figure 3.4: Nuclear density according to the Woods-Saxon model (in black) and the Fermi surface momentum (in red) as a function of the radial distance from the center of ^{16}O . Taken from [56].

3.3 Detector simulation

The information about the particles exiting the nucleus after a neutrino interaction simulated by NEUT is formatted in a vector and fed to a GEANT3-based [1] detector simulator, named SKDETSIM.

SKDETSIM simulates particle interactions with water, particle decays and Cherenkov photon production. The hadronic interactions of particles are simulated via GCALOR [65], except for pions below 500 MeV/c of momentum whose interactions are simulated via NEUT cascade model, as in Section 3.2.1.

The Cherenkov photons produced by the particles are propagated in the detector using a custom code which models the scattering, both Rayleigh and Mie components, and absorption in water.

Rayleigh scattering dominates for light wavelengths $\lambda < 450$ nm, it's symmetrical in the forward and backward directions with a characteristic λ^{-4} dependence and it's caused by small particles of radius $r \ll \lambda$. Mie scattering dominates for $\lambda > 450$ nm, it's asymmetrical with a sharp peak in the forward direction and it's caused by particles of radius $r \gg \lambda$ [56]. Water properties tuning in SKDETSIM is based on the results of the calibration procedures explained in Section 2.4.3.

The calibration results from the procedures explained in Section 2.4.4 and Section 2.4.2 are used to tune PMT and black sheet reflectivity and

individual PMTs responses in both charge and time, respectively.

The output of SKDETSIM has almost the same structure as observed data: it can be processed and analyzed in the same way but it comes with some additional structures containing the *Monte Carlo truth*, which is a list of the particles involved in the simulated event, their kinematic parameters, the position of their production and interaction vertexes and the kind of interactions they are subject to.

3.4 Generation of the Proton Decay (PDK) Monte Carlo sample

The sample used in this thesis contains a simulation of the following proton decay mode:

$$p \rightarrow \nu + K^+ \quad (3.16)$$

The simulated K^+ decay modes are:

$$K^+ \rightarrow \mu^+ + \nu \quad (3.17)$$

$$K^+ \rightarrow \pi^+ + \pi^0 \quad (3.18)$$

Both are contained in the sample: mode 3.18 is the subject of the analysis performed in this thesis.

Only protons from the Hydrogen nuclei, or *free protons*, and Oxygen nuclei, or *bound protons*, from the water molecules (H_2O) inside the tank are considered: this means that ten protons per water molecule are available for decay. The probability of decay is assumed to be the same for any proton, bound or free.

In the decay of a free proton, the ν and the K^+ are emitted back-to-back with a monochromatic momentum of 339 MeV/c in the laboratory frame [40].

Fermi momentum, correlation with other nucleons, nuclear binding energy and kaon-nucleon interactions are taken into account for bound protons.

The nucleon momentum in ^{16}O is simulated according to the results of the electron- ^{12}C scattering described in [13]. The binding energy is simulated as a Gaussian distribution and this effect is considered by subtracting the binding energy from the proton mass in the rest frame [56]. The mean and σ of the binding energy distributions are respectively 39.0 MeV/c and 10.2 MeV/c for the s-state and, respectively, 15.5 MeV/c and 3.82 MeV/c for the p-state. Both the momentum and the invariant mass distributions for simulated protons are shown in Figure 3.5.

The contribution from correlated decay protons is taken into account: when the wave function of a decaying proton is overlapped with the wave

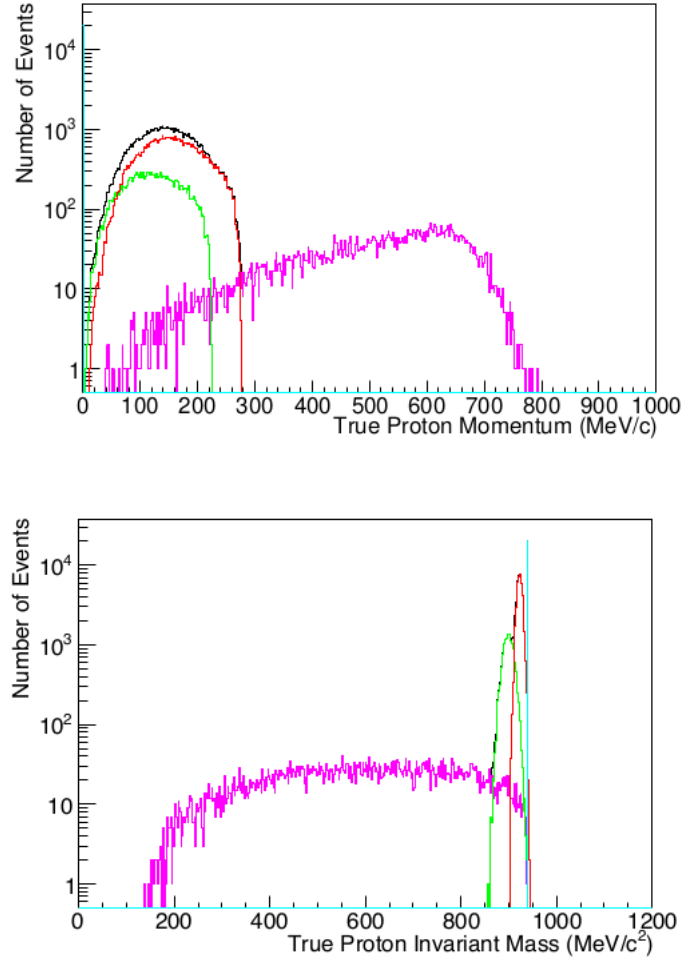


Figure 3.5: Distributions for the $p \rightarrow \nu + K^+$ decay simulation. The upper figure shows the simulated proton momentum and the lower figure shows the simulated proton invariant mass distributions in ^{16}O . The cyan, black, green, red and purple histograms correspond to free, bound, s-state, p-state and correlated decay protons, respectively. Taken from [56].

function of a spectator nucleon, the momentum of the decaying proton is changed. The predicted probability of correlated decay for a proton in ^{16}O is 10% [56].

The position of a decay nucleon inside Oxygen is simulated according to the Woods-Saxon nuclear density model, as explained in Section 3.2.1.

All the simulations described until this point are performed via a custom

software. After a proton decay event has been simulated, NEUT is used to propagate its products inside the nuclear medium and calculate FSIs as in Section 3.2.1. Finally SKDETSIM is used as in Section 3.3 to perform the simulation of the detector response.

Chapter 4

Reconstruction algorithms

Reconstruction algorithms extract information about visible particles in the events for physical analysis. Typical reconstructed information is the vertex of interaction, the number of Cherenkov rings produced in the ID, the type and momentum of visible particles. Two reconstruction algorithms are available in SK: *APFit* and *fiTQun*. In this analysis *fiTQun* is used to select signal events, aiming at understanding its performance with multi-ring events containing a charged pion ring, while *APFit* is used as a term of comparison and for validation since it's well known and reliable. In addition to these two algorithms, a neutron tagging algorithm (*Neut-Fit*) is used to count the number of neutrons emitted in a primary FC event.

4.1 Introduction: *APFit* and *fiTQun*

APFit is a sequential fitter that uses the time and charge information of hit PMTs. It was used for the discovery of neutrino oscillation and in K2K and T2K experiments. The growth of available computing power has led to the development of a different and more complex approach to event reconstruction: *fiTQun* is a maximum likelihood fitter that uses time and charge information of both hit and unhit PMTs. It was developed for the MiniBooNE experiment, a Cherenkov detector at Fermilab, whose main motivation is the study of neutrino oscillations, employing a spherical shaped container lined with 1280 PMTs and filled with a mix of mineral oils, where charged particles above Cherenkov threshold in oil are expected to produce photon rings as in SK. *FiTQun* was later adapted to SK for the T2K experiment, finally it's being used for SK analysis, including the search for proton decay. Generally speaking, *fiTQun* shows a better reconstruction performance than *APFit* [56] at the cost of a longer processing time per event. *fiTQun* can han-

up to six Cherenkov rings per event, each with its reconstructed vertex, and three Particle Identification (PID) hypotheses: electron/gamma, muon and charged pion. *APfit* can handle up to five rings with a single vertex per event and two PID hypotheses: electron/gamma and muon.

4.2 *APFit*

APFit performs these steps sequentially to reconstruct an event:

- vertex fitting;
- ring counting;
- particle identification;
- momentum determination;
- *Michel electron* search.

A complete reference on *APFit* can be found in [54].

4.2.1 Vertex fitting

The vertex fitting process consists of three steps:

- point-fit;
- search for the edge of the most energetic Cherenkov ring;
- Time-to-Digital Converter TDC-fit.

Point-fit

The point-fit assumes that Cherenkov light is emitted from a single vertex in water. For hypothesis \mathbf{x} of possible vertex, the time-of-flight (TOF) subtracted hit timing distribution is calculated: the vertexes that produce a narrower distribution are those closer to the true vertex as well. Hence, the point-fit vertex can be obtained by maximizing the following goodness function:

$$\text{goodness} = \frac{1}{N} \sum_i \exp \left(-\frac{(t_i(\mathbf{x}) - t_0)^2}{2(1.5\sigma)^2} \right) \quad (4.1)$$

where N is the number of hit PMTs, t_i is the TOF subtracted timing of the i -th PMT, t_0 is the interaction time maximizing the goodness, σ is the PMT timing resolution of 2.5 ns. The factor 1.5 at the denominator is chosen to optimize the fitting performance.

Ring edge search

This step aims at the determination of the edge and direction of the most energetic Cherenkov ring. Using the point-fit vertex and assuming a test direction, starting from the overall direction which is estimated by taking a charge-weighted sum of each ID PMT, the observed charge distribution $PE(\theta)$ in dependence of the opening angle θ can be calculated, as shown in Figure 4.1. The angle θ_{edge} corresponding to the ring edge satisfies the following conditions:

1. $\theta_{\text{edge}} > \theta_{\text{peak}}$
2. $\left[\frac{d^2 PE(\theta)}{d^2 \theta} \right]_{\theta=\theta_{\text{edge}}} = 0$

where θ_{peak} is the value of the angle corresponding to the maximum of $PE(\theta)$.

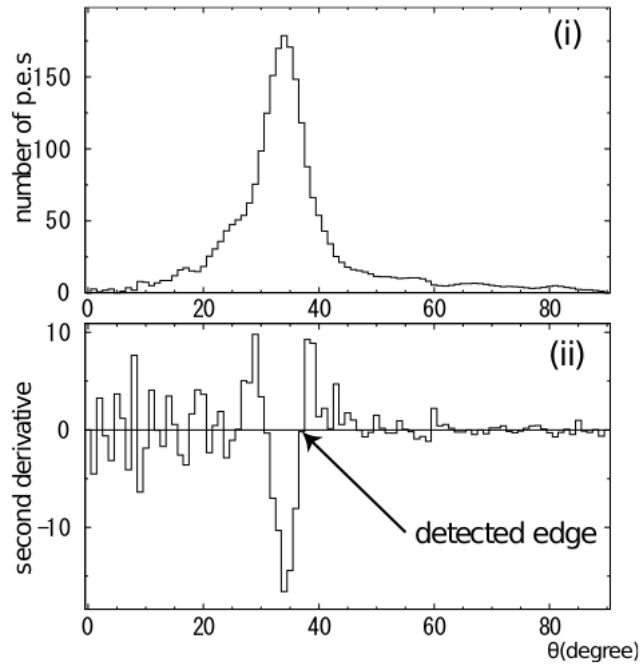


Figure 4.1: Observed charge distribution in dependence of the opening angle for a test direction as seen from the point-fit vertex (top) and its second derivative (bottom). Taken from [56].

By maximizing the following estimator $Q(\theta_{\text{edge}})$, the edge and the direc-

tion of the most energetic Cherenkov ring are determined:

$$Q(\theta_{\text{edge}}) = \frac{\int_0^{\theta_{\text{edge}}} \text{PE}(\theta) d\theta}{\sin \theta_{\text{edge}}} \left(\left[\frac{d\text{PE}(\theta)}{d\theta} \right]_{\theta=\theta_{\text{edge}}} \right)^2 \exp \left(-\frac{(\theta_{\text{edge}} - \theta_{\text{exp}})^2}{2\sigma_\theta^2} \right) \quad (4.2)$$

where θ_{exp} and σ_θ are the expected Cherenkov angle using the total charge inside the cone and its resolution, respectively. The charge in $\text{PE}(\theta)$ is corrected for attenuation and PMT angular acceptance.

TDC-fit

TDC-fit refines the vertex position estimate: the track length of the charged particle and the scattered Cherenkov photons are taken into account. The initial track length, assuming that 3 MeV/cm are deposited along it, is estimated from the total charge. The timing residual for PMTs inside the cone is calculated assuming the Cherenkov light is emitted along the track with the same angle. For PMTs outside the cone, the timing residual is calculated assuming that Cherenkov light is emitted at the vertex and considering the scattering parameters.

$$\begin{aligned} t_i &= t_i^0 - \frac{1}{c} \times |\vec{X}_i - \vec{O}| - \frac{n}{c} \times |\vec{P}_i - \vec{X}_i| && \text{PMTs inside the ring} \\ t_i &= t_i^0 - \frac{n}{c} \times |\vec{P}_i - \vec{O}| && \text{PMTs outside the ring} \end{aligned} \quad (4.3)$$

where \vec{O} is the vertex position, \vec{X}_i is the position at which Cherenkov photons are emitted toward the i^{th} PMT, n is the refractive index of water, \vec{P}_i is the position and t_i^0 is the hit timing of the i^{th} PMT. The final vertex of the most energetic ring is determined by maximizing an estimator.

4.2.2 Ring counting

This step aims at searching additional Cherenkov rings: candidate rings are found by a shape extraction algorithm known as the *Hough transform*, shown in Figure 4.2.

For each hit PMT a fake ring is projected onto the ID wall with a 42° opening angle calculated from the already fitted vertex. The intersection of these fake rings is the direction of a candidate Cherenkov ring: a log-likelihood method is used to accept or reject any candidate additional ring.

The likelihood function is defined as:

$$L_N = \sum_i \log \left(P \left(q_i^{\text{obs}}, \sum_{n=1}^N \alpha_n \cdot q_{i,n}^{\text{exp}} \right) \right) \quad (4.4)$$

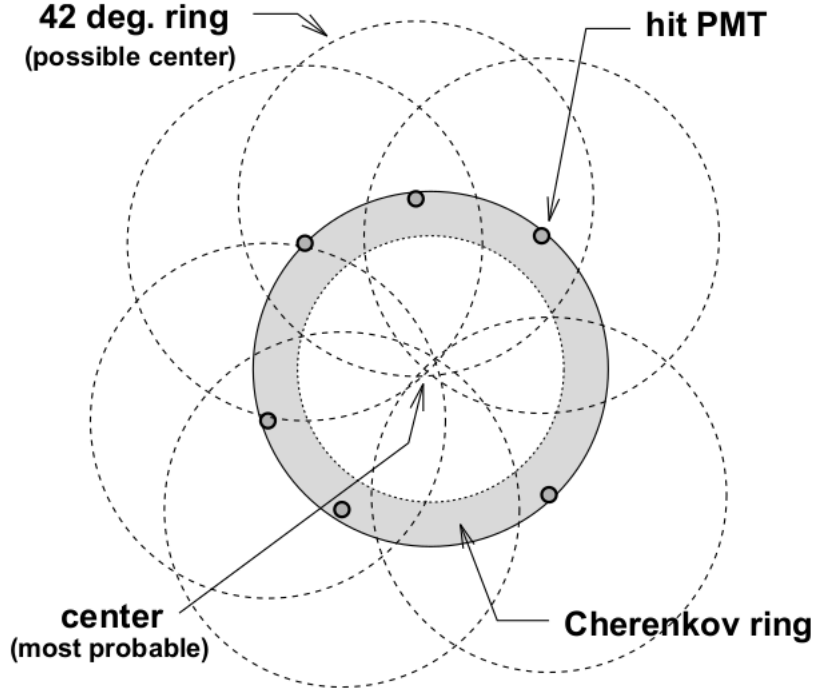


Figure 4.2: A schematic of the ring-finding procedure.

where i runs over all the indexes of the hit PMTs inside the N Cherenkov rings, q_i^{obs} is the observed charge in the i^{th} PMT, $\alpha_n \cdot q_{i,n}^{\text{exp}}$ is the expected charge in the i^{th} PMT from the n^{th} ring. The α_n factors are allowed to vary in order to maximize the likelihood with a minimum momentum constraint, applied to account for the charge produced in the hit PMTs. P is a gaussian probability density function:

$$P(q_i^{\text{obs}}, q_i^{\text{exp}}) = \frac{1}{\sqrt{2\pi\sigma^2}} \exp\left(-\frac{(q_i^{\text{obs}} - q_i^{\text{exp}})^2}{2\sigma^2}\right) \quad (4.5)$$

The hypothesis of $N+1$ rings is tested against the hypothesis of N rings: if no candidates satisfy $L_{N+1} \geq L_N$ the number of rings is finalized at N and the search stops. Otherwise, further processing is performed to choose the best-fit candidate. More details can be found in [59].

Figure 4.3 shows the ring counting likelihood distribution $L_2 - L_1$, calculated for the FCFV sub-GeV (visible energy < 1.33 GeV) sample of the data and the atmospheric neutrino MC for the L_2 hypothesis. *APFit* repeats the search for additional rings up to a maximum of five rings per event.

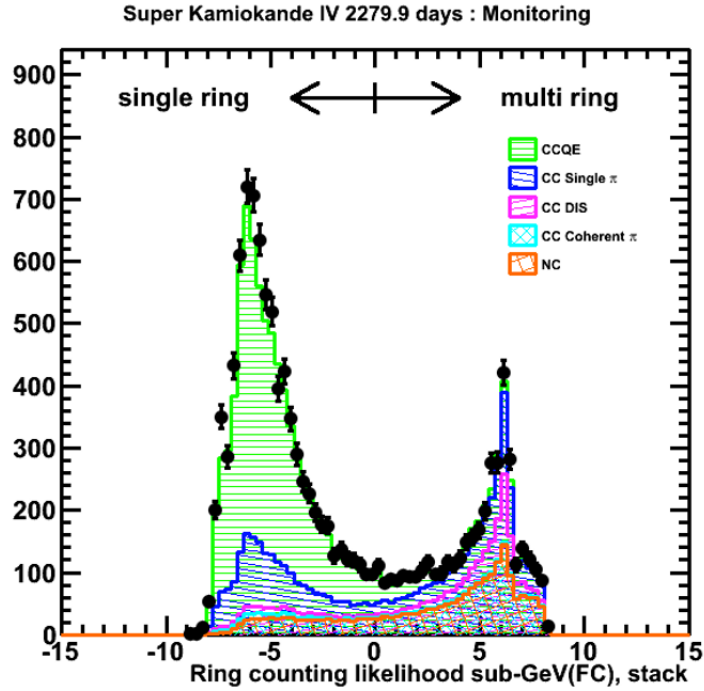


Figure 4.3: Ring counting likelihood distribution $L_2 - L_1$ for the FCFV sub-GeV sample of the data (black points) and the atmospheric neutrino MC (stacked histograms, normalized to data livetime) in SK-IV. Events with no Michel electrons tagged are selected. The events in the positive likelihood side are tagged as multi-ring, conversely those in the negative likelihood side are tagged as single-ring.

4.2.3 Particle Identification (PID)

The reconstructed Cherenkov rings are processed by a Particle Identification (PID) classifier under two available hypotheses: an e-like ring hypothesis, suitable for rings produced by gammas or electrons and a μ -like hypothesis suitable for rings produced by muons, charged pions or protons.

High-energy electrons produce electromagnetic showers due to the chain of bremsstrahlung ($e^\pm \rightarrow e^\pm \gamma$) and photon pair production ($\gamma \rightarrow e^+ e^-$). Photons can start the same process via pair production as well. The resulting Cherenkov ring is the sum of several rings produced by the charged component of these showers, all approximately in the same direction: for this reason e-like rings have diffuse edges.

Muons have a mass ~ 200 times the mass of electrons, for this reason their

bremsstrahlung cross-section is negligibly small¹: muon-like rings have sharp, thick edges, since they are produced by a single particle emitting Cherenkov light along its track.

Charged mesons can also interact hadronically, so their direction can suddenly change: this leads to the production of one or more distinct thinner rings, with respect to muons, with sharp edges due to the absence of electromagnetic showers.

Some differences come from the angles of Cherenkov emission: high-energy electrons usually have a 42° Cherenkov opening angle, corresponding to $\beta_e \simeq 1$, since they are always highly relativistic. Muons aren't always highly relativistic ($\beta_\mu = \frac{v}{c} \leq \beta$) and lose energy due to ionization, so their Cherenkov angle can be less than 42° and may shrink during the emission, as shown in Figure 4.4.

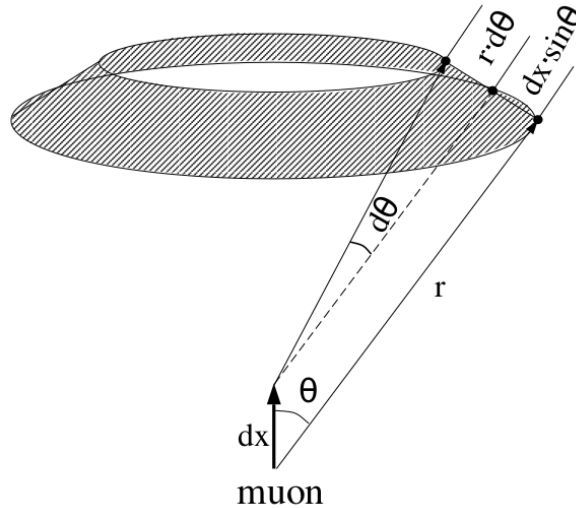


Figure 4.4: A schematic view of Cherenkov radiation from a muon. Cherenkov photons are emitted to the area of $2\pi r \sin \theta(dx \sin \theta + rd\theta)$ while a muon travels the distance of dx .

Figure 4.5 shows the different shapes of typical e-like and μ -like rings: these differences are exploited by the PID algorithm to classify the processed rings.

A likelihood test based on the observed and expected charge for each ring is performed. The expected charge is evaluated from Monte Carlo simulations using a test vertex placed at a distance of $R = 16.9$ m from the ID wall and

¹Bremsstrahlung cross-section for a particle of mass m is proportional to $\frac{1}{m^2}$.

it has the following form for e-like and μ -like rings respectively:

$$q_{\text{exp},i}(e) = \alpha_e Q_{\text{exp}}(p_e, \theta_i) \left(\frac{R}{r_i} \right)^{\frac{3}{2}} e^{-\frac{r_i}{L}} f(\Theta_i) + q_{\text{scat},i} \quad (4.6)$$

$$q_{\text{exp},i}(\mu) = \left(\frac{\alpha_\mu \sin^2 \theta_{x_i}}{r_i \left(\sin \theta_{x_i} + r_i \left[\frac{d\theta}{dx} \right]_{x=x_i} \right)} + q_{\text{knock},i} \right) e^{-\frac{r_i}{L}} f(\Theta_i) + q_{\text{scat},i} \quad (4.7)$$

where α_e and α_μ are normalization factors, $Q_{\text{exp}}(p_e, \theta_i)$ is the expected charge distribution depending on the electron momentum p_e and the angle θ_i for the i^{th} PMT, r_i is the distance between the ring vertex and the i^{th} PMT, L is the light attenuation length in water, $f(\Theta_i)$ is the angular acceptance as a function of the photon incidence angle Θ_i for the i^{th} PMT, $q_{\text{scat},i}$ is the expected charge due to scattered light for the i^{th} PMT, x_i is the estimated point on the muon track from which photons detected by the i^{th} PMT were received, θ_{x_i} is the Cherenkov angle of a muon track length at x_i , $q_{\text{knock},i}$ is the expected charge due to *knock-on electrons*, i.e. electrons produced by the muon ionization in water, for the i^{th} PMT.

A gaussian probability density is calculated as in Equation 4.5 and fed to a likelihood function. The final probability density P takes into account the variation of the Cherenkov angle of emission, too [35].

The PID likelihood function is given as:

$$L_{\text{PID}} = \sqrt{-\log P(\mu)} - \sqrt{-\log P(e)} \quad (4.8)$$

The single-ring and multi-ring L_{PID} distributions for SK-IV are shown in Figure 4.6.

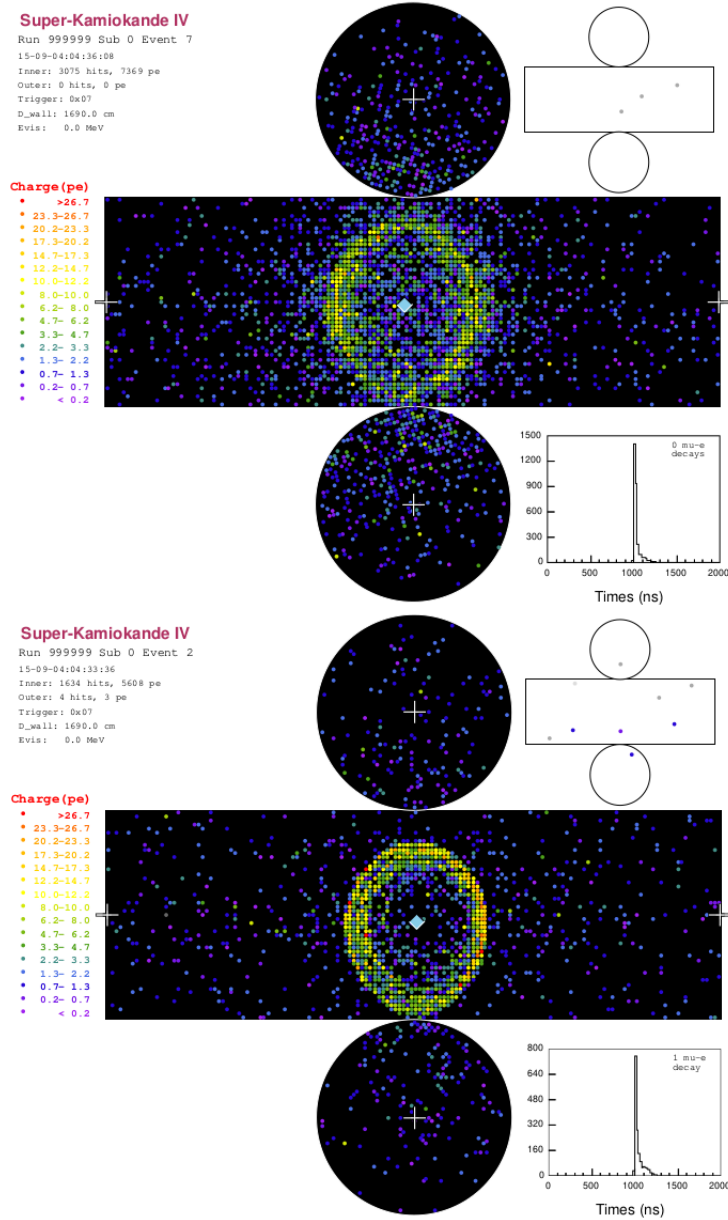


Figure 4.5: Display of Monte Carlo simulated e-like (top) and mu-like (bottom) rings from an e^+ and a μ^+ respectively, with a momentum of 800 MeV/c both. The intensity scale shows the amount of charge produced in each PMT. The main display shows the ID while the small display on the top right shows the OD, whose negligible activity is compliant with the FC event definition. The timing distributions for both the events is also reported at the bottom right corner of each ID displays.

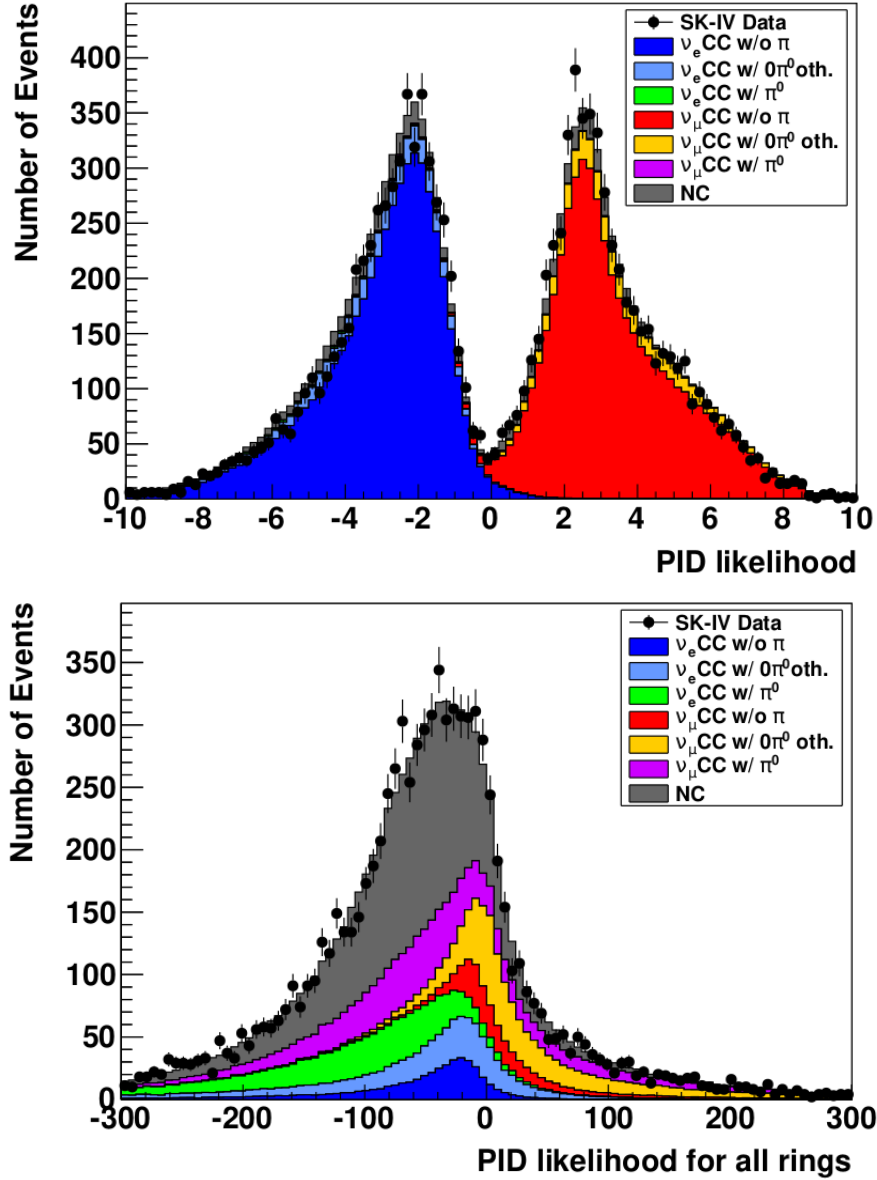


Figure 4.6: PID likelihood distributions for the FCFV sub-GeV single-ring (top) and multi-ring (bottom) sample of the data (black points) and the atmospheric neutrino MC (stacked histograms, normalized to data livetime) in SK-IV. The events in the positive side are identified as μ -like events. Conversely, the events in the negative side are identified as e-like.

4.2.4 Momentum determination

The momentum of each particle is evaluated by the observed charge inside the Cherenkov cone with a half angle of 70° . The observed charge of the i^{th} PMT for the n^{th} ring is separated based on the expected charge distributions from each ring, described as follows:

$$q_{\text{obs},i,n} = q_{\text{obs},i} \frac{q_{\text{exp},i,n}}{\sum_{n'} q_{\text{exp},i,n'}} \quad (4.9)$$

The total charge for each ring (RTOT) is calculated as follows:

$$RTOT = \frac{G_{\text{MC}}}{G_{\text{Data}}} \left[\alpha \sum_{\substack{\theta_{i,n} < 70^\circ \\ -50\text{ns} < t_i < 250\text{ns}}} \left(q_{\text{obs},i,n} e^{\frac{r_i}{L} \cos \Theta_i} \frac{1}{f(\Theta_i)} \right) - \sum_{\theta_i < 70^\circ} S_i \right] \quad (4.10)$$

where G_{MC} and G_{Data} are the relative PMT gain parameters for the data and the Monte Carlo simulation, α is a normalization factor, r_i is the distance between the ring vertex and the i^{th} PMT, L is the light attenuation length in water, $f(\Theta_i)$ is the angular acceptance as a function of the photon incidence angle Θ_i for the i^{th} PMT, $\theta_{i,n}$ is the angle between the i^{th} PMT and the n^{th} ring direction, t_i is the TOF subtracted hit timing of the i^{th} PMT, S_i is the expected charge of the i^{th} PMT due to scattered light.

RTOT is converted to the corresponding momentum according to conversion tables obtained from Monte Carlo simulations for both the e-like and μ -like hypotheses: Figure 4.7 shows that momentum dependence on RTOT is quite linear.

4.2.5 Michel electron search

Michel electrons are an indicator of the presence of a muon. The tagging of *Michel electrons* is based on the number of hits in a cluster, the total charge and the goodness of the vertex fit.

4.3 *fiTQun*

fiTQun is based on the maximization of a likelihood function. The reconstruction procedure consists of the following steps:

- vertex pre-fitting;
- hit clustering;

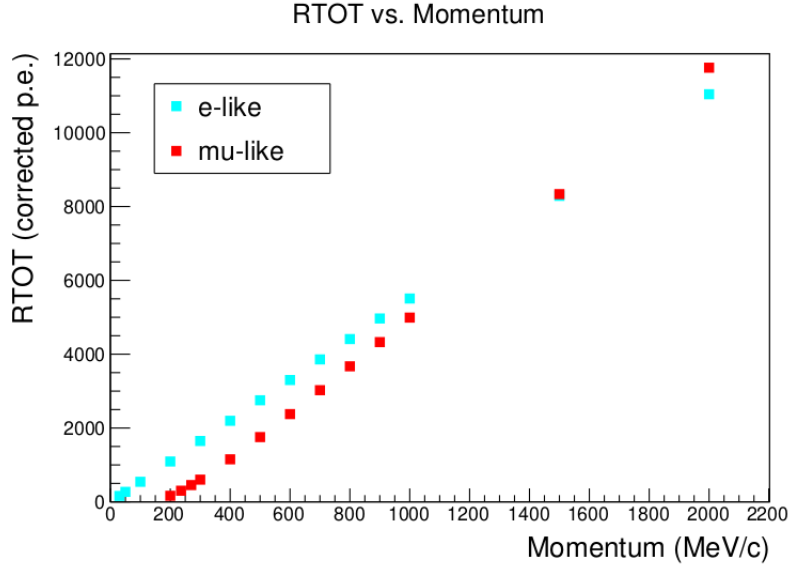


Figure 4.7: Distributions of RTOT as a function of momentum up to 2000 MeV/c for both e-like and μ -like rings.

- single-ring fitting;
- multi-ring fitter.

Detailed information about *fiTQun* can be found in [56] and [62].

4.3.1 The likelihood function

The likelihood function to be maximized by *fiTQun* is defined as:

$$L(\mathbf{x}) = \prod_j^{\text{unhit}} P_j(\text{unhit}|\mathbf{x}) \prod_i^{\text{hit}} [1 - P_i(\text{unhit}|\mathbf{x})] f_q(q_i|\mathbf{x}) f_t(t_i|\mathbf{x}) \quad (4.11)$$

where \mathbf{x} is an event hypothesis consisting of particle types, vertexes and momenta.

The index j runs over all unhit PMTs, conversely the index i runs over all hit PMTs: for each of the hit ones, information about the charge produced and the time of arrival of the first incident photon is stored in the event data structures. $P_i(\text{unhit}|\mathbf{x})$ is the conditioned probability the i^{th} PMT does not register a hit for the given hypothesis \mathbf{x} , q_i and t_i represent the charge and time information registered by the i^{th} hit PMT, $f_q(q_i|\mathbf{x})$ and $f_t(t_i|\mathbf{x})$ are the

conditioned probability density functions of observing charge q_i and time t_i respectively in the i^{th} hit PMT for the given hypothesis \mathbf{x} . *fitQun* searches for the hypothesis \mathbf{x} which maximizes $L(\mathbf{x})$ and uses it as the best estimate for the particle configuration in the event.

4.3.2 Predicted charge

Predicted charges μ_i are introduced to decouple the process of particle and optical propagation inside the tank from the response of the PMTs. μ_i is defined as the mean number of photoelectrons produced in the i^{th} PMT for a given hypothesis from which it explicitly depends. Equation 4.11 becomes:

$$L(\mathbf{x}) = \prod_j^{\text{unhit}} P_j(\text{unhit}|\mu_j) \prod_i^{\text{hit}} [1 - P_i(\text{unhit}|\mu_i)] f_q(q_i|\mu_i) f_t(t_i|\mathbf{x}) \quad (4.12)$$

Likelihood is evaluated in two steps:

1. for a given hypothesis \mathbf{x} the predicted charge μ_i is calculated for each PMT;
2. using the calculated μ_i and the observed information, the likelihood function (Equation 4.12) is evaluated.

For a multi-particle hypothesis, the predicted charges for each particle are calculated separately and then summed. If n is the number of particles, the total predicted charge is calculated as follows:

$$\mu_i = \sum_n (\mu_{i,n}^{\text{dir}} + \mu_{i,n}^{\text{sct}}) + \mu^{\text{dark}} \quad (4.13)$$

where μ^{dark} is the contribution from the PMT dark current, $\mu_{i,n}^{\text{dir}}$ and $\mu_{i,n}^{\text{sct}}$ are the contributions from direct light and scattered light incident on the i^{th} and due to the n^{th} particle. For a single particle hypothesis, μ^{dir} and μ^{sct} are given as integrals along the particle track length s from its initial position.

$$\mu^{\text{dir}} = \Phi(p) \int g(p, s, \cos \theta) \Omega(R) T(R) \epsilon(\eta) ds \quad (4.14)$$

$$\mu^{\text{sct}} = \Phi(p) \int \frac{1}{4\pi} \rho(p, s) \Omega(R) T(R) \epsilon(\eta) A(s) ds \quad (4.15)$$

where the variables θ , R and η indicate the relative orientation of the particle and the PMT in dependence on s , as shown in Figure 4.8. $\Phi(p)$ is a normalization factor which is proportional to the average total number of photons for a particle with initial momentum p . The other factors are explained in the following paragraphs.

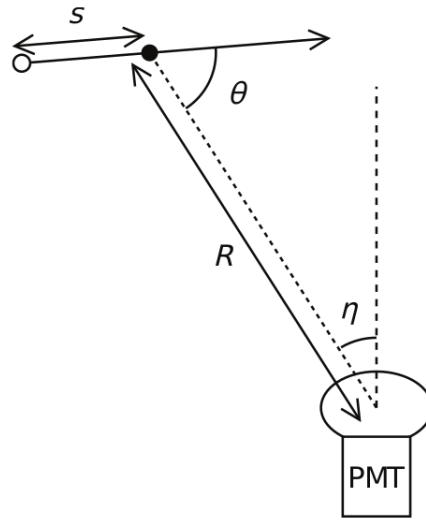


Figure 4.8: Reference diagram of the variables for the predicted charge calculations in Equations 4.14 and 4.15. The vertex position of the particle is shown as the white dot.

Cherenkov emission profile

The Cherenkov emission profile g is defined as the number of photons per unit track length per unit solid angle, at angle θ with respect to the particle direction, emitted by a particle with initial momentum p . g is normalized as:

$$\int g(p, s, \cos \theta) ds d\Omega = 1 \quad (4.16)$$

Electron and muon Cherenkov emission profiles simulated in SKDETSIM for four different values of initial momentum each are shown in 4.9 and 4.10 respectively. *fiTQun* exploits their differences for PID.

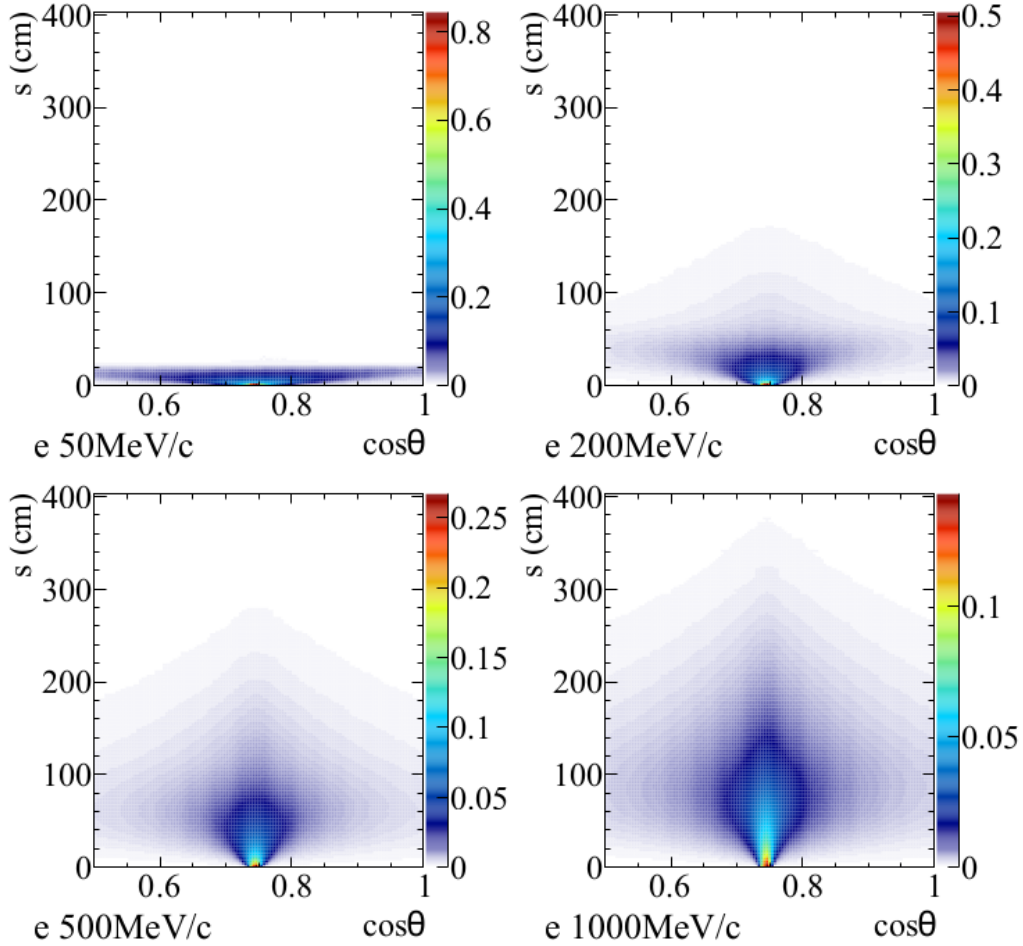


Figure 4.9: Cherenkov emission profiles for electrons at various initial momenta, simulated in SKDETSIM. The emission has a peak near $\cos\theta = 0.75$, corresponding to $\sim 42^\circ$, which is the Cherenkov emission angle for a particle with $\beta \simeq 1$ in water. This happens for all the initial momentum values, since they are far beyond the ultra-relativistic threshold for electrons. The broadening of the angle distribution is due to electromagnetic showering.

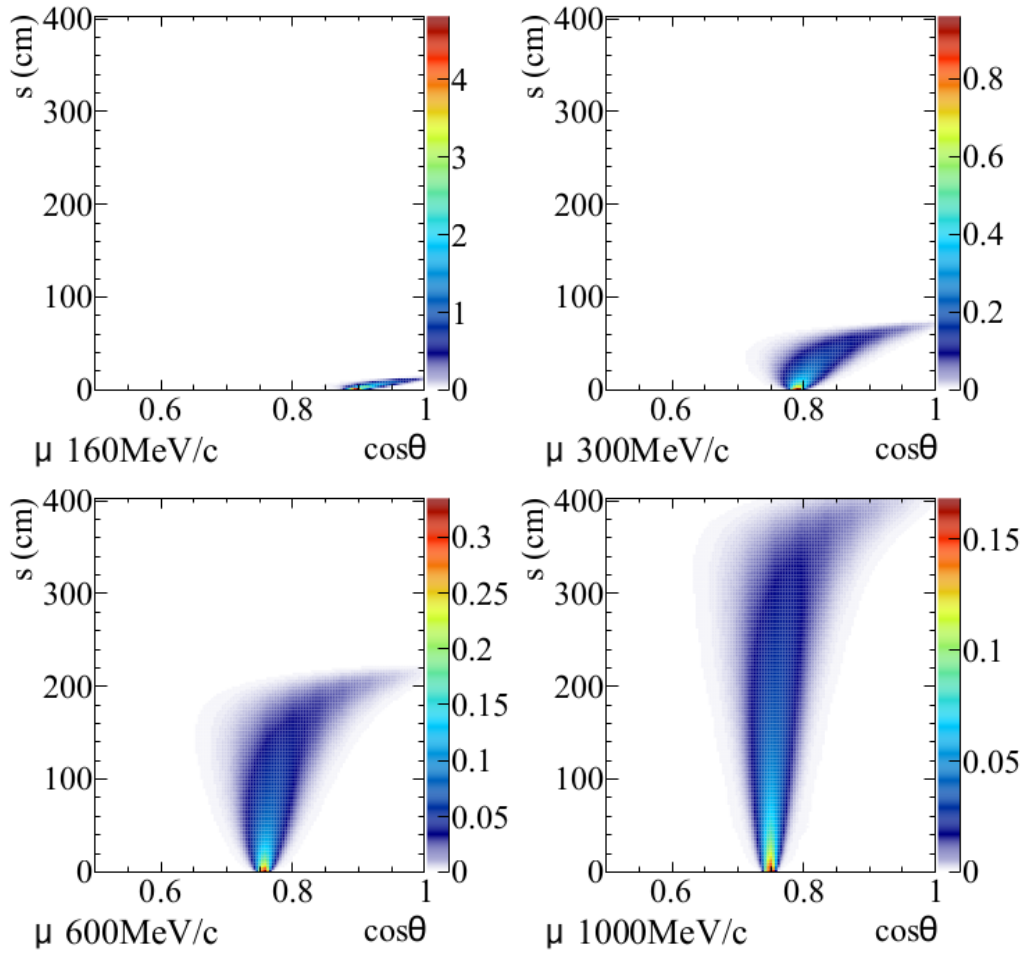


Figure 4.10: Cherenkov emission profiles for muons at various initial momenta, simulated in SKDETSIM. As the initial momentum grows, the initial emission angle approaches the theoretical value of 42° for a particle of $\beta \simeq 1$ in water. The angle distribution is sharper than in the electron case due to the absence of electromagnetic showering. Finally, muons lose energy due to ionization, causing their average Cherenkov emission angle to shrink along their tracks.

Solid angle $\Omega(R)$

The PMT sensitive area subtends a solid angle from the particle position on the track which can be roughly evaluated, for $R > 1$ m, as:

$$\Omega(R) = \frac{\pi a^2}{R^2 + a^2} \quad (4.17)$$

where a is the radius of an ID PMT (0.254 m).

Light transmission factor $T(R)$

The factor $T(R)$ takes the absorption and scattering of the emitted Cherenkov light in water into account. It is evaluated as:

$$T(R) = \exp\left(-\frac{R}{L^{\text{att}}}\right) \quad (4.18)$$

where L^{att} is the light attenuation length in water used in SKDETSIM (74.9646 m for SK-IV).

PMT angular acceptance $\epsilon(\eta)$

The PMT angular acceptance $\epsilon(\eta)$ is obtained from SKDETSIM and fitted by a polynomial function which is used in the predicted charge calculation as $\epsilon(\eta)$, normalized in order to satisfy the condition $\epsilon(0) = 1$ (Figure 4.11).

Light scattering and reflection: $A(s)$

The $A(s)$ factor takes into account the indirect light caused by light scattering and reflection happening inside the detector. It is evaluated as:

$$A(s) = \frac{d\mu^{\text{sct}}}{d\mu^{\text{iso,dir}}} \quad (4.19)$$

where $\mu^{\text{iso,dir}}$ is the predicted charge due to an hypothetical isotropic light source traveling along the same track as the actual particle with a total light intensity same as that producing μ^{dir} , which is obtained by removing $A(s)$ from Equation 4.15 and defining $\rho(p, s)$ as follows:

$$\rho(p, s) \equiv \int g(p, s, \cos \theta) d\Omega \quad (4.20)$$

Finally, tables containing the numerical values of $A(s)$ are generated by SKDETSIM simulations.

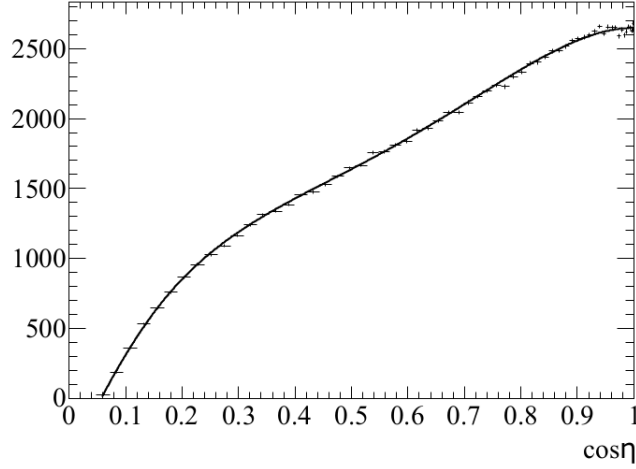


Figure 4.11: PMT angular acceptance as a function of $\cos \eta$ obtained from SKDETSIM. The vertical axis is in arbitrary unit. The solid line shows a fitted polynomial function and it is normalized to be 1 at $\eta = 0$.

4.3.3 Unhit probability

The number of photoelectrons produced in a PMT follows a Poisson distribution whose mean μ is the total predicted charge defined in Equation 4.13. According to Poisson distribution, the probability that k photoelectrons are produced if the mean number is μ is:

$$P(k) = \frac{\mu^k}{k!} e^{-\mu} \quad (4.21)$$

Hence, the probability of no photoelectron is $e^{-\mu}$. Due to the threshold of the PMT signal, a photoelectron might not surpass the threshold and make a hit. This threshold effect is corrected up to the third order of μ as follows:

$$P(\text{unhit}|\mu) = (1 + a_1\mu + a_2\mu^2 + a_3\mu^3) e^{-\mu} \quad (4.22)$$

where the coefficients a_n are obtained from SKDETSIM.

4.3.4 Charge likelihood

The charge likelihood $f_q(q|\mu)$ is the conditional probability to observe a charge q in the considered PMT, given the hypothesis that its predicted charge is μ . In order to obtain $f_q(q|\mu)$, normalized observed charge distributions are prepared by generating photoelectrons according to a Poisson

distribution with discrete values of μ at each PMT in SKDETSIM. Then, those distributions are fitted by a polynomial as a function of μ at each fixed value of q . The final polynomial is obtained after a linear interpolation of the fit parameters in terms of the observed charge q .

4.3.5 Time likelihood

The time likelihood $f_t(t_i|\mathbf{x})$ depends on the event hypothesis \mathbf{x} and the position of the PMT. However, it is impractical to completely consider such complex dependencies. In order to approximate $f_t(t_i|\mathbf{x})$, we assume that all Cherenkov photons are emitted at the midpoint of the particle track, and then the time likelihood can be expressed by the residual hit time given as:

$$t_i^{\text{res}} = t_i - t - s_{\text{mid}}/c - |\mathbf{R}_{\text{PMT}}^i - \mathbf{x} - s_{\text{mid}}\mathbf{d}|/(c/n) \quad (4.23)$$

where t_i , $\mathbf{R}_{\text{PMT}}^i$ are the raw hit time and position of the i^{th} PMT, \mathbf{x} , t are the vertex position and time, \mathbf{d} is the particle direction and s_{mid} is the half of the particle track length. For a single particle hypothesis, by using t_i^{res} , time likelihoods for the direct and indirect light are obtained by SKDETSIM and the final likelihood is obtained by merging those two likelihoods as described below:

$$f_t(t_i^{\text{res}}) = \omega f_t^{\text{dir}}(t_i^{\text{res}}) + (1 - \omega) f_t^{\text{sct}}(t_i^{\text{res}}) \quad (4.24)$$

where

$$\omega = \frac{1 - e^{-\mu_i^{\text{dir}}}}{1 - e^{-\mu_i^{\text{dir}}} e^{-\mu_i^{\text{sct}}}} \quad (4.25)$$

i.e. assuming that a hit is produced by an indirect photon if there is no direct photon. For a multi-particle hypothesis, the t_{res} for each particle hypothesis are calculated separately. The particles are ordered by t_i^{res} and the total time likelihood is calculated as:

$$\begin{aligned} f_t(t_i^{\text{res}}) = & \frac{1}{1 - \prod_{j=1}^{\text{all}} e^{-(\mu_{i,j}^{\text{dir}} + \mu_{i,j}^{\text{sct}})}} \\ & \times \sum_{j=1}^{\text{all}} \left[\left(\prod_{k=1}^{j-1} e^{-\mu_{i,k}^{\text{dir}}} \right) \left(1 - e^{-\mu_{i,j}^{\text{dir}}} \right) f_{t,j}^{\text{dir}}(t_i^{\text{res}}) \right. \\ & \left. + \left(\prod_{k=1}^{\text{all}} e^{-\mu_{i,k}^{\text{dir}}} \right) \left(\prod_{k=1}^{j-1} e^{-\mu_{i,k}^{\text{sct}}} \right) \left(1 - e^{-\mu_{i,j}^{\text{sct}}} \right) f_{t,j}^{\text{sct}}(t_i^{\text{res}}) \right] \end{aligned} \quad (4.26)$$

4.3.6 Vertex pre-fitting

The maximization of $L(\mathbf{s})$ must be initialized with a single starting vertex position as close as possible to the best-fit value, in order to prevent *fitQu*

to get stuck in a local maximum instead of the global one. The pre-fitting process calculates this initial *seed* value: assuming that all photons are emitted from a point-like light source, the *seed* is estimated by maximizing the following goodness function:

$$G(\mathbf{x}, t) = \sum_i^{\text{hit}} \exp \left[-\frac{1}{2} \left(\frac{T_{\text{res}}^i}{\sigma} \right)^2 \right] \quad (4.27)$$

where the residual hit time for the i^{th} T_{res}^i is calculated as:

$$T_{\text{res}}^i = t_i - t - |\mathbf{R}_{\text{PMT}}^i - \mathbf{x}|/(c/n) \quad (4.28)$$

A grid scan in the space of \mathbf{x} , t is iteratively done for the goodness while shrinking the grid size and σ .

4.3.7 Hit clustering

The time window for an event is $\sim 10 \mu\text{s}$ around an event trigger: it's wide enough for multiple hit clusters to be detected within the same event. For example, a *Michel electron* produced by a muon in the primary event is counted as a *sub-event* since it's typically detected after $\sim 2 \mu\text{s}$ from the trigger time, which is long enough to produce two separable hit clusters in time. The hit clustering algorithm is performed before the maximum likelihood reconstruction step, in order to keep the *sub-events* well separated.

The goodness function $G(\mathbf{x}, t)$ defined in Equation 4.27 is evaluated, in the vertex position returned by the pre-fitting procedure, every 8 ns step, starting at 300 ns before the trigger and using all the hits in the interval (-200 ns, 15000 ns) around the trigger, with an optimized $\sigma = 6.3$ ns. An example of the goodness distribution as a function of t for an event with a primary muon and a *Michel electron* is shown in Figure 4.12.

The goodness peak is identified by using a goodness threshold curve function. A time window is set around each peak found, containing only the hits that belong to it. The hits outside the time window are considered as un-hit in the likelihood calculation. The residual time is re-evaluated for the peak time and then the time window is defined as $-180 \text{ ns} < T_{\text{res}}^i < 800 \text{ ns}$. Overlapping time windows are merged together. Finally, the vertex pre-fitting procedure and the peak search are repeated to improve peak-finding precision. The final time windows are fixed for each remaining peak and the maximum likelihood reconstruction is done in each of them.

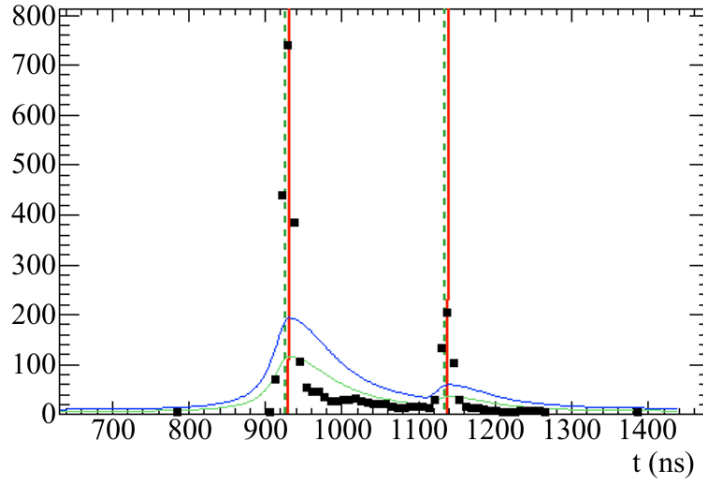


Figure 4.12: Goodness distribution as a function of hit time for an event with a parent muon and a *Michel electron*. The dots show the scanned goodness points. The blue and green curves are the goodness threshold functions which are used to determine the event time indicated by the red lines. The green dotted lines are for the true time for each particle: they are consistent with the peaks.

4.3.8 Single-ring fitter

After the hit-clustering step, the *sub-events* contained in an event are defined, ready to be processed by the reconstruction algorithms. The single-ring fitter is the most basic reconstruction algorithm available. For each *sub-event* it is applied to, it maximizes the likelihood $L(\mathbf{x})$ in order to obtain the best-fit single-particle hypothesis \mathbf{x} . *fitQun* considers three types of single-ring hypotheses: electron, muon and charged pion. Three fits are applied to every *sub-event*, one per hypothesis type.

Single-ring electron and muon fit

Both single-ring electron and muon hypothesis contain seven parameters: the vertex position \vec{x} , the time t , the zenith angle and azimuth of the direction (θ, ϕ) respectively, and the momentum p .

The single-ring electron fit starts by setting the vertex initially at the position determined by the vertex pre-fitting procedure and the time to the peak time. In order to determine the initial value for the direction, a likelihood scan of the direction is performed by sampling the likelihood at 400 points that are equally spaced on the unit sphere. During the direction scan,

momentum is fixed at the value which is roughly estimated using the total observed charge. After the direction is determined by the grid scan, the momentum *seed* value is set by performing another likelihood scan by only varying the momentum.

Once all the seven track parameters are seeded, the parameters are then simultaneously fit by minimizing the $-\ln L(\mathbf{x})$ in Equation 4.11 using the SIMPLEX algorithm in the MINUIT package, which provides the final maximum likelihood estimation of the particle track parameters assuming a single electron.

After that, the single-ring muon-fitter is applied to the same *sub-event*, assuming the vertex, time and direction from the electron fit as their *seed* values. The momentum is then estimated by a likelihood scan as in the electron fit, after which the full simultaneous minimization of the $-\ln L(\mathbf{x})$ is performed.

e/μ Particle Identification

The Particle Identification (PID) process between the e and μ hypotheses exploits the differences between e -like and μ -like rings already explained in Section 4.2.3. Since the likelihood function in Equation 4.12 embeds the different emission profiles for electrons and muons via the evaluation of the predicted charge (Section 4.3.2), in *fitQun* PID is done by comparing the best-fit likelihood values between different particle hypotheses.

In this case, electrons and muons are distinguished by making a cut on $\ln(L_e/L_\mu)$, the log-likelihood ratio between the best-fit electron and muon hypotheses, as shown in Figure 4.13.

The cut is evaluated by processing the FC true-FV CCQE event sample in the atmospheric neutrino Monte Carlo and set at:

$$\ln(L_e/L_\mu) > -10 \quad (4.29)$$

If this condition is satisfied, the ring is of electron, or showering, type. Otherwise it is of muon, or non-showering, type.

π^+ hypothesis

A π^+ propagating in water can interact hadronically with the nuclei contained in the surrounding molecules: this results in a sudden change of direction, due to hard scattering, or even absorption. The portion of the π^+ trajectory before such an interaction is known as the *upstream track*: the ring emitted in this part of the track is usually quite distinct from that of electrons being thinner and sharper but very similar to that of muons due to the absence of

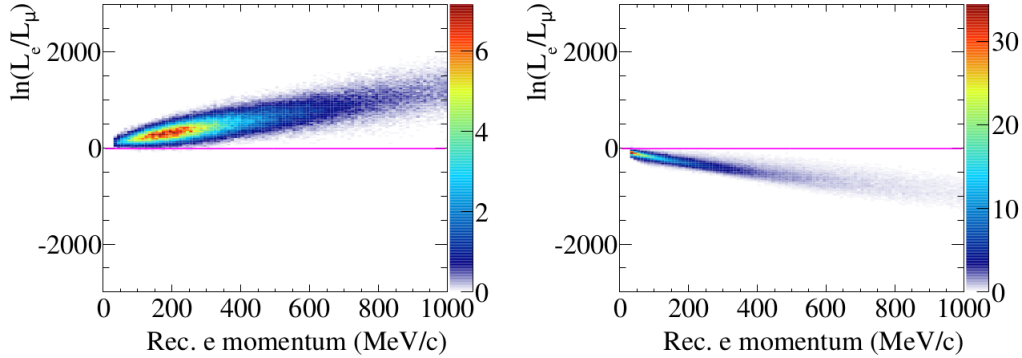


Figure 4.13: Likelihood separation of single-ring electron (left) and muon (right) events in the FC true-FV CCQE event sample in the atmospheric neutrino Monte Carlo. The vertical axes are $\ln(L_e/L_\mu)$ and the horizontal axes are the reconstructed single-ring electron fit momentum. The magenta lines indicate the cut criteria for electron-muon separation.

electromagnetic showers. If a chain of hadronic interactions happens, several upstream rings may be produced in the event. Finally, the remaining part of the track is known as the *downstream track*: a Cherenkov ring may be emitted from this part as well, if the necessary conditions are met (Figure 4.14).

The single-ring π^+ fitter reconstructs the upstream ring using the single-ring muon fit result as a *seed*. The predicted charge of the *upstream track* is obtained by subtracting the predicted charge of the *downstream track* from the predicted charge of an imaginary full track without any hadron interaction happening.

π^+ hypothesis contains the same parameters as the electron and muon ones, plus an additional fit parameter E_{loss} which is defined as the kinetic energy deposit in the *upstream track*.

Using E_{loss} , the vertex of the *downstream track* is calculated by assuming constant kinetic energy loss per unit track length. For the time likelihood, the residual time is estimated using the midpoint of the *upstream track*. All eight parameters of the *upstream track* are simultaneously fitted by minimizing $-\ln L$.

μ/π^+ identification

Since muons and charged pions have similar masses, in absence of any hadronic interaction, they produce similar ring patterns. The single-ring π^+ fitter,

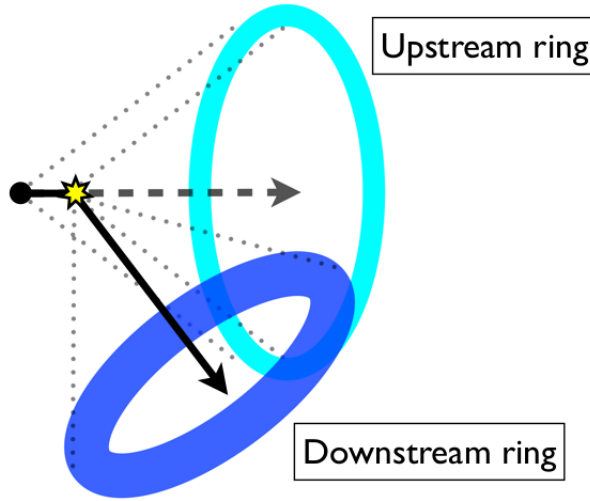


Figure 4.14: Schematic of the rings produced by a π^+ before and after hadronic scattering on a nucleus in water.

however, can distinguish between the two types of rings by a likelihood-ratio value test, which includes the π^+ specific E_{loss} parameter.

As Figure 4.15 shows, the separation between muons from ν_μ CCQE and pions NC π^+ in the T2K experiment² accelerator neutrino Monte Carlo simulation is not as sharp as in the e/μ case: although there are some indistinguishable events, a significant fraction of about 60% of π^+ events can be separated from muons. The π^+ hypothesis performance in fitting muon rings improves as E_{loss} grows, reaching the top when the particle momentum at the assumed *upstream track* endpoint drops below Cherenkov threshold.

4.3.9 Multi-ring fitter

fitQun multi-ring fitter can reconstruct multi-particle events containing up to six Cherenkov rings, like those ones relevant for this analysis.

The multi-ring fitter is applied only to the first *sub-event*, as defined in Section 4.3.7 since it's very unlikely that any subsequent *sub-event* carries more than one ring.

The fitting procedure considers only two hypotheses: electron, for showering particles like gammas and electrons, and π^+ , for non showering particles.

²Tokai-to-Kamioka (T2K) is an experiment which consists in sending a beam of ν_μ with a narrow energy distribution peaked at ~ 600 MeV from the town of Tokai to Super-Kamiokande for detection, along a path ~ 200 km long through the Earth, in order to study neutrino flavor oscillations.

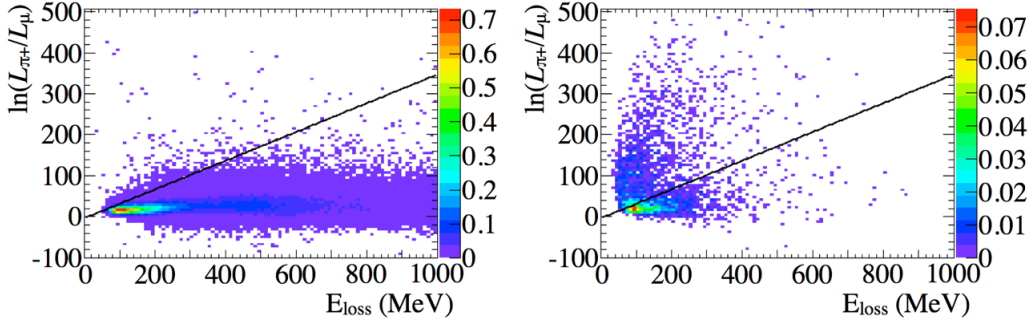


Figure 4.15: Likelihood separation of ν_μ CCQE (left) and $\text{NC}\pi^+$ (right) events, in the T2K experiment accelerator neutrino Monte Carlo simulation. The vertical axes are $\ln(L_{\pi^+}/L_\mu)$ and the horizontal axes are E_{loss} . Taken from [62].

The muon hypothesis is not considered since the single-ring π^+ hypothesis can fit muon rings with an acceptable performance.

The algorithm starts with the assumption that only one ring is in the event: the ring is tested for both the electron and π^+ hypotheses.

Then, using the result of each test as *seeds*, one more ring is assumed for both and the fit repeated: the newly assumed ring is tested for both the electron and π^+ hypotheses and the process proceeds by adding one more ring per step and per combination of hypotheses, until the number of rings reaches the maximum of six.

The fit sequence can be summarized as a tree shaped graph: Figure 4.16 shows the tree starting with the electron hypothesis, another tree is generated starting with the π^+ one.

Four parameters of ring counting constrain which added rings are acceptable or not: Ea_0 , Mua_0 , a_0 , a_1 . When an $n+1$ -th ring is added to an n -ring hypothesis, the condition on hypotheses likelihoods L_{n+1} and L_n for it to be accepted is:

- if $n = 1$:
 - $-\ln\left(\frac{L_{n+1}}{L_n}\right) > Ea_0 + a_1 * E_{\text{vis}}$, if the added ring is e-like.
 - $-\ln\left(\frac{L_{n+1}}{L_n}\right) > Mua_0 + a_1 * E_{\text{vis}}$, if the added ring is π -like.
- if $n > 1$:
 - $-\ln\left(\frac{L_{n+1}}{L_n}\right) > a_0 + a_1 * E_{\text{vis}}$

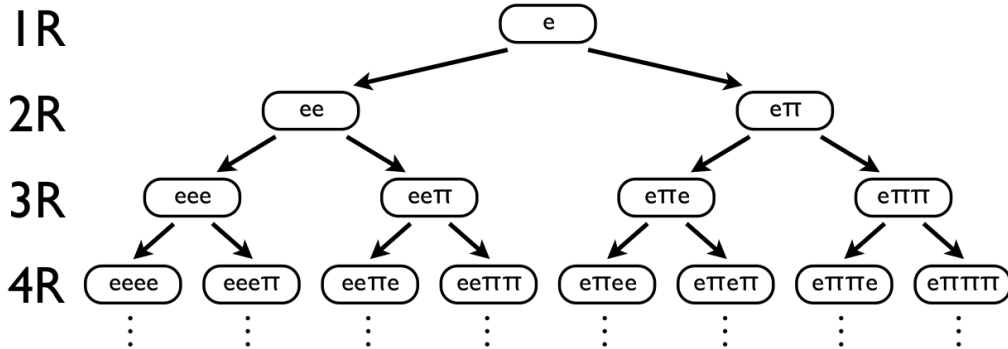


Figure 4.16: A tree diagram showing how the tree of the multi-ring hypotheses evolve as the number of rings is increased. The diagram is for the case assuming the first ring as electron and an equivalent procedure is done for the case of assuming a π^+ as the first ring. Taken from [62].

For Super-Kamiokande the following values are used:

- $Ea_0 = 87.5$
- $Mua_0 = 140$
- $a_0 = 70$
- $a_1 = 0$

When the second ring is added to the first, they share a common vertex, its initial direction is obtained by evaluating the likelihood for 400 uniformly distributed points on the unit sphere, arbitrarily assuming for it a momentum of 50 MeV/c: the direction which minimizes $-\ln L$ is chosen. Then the second ring momentum is fitted while all other parameters are fixed. After the momentum of the second ring has been estimated, a simultaneous fit of direction and momentum of the second ring is performed while all other parameters are still fixed. In the same fashion, a simultaneous fit of the two rings momenta is performed, in order to redistribute the visible energy between the two rings especially in case of overlap and, finally, the momenta, directions and the common vertex are all simultaneously fit to get the final best-fit two-ring result. If the second ring is being tested under the π^+ hypothesis, the fit of the E_{loss} parameter is included in the final step.

Once the two-ring fits are done, for each of the two particle hypotheses for the new ring, whether the fitted second ring is an actual true ring is checked

by comparing the likelihoods between the hypotheses before and after adding the new ring.

The process of adding a new ring, fitting and checking if the new ring can be considered true or fake is repeated until the new ring fails the check or a number of six rings is reached. The simultaneous fit of all parameters is done only for the two-ring case: for the subsequent cases only the simultaneous momentum fit of all rings is performed, assuming that the two-ring fit gives a reasonable estimate of the true interaction vertex. To save more computational time, for the fifth and sixth ring, only electron hypotheses are considered.

In the end, the hypothesis with the smallest $-\ln L$ among all the calculated hypotheses containing true rings in both trees is chosen as the *seeding multi-ring hypothesis*.

The rings in the seeding multi-ring hypothesis are ordered by the visible energy of the ring, i.e. the reconstructed kinetic energy above Cherenkov threshold. A ring correction algorithm is applied to remove fake rings, as shown in [56]: for the most energetic ring, the angle between the directions of the ring and each lower-energy ring is calculated and if the angle for a given lower-energy ring is smaller than 20° , the lower-energy ring is merged to the most energetic ring by adding their visible energies. After that, the most energetic ring is re-fitted assuming three particle types: electron, muon and π^+ while all the other remaining rings which were not merged in the ring-merge procedure are fixed at their original configurations. All the ring parameters are fit simultaneously including the vertex.

The best-fit likelihoods for the electron and π^+ hypotheses of the most-energetic ring are compared using the following inequality:

$$\ln(L_e/L_{\pi^+}) > -10 \quad (4.30)$$

which is the same condition as in Section 4.3.8, except for the π^+ instead of the muon hypothesis. If this condition is satisfied, the ring is of electron, or showering, type. Otherwise it's of π^+ , or non-showering, type. If the most energetic ring is found to be of non-showering type, it is assumed to have been produced by a muon. Any less energetic ring of non-showering type is assumed to have been produced by a charged pion. This consideration is backed by Monte Carlo simulations of the atmospheric neutrino CC and NC events involving muons and charged pions.

After the most energetic ring, all the other rings are re-fitted one by one, including their vertex, allowing each ring to have it in different positions. The result obtained in the end of this sequential fit procedure is taken as the best reconstruction of the processed event.

4.4 Performance comparison between *APFit* and *fiTQun*

The reconstruction performances of *APFit* and *fiTQun* have been studied and compared when applied against Monte Carlo simulations of single ring Fully Contained Charged Current events, with a single electron or a single muon in the final state.

The Fiducial Volume for *APFit* is defined as the region of the inner 2 m inside from the ID wall, while the *fiTQun* performance has been tested in two different Fiducial Volume definitions: 1.5 m and 2 m.

Figure 4.17 shows the distributions of the distance between the reconstructed and true vertexes. The vertex resolutions defined at 1σ deviation position for single electron (muon) events are; 20.1 (19.3) cm for the best single ring fit of *fiTQun* and 29.4 (22.7) cm for *APFit*. The momentum dependencies of the vertex resolution are shown in Figure 4.18.

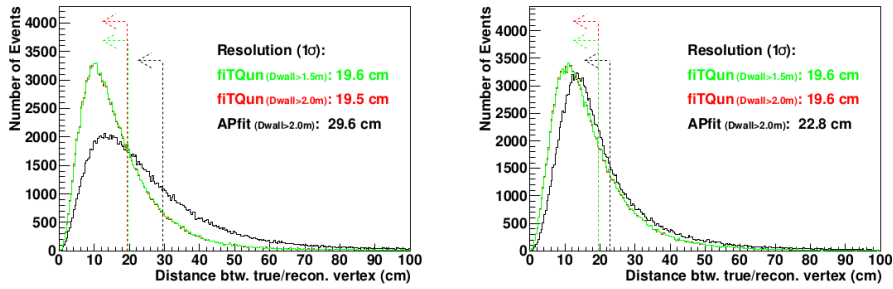


Figure 4.17: Distributions of the distance between the true and reconstructed vertex of FC true-fiducial CCQE single electron (left) and muon (right) events in the atmospheric neutrino MC. The green (red) histogram is for the best single ring fit of *fiTQun* with the distance from the ID wall $D_{\text{wall}} > 1.5$ (2.0) m cut and black histogram is for *APFit* with the $D_{\text{wall}} > 2.0$ m cut. The dotted lines show the vertex resolution which is defined at one standard deviation.

The angle between the reconstructed and true directions and their momentum dependencies are also shown in Figure 4.19 and 4.20. For single electron and muon events, the direction resolutions defined at one standard deviation angle are 2.81° (2.91°) and 1.73° (1.75°) for the best single ring fit of *fiTQun* (*APFit*).

In order to evaluate the momentum resolution, the fractional difference between the reconstructed and true momenta is fitted by a Gaussian at each

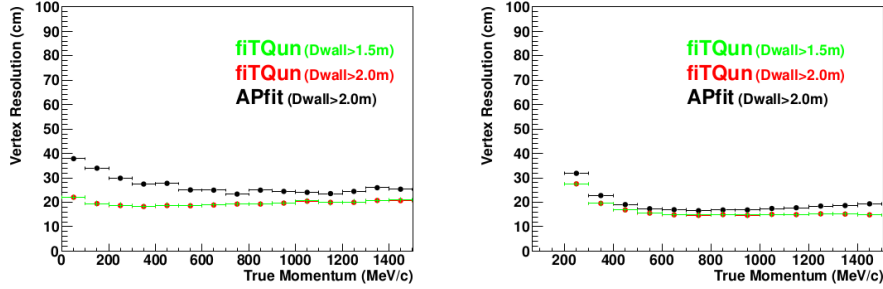


Figure 4.18: Vertex resolution as a function of true momentum of FC true-fiducial CCQE single electron (left) and muon (right) events in the atmospheric neutrino MC. The green (red) points are for the best single ring fit of *fitQun* with the distance from the ID wall $D_{\text{wall}} > 1.5$ (2.0) m cut and black points are for *APFit* with the $D_{\text{wall}} > 2.0$ m cut.

true momentum bin and taking the sigma of the fitted Gaussian as the resolution. Figure 4.21 shows the momentum resolution as a function of the true momentum.

Finally, the misidentification rates as a function of the true momentum are shown in Figure 4.22.

In the end, this study allows to confirm that *fitQun* overall reconstruction performances are better than those of *APFit*.

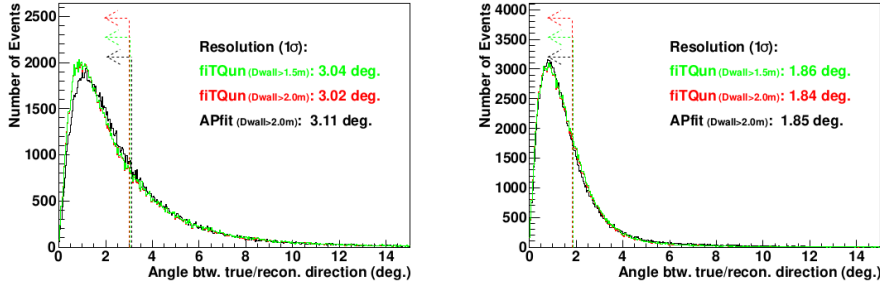


Figure 4.19: Distributions of the angle between the true and reconstructed direction of FC true-fiducial CCQE single electron (left) and muon (right) events in the atmospheric neutrino MC. The green (red) histogram is for the best single ring fit of *fitQun* with the distance from the ID wall $D_{\text{wall}} > 1.5$ (2.0) m cut and black histogram is for *APFit* with the $D_{\text{wall}} > 2.0$ m cut. The dotted lines show the direction resolution which is defined as 1σ deviation point.

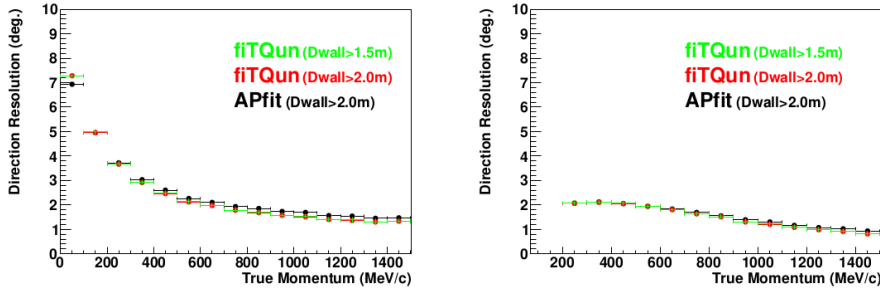


Figure 4.20: Direction resolution as a function of true momentum of FC true-fiducial CCQE single electron (left) and muon (right) events in the atmospheric neutrino MC. The green (red) points are for the best single ring fit of *fiTQun* with the distance from the ID wall $D_{\text{wall}} > 1.5$ (2.0) m cut and black points are for *APFit* with the $D_{\text{wall}} > 2.0$ m cut.

4.5 Neutron tagging

Counting neutrons produced in a FC event can help to separate signal from background events. For example an anti-neutrino interaction such as:

$$\bar{\nu}_e + p \rightarrow n + e^+ \quad (4.31)$$

produces a neutron that after thermalisation in water is captured by an Hydrogen atom:

$$n + p \rightarrow d^* \rightarrow d + \gamma \quad (4.32)$$

The delayed detection ($\sim 200 \mu\text{s}$) of the electron Compton-scattered by the 2.2 MeV γ in coincidence with the detection of the positron from the primary event is a signature of the process.

4.5.1 Neutron tagging algorithm

Tagging and counting neutrons in FC events is challenging due to the low energy of the de-excitation photon produced in their capture: this task is performed using a specifically developed algorithm [37] which is made of two steps:

1. initial neutron candidate selection;
2. final neutron candidate selection with neural network.

One neutron capture is expected to produce less than 10 PMT hits in the ID: first such PMT hit clusters are searched for as initial candidates, then each candidate is fed to a dedicated neural network.

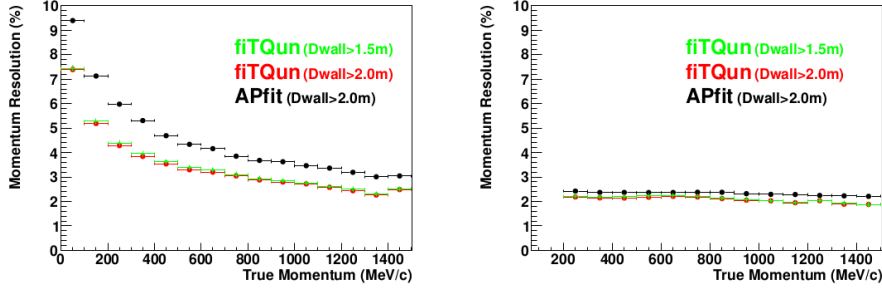


Figure 4.21: Momentum resolution as a function of true momentum of FC true-fiducial CCQE single electron (left) and muon (right) events in the atmospheric neutrino MC. The green (red) points are for the best single ring fit of *fitQun* with the distance from the ID wall $D_{\text{wall}} > 1.5$ (2.0) m cut and black points are for *APFit* with the $D_{\text{wall}} > 2.0$ m cut.

Initial neutron candidate selection

The number of hit PMTs in a sliding 10 ns time window (N_{10}^{RAW}) is counted. Each PMT hit timing is corrected for time-of-flight using the primary FC event vertex position. A cluster with $N_{10}^{\text{RAW}} > 4$ is tagged as neutron candidate but if $N_{10}^{\text{RAW}} > 50$ or the number of hit PMTs in a 200 ns time window around the cluster timing (N_{200}) is more than 200 it is rejected as background.

Besides random dark noise, another type of time-clustered dark noise has to be taken into account: its source has been identified to be the scintillation light in the SK PMT glass. Since this clustered noise can mimic a neutron capture signal, a cut is introduced to reject it. If there are multiple hits in the same PMT within X μs these hits are removed. The value of X depends on the value of N_{10}^{RAW} : for values of less than 7, X is set to 12 μs otherwise it is set to 6 μs . Clusters with a remaining number of PMT hits (N_{10}) greater than 4 are selected as initial neutron candidates.

Final neutron candidate selection with neural network

The vertex position of the Compton-scattered electron of initial neutron candidates is reconstructed using the Neut-Fit algorithm. Neut-Fit searches for the vertex position that minimizes the RMS of the time-of-flight subtracted residual timing distribution of the initial candidate hit cluster, defined as:

$$t'_{rms} = \sqrt{\frac{\sum_i^{N_{10n}} (t'_i - t'_{mean})^2}{N_{10n}}} \quad (4.33)$$

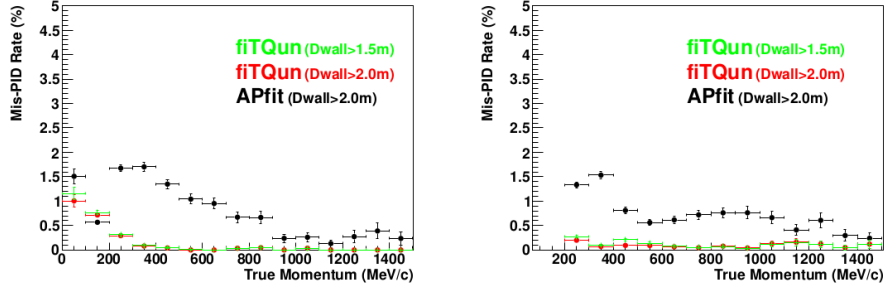


Figure 4.22: Rate of erroneous particle identification (*Mis-PID*) as a function of true momentum of FC true-fiducial CCQE single electron (left) and muon (right) events in the atmospheric neutrino MC. The green (red) points are for the best single ring fit of *fiTQun* with the distance from the ID wall $D_{\text{wall}} > 1.5$ (2.0) m cut and black points are for *APFit* with the $D_{\text{wall}} > 2.0$ m cut.

$$t'_{\text{mean}} = \sum_i^{N_{10n}} \frac{t'_i}{N_{10n}} \quad (4.34)$$

where t'_i is the i -th PMT's time-of-flight corrected residual time for an assumed vertex position and N_{10n} is the number of PMT hits in a 10 ns timing window in residual timing for an assumed vertex position. Neut-Fit is executed twice: in the first run the reconstructed vertex position is constrained within 200 cm from the primary vertex position, in the second run it is unconstrained. Finally the candidate is fed to a neural network that performs the final classification as signal or background by evaluating 23 calculated input variables, as described in detail in [60].

Chapter 5

Search for $p \rightarrow \nu K^+$ in SK-IV using *fiTQun*

We searched for proton decay in the $p \rightarrow \nu K^+$, $K^+ \rightarrow \pi^+ \pi^0$ channel in the full SK-IV FCFV data, with a livetime of 3244.4 days corresponding to an exposure of 200.0 kton*year. This chapter describes the simulated samples used, the signal definition and the selection criteria, the study of remaining background, the estimation of systematic uncertainties and the search for candidates in real data. The reference study for this analysis is [40].

5.1 Simulated samples used

We used three simulated samples in this analysis, all reconstructed with *fiTQun*:

- **PDK MC:** proton decay $p \rightarrow \nu K^+$ Monte Carlo simulated FCFV sample containing ~ 600000 events;
- **ATM- ν MC:** 500 years of atmospheric neutrino Monte Carlo simulated background FCFV sample, each event is weighted for oscillation probability and neutrino flux;
- **Hybrid sample:** we built an hybrid sample to estimate detector systematic error, as described in Section (5.6.4).

5.2 Proton decay mode

We consider the proton decay mode:

$$p \rightarrow \nu K^+ \tag{5.1}$$

The two most probable decay modes of charged kaons are:

$$\begin{aligned} K^+ &\rightarrow \mu^+ \nu_\mu \quad (64\%) \\ K^+ &\rightarrow \pi^+ \pi^0 \quad (21\%) \end{aligned} \quad (5.2)$$

of which the second one is relevant for this analysis. If we consider that

$$\pi^0 \rightarrow \gamma\gamma \quad (98.8\%) \quad (5.3)$$

the particles in the final state considered for this study are

$$\pi^+ \gamma\gamma \quad (5.4)$$

5.2.1 Decay kinematics

Proton decay is assumed to happen in water molecules (H_2O) with equal probability for each of its ten protons: in the case of a decay in Hydrogen the proton is at rest since it's free while in the case of a decay in Oxygen it's in motion due to Fermi momentum since it's bound. In the free proton case the neutrino and charged kaon are emitted back-to-back with a 339 MeV/c momentum each. In the bound proton case several effects are taken into account: proton binding energy with nucleus, correlated decay with other nucleons, proton Fermi momentum, interaction of the decay products with nuclear matter. These effects are all simulated in the Monte-Carlo samples used.

Products from proton decays in Oxygen have an invariant mass lower than the mass of a free proton, due to the effect of binding energy and correlation between nucleons: for this reason, bound proton decays are simulated with a lower proton invariant mass and a 10% correlated decay probability [58]. The position of the decay proton is simulated according to the Woods-Saxon nuclear density model. Figure 5.1 shows the results of simulation with NEUT [36].

Since the fraction of charged kaons produced above Cherenkov threshold (560 MeV/c in water) is negligibly small, we can assume that the charged kaon from proton decay produces no visible ring.

The fraction of charged kaons decaying at rest in water is 89%, as simulated by SKDETSIM: in this case the decay is back-to-back and each produced π^+ and π^0 carry a momentum of 205 MeV/c.

The π^+ is above Cherenkov threshold (156 MeV/c in water), the expected Cherenkov angle is $\sim 25^\circ$, narrower than the maximum angle of 42° .

The π^0 is a neutral particle and doesn't produce any ring but it decays 99.8% [17] of the times in two photons which convert to positron-electron couples in water and produce two visible rings.

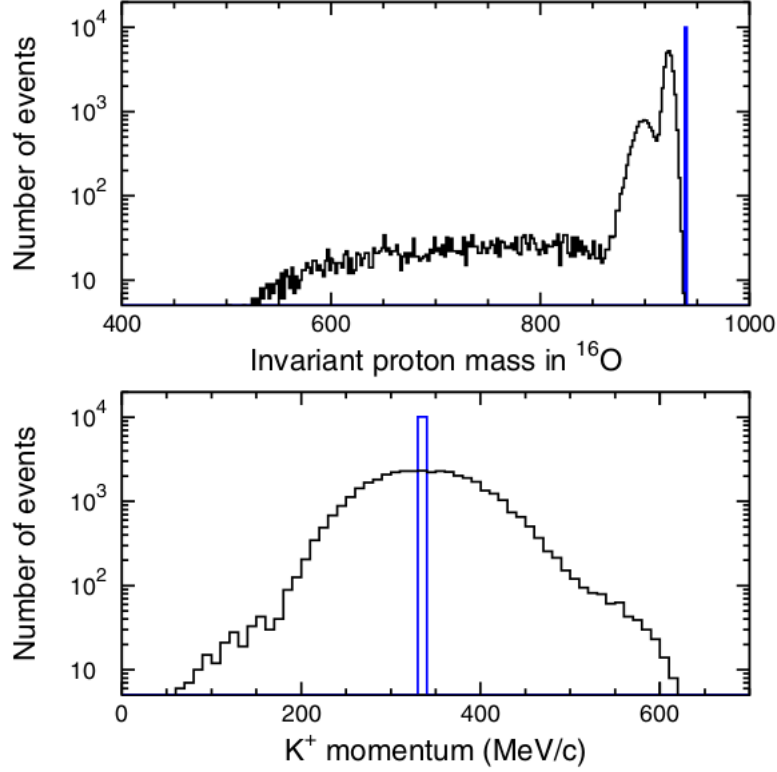


Figure 5.1: The top figure shows the decaying proton invariant mass distribution in ^{16}O and the lower figure shows the K^+ momentum distribution from the simulation of $p \rightarrow \nu K^+$. In the top figure, the single-bin histogram shows the free proton case and the broad histogram shows the bound proton case. The rightmost peak in the bound proton case corresponds to the p-state, located slightly lower than the proton mass by 15.5 MeV of binding energy; the second rightmost peak is the s-state (39 MeV in binding energy). The correlated nucleon decay makes the longer tail in the lower mass region. In the bottom figure, the single-bin histogram shows the free proton case (339 MeV/c) and the broad histogram shows the bound proton case which is smeared by Fermi motion.

5.2.2 Definition of visible energy

The *visible energy* E_{vis} of a particle is defined as the difference between its energy E and its Cherenkov threshold on energy E_{th} .

$$E_{vis} = E - E_{th} = \sqrt{p^2 c^2 + m_0^2 c^4} - \sqrt{p_{th}^2 c^2 + m_0^2 c^4} \quad (5.5)$$

where p , p_{th} and m_0 are the momentum, the Cherenkov momentum threshold and the rest mass of the particle respectively.

Intuitively, the visible energy measures the maximum amount of energy that the particle could convert entirely into Cherenkov radiation.

A direct calculation shows that the visible energy for the charged pion, if the parent kaon decays at rest, is ~ 39 MeV, which is one order of magnitude lower than the typical visible energy of the photons coming from the neutral pion decay: this means that the charged pion ring is expected to be the fainter ring in the signal events and its reconstruction is a challenging task.

Finally, this definition is equivalent to the one used in 3.1.7 for the FC reduction process and it can be calculated using *fiTQun* reconstructed variables only.

5.3 Event selections

Signal events $p \rightarrow \nu K^+$, $K^+ \rightarrow \pi^+ \pi^0$ with $\pi^0 \rightarrow \gamma\gamma$ are selected in **FCFV** (Section 3.1.7) samples by the following criteria:

1. **nring**: 3 reconstructed rings,
2. **PID**: 2 e-like and 1 μ or π -like rings,
3. **micel**: 0 or 1 *Michel electrons*,
4. **M $_{\pi^0}$** : reconstructed π^0 mass between 85 and 185 MeV/ c^2 ,
5. **P $_{\pi^0}$** : reconstructed π^0 momentum between 175 and 250 MeV/ c ,
6. **P $_{\pi^+}$** : reconstructed π^+ momentum between 175 and 250 MeV/ c ,
7. **M $_{K^+}$** : reconstructed K^+ mass between 450 and 530 MeV/ c^2 ,
8. **P $_{K^+}$** : reconstructed K^+ momentum less than 60 MeV/ c ,
9. **Ntag**: 0 tagged neutrons.

The background for this analysis are the FCFV events from atmospheric neutrino interactions: we estimate the remaining background by applying the same event selections as for signal to the ATM- ν MC sample.

5.4 Distributions along cut parameters

We compare distributions along cut parameters for PDK MC and ATM- ν MC overlaid one by one. We also show the same distributions for data and ATM- ν MC scaled by data livetime and overlaid.

5.4.1 Number of reconstructed rings distributions

Signal events contain three reconstructed rings. Figure 5.2(a) shows the PDK MC and ATM- ν MC distributions of the number of reconstructed rings. Only about 20% of true $\pi^+\pi^0$ with $\pi^0 \rightarrow \gamma\gamma$ events in PDK MC has three reconstructed rings as expected because the π^+ ring is a faint object and hard to reconstruct. Nevertheless three rings are required in order to reconstruct the kaon kinematics. Figure 5.2(b) shows the data and ATM- ν MC distributions.

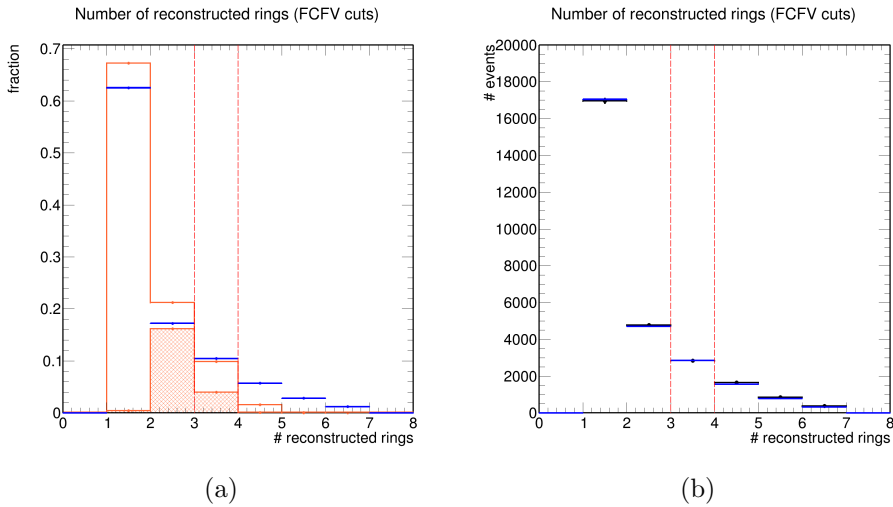


Figure 5.2: Number of reconstructed rings distributions for FCFV samples. The left plot shows the PDK MC (orange) and the ATM- ν MC (blue) distributions normalized to unity. The shaded area shows true signal events ($K^+ \rightarrow \pi^+\pi^0, \pi^0 \rightarrow \gamma\gamma$) in PDK MC. The right plot shows Data (black dots) and ATM- ν MC (blue), scaled to Data livetime, distributions. Events with 3 reconstructed rings pass the **nring** cut.

5.4.2 Number of reconstructed e-like rings distributions

Signal is made of two e-like rings from the π^0 decay plus a third ring that we require to be non-showering since it's supposed to be produced by the π^+ : anyway we don't constrain it to be a π -like ring to improve selection efficiency (Section 4.3.8). Figure 5.3(a) shows the PDK MC and ATM- ν MC distributions of the number of reconstructed e-like rings, Figure 5.3(b) shows the same distributions for Data and ATM- ν MC.

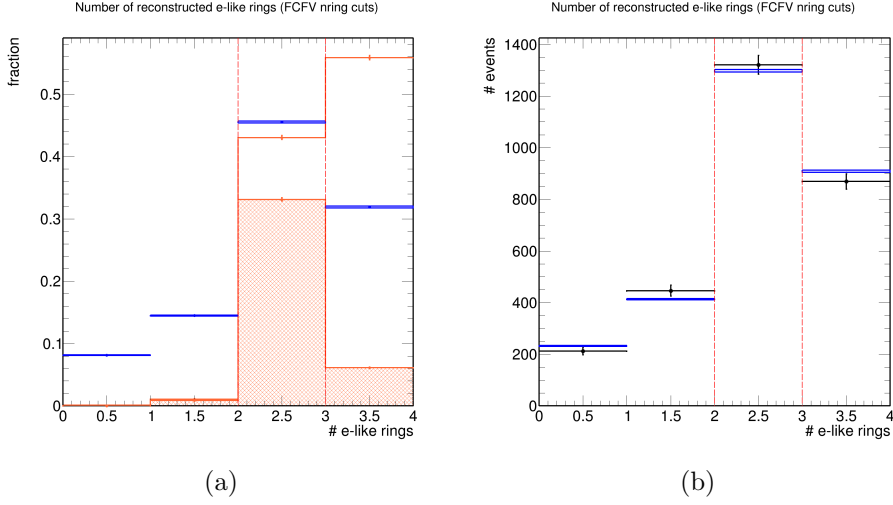


Figure 5.3: Number of reconstructed e-like rings distributions for FCFV samples, with **nring** cut applied. The left plot shows the PDK MC (orange) the ATM MC (blue) distributions normalized to unity. The shaded area shows true signal events ($K^+ \rightarrow \pi^+ \pi^0$, $\pi^0 \rightarrow \gamma\gamma$). The right plot shows data (black dots) and ATM- ν MC (blue), scaled to data livetime, distributions. Events with 2 reconstructed e-like rings pass the **PID** cut.

5.4.3 Tagged *Michel electrons* distributions

Signal contains one π^+ whose final decay products include one *Michel positron*: events with more than one tagged *Michel electron* are rejected. Figure 5.4(a) shows the distributions of the number of tagged *Michel electrons* for PDK MC and ATM- ν MC, Figure 5.4(b) shows the same distributions for data and ATM- ν MC.

5.4.4 Reconstructed π^0 mass and momentum distributions

Reconstructed π^0 mass (M_{π^0}) and momentum (P_{π^0}) are calculated as:

$$M_{\pi^0} = \sqrt{2|\vec{p}_{\gamma_1}||\vec{p}_{\gamma_2}|(1 - \cos\theta)} \quad (5.6)$$

$$P_{\pi^0} = |\vec{p}_{\gamma_1} + \vec{p}_{\gamma_2}| \quad (5.7)$$

where \vec{p}_{γ_1} and \vec{p}_{γ_2} are the e-like rings reconstructed momenta and θ is the angle between their reconstructed directions.

Figure 5.5(a) shows the distributions of M_{π^0} for PDK MC and ATM- ν MC, Figure 5.5(b) shows the same distributions for Data and ATM- ν MC.

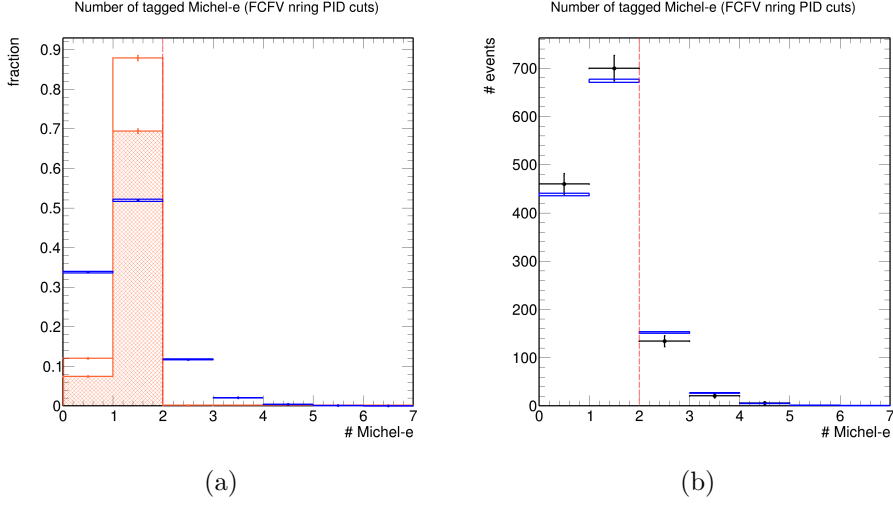


Figure 5.4: Number of tagged *Michel electrons* distributions for FCFV samples, with **nring** and **PID** cuts applied. The left plot shows the PDK MC (orange) the ATM MC (blue) distributions normalized to unity. The shaded area shows true signal events ($K^+ \rightarrow \pi^+\pi^0$, $\pi^0 \rightarrow \gamma\gamma$). The right plot shows data (black dots) and ATM- ν MC (blue), scaled to data livetime, distributions. Events with 0 or 1 tagged *Michel electrons* pass the **Michel** cut.

Figure 5.6(a) shows the distributions of P_{π^0} for PDK MC and ATM- ν MC, Figure 5.6(b) shows the same distributions for Data and ATM- ν MC.

5.4.5 Reconstructed π^+ momentum distributions

The reconstructed π^+ momentum P_{π^+} is equal to the reconstructed momentum of the non-showering ring in the event in case it is tagged as π -like. In case it is tagged as μ -like, it is assumed to be a misidentified charged pion and P_{π^+} is calculated as:

$$P_{\pi^+} = \frac{m_{\pi^+}}{m_{\mu}} * P_{\mu} \quad (5.8)$$

where m_{π^+} and m_{μ} are the π^+ and μ masses from the PDG [17] respectively and P_{μ} is the reconstructed momentum of the μ -like ring.

Figure 5.7(a) shows the distributions of P_{π^+} for PDK MC and ATM- ν MC, Figure 5.7(b) shows the same distributions for Data and ATM- ν MC.

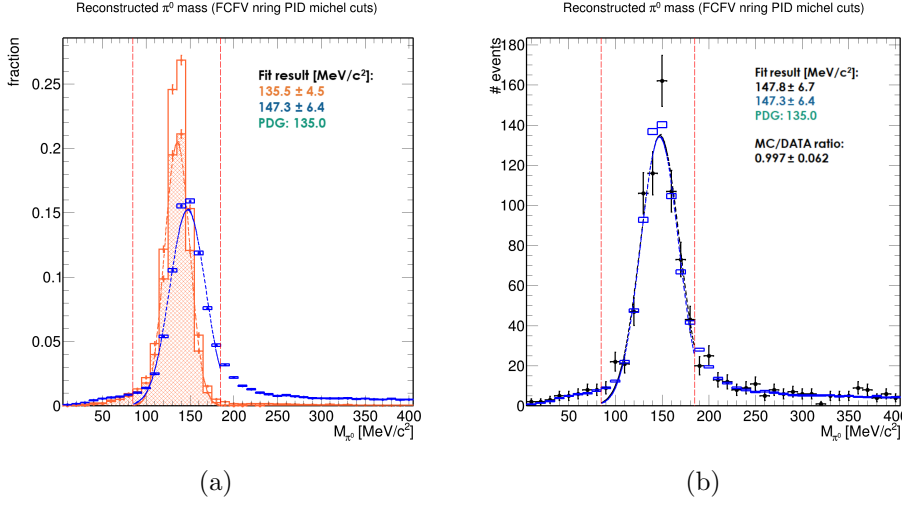


Figure 5.5: Reconstructed π^0 mass distributions M_{π^0} for FCFV samples, with **nring**, **PID** and **michel** cuts applied. The left plot shows the PDK MC (orange) the ATM MC (blue) distributions normalized to unity. The shaded area shows true signal events ($K^+ \rightarrow \pi^+\pi^0$, $\pi^0 \rightarrow \gamma\gamma$). The right plot shows data (black dots) and ATM- ν MC (blue), scaled to data livetime, distributions. The fitted peak values agree with the π^0 mass value from the PDG [17]. Events with reconstructed π^0 mass between 85 and 185 MeV/c² pass the M_{π^0} cut.

5.4.6 Reconstructed K^+ mass and momentum distributions

Reconstructed K^+ mass (M_{K^+}) and momentum (P_{K^+}) are calculated as:

$$P_{K^+} = |\vec{p}_{\pi^+} + \vec{p}_{\pi^0}| \quad (5.9)$$

$$M_{K^+} = \sqrt{E_{K^+}^2 - P_{K^+}^2} = \sqrt{(E_{\pi^+} + E_{\pi^0})^2 - P_{K^+}^2} \quad (5.10)$$

Figure 5.8(a) shows the distributions of M_{K^+} for PDK MC and ATM- ν MC, Figure 5.8(b) shows the same distributions for Data and ATM- ν MC.

Figure 5.9(a) shows the distributions of P_{K^+} for PDK MC and ATM- ν MC, Figure 5.9(b) shows the same distributions for Data and ATM- ν MC.

5.4.7 Number of tagged neutrons

Figure 5.10 shows the distributions of the number of tagged neutrons per event. No neutrons are expected to be tagged according to our signal defi-

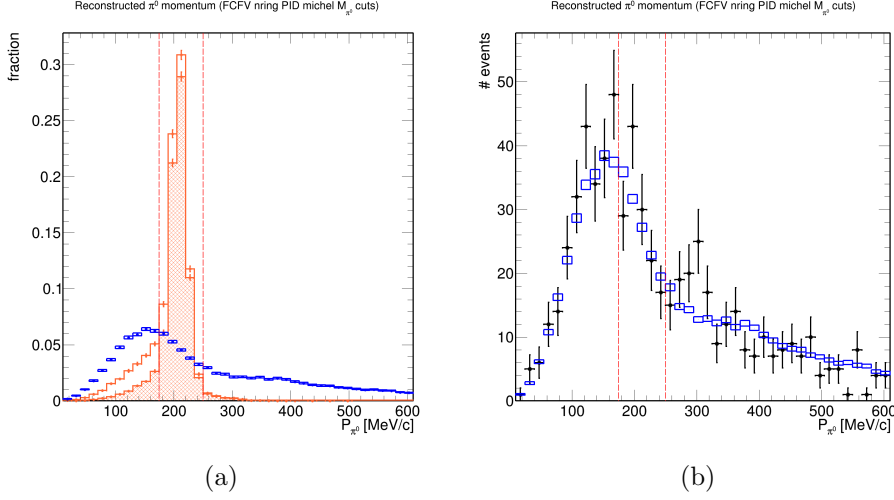


Figure 5.6: Reconstructed π^0 momentum distributions P_{π^0} for FCFV samples, with **nring**, **PID**, **michel** and M_{π^0} cuts applied. The left plot shows the PDK MC (orange) the ATM MC (blue) distributions normalized to unity. The shaded area shows true signal events ($K^+ \rightarrow \pi^+\pi^0$, $\pi^0 \rightarrow \gamma\gamma$). The peak at 205 MeV/c is consistent with the expected value. The right plot shows data (black dots) and ATM- ν MC (blue), scaled to data livetime, distributions. Events with reconstructed π^0 momentum between 175 and 250 MeV/c pass the \mathbf{P}_{π^0} cut.

nition. No data events reach this selection stage so no distribution is shown for the data sample.

5.5 Results

Selection efficiency for PDK MC η is defined as:

$$\eta = \frac{\# \text{ events passing the cuts}}{\# \text{ of events generated in true FV}} \quad (5.11)$$

Figure 5.11(a) shows selection efficiency after each cut. The **nring** cut reduces selection efficiency to about 10% and **PID** cut further reduces it to about 4%: these cuts are necessary to reconstruct the kaon kinematics. The \mathbf{P}_{π^+} and \mathbf{P}_{K^+} cuts produce the dominant background reductions, as shown in Figure 5.11(b). No data candidates remain after all cuts. Results are summarized in Table 5.1.

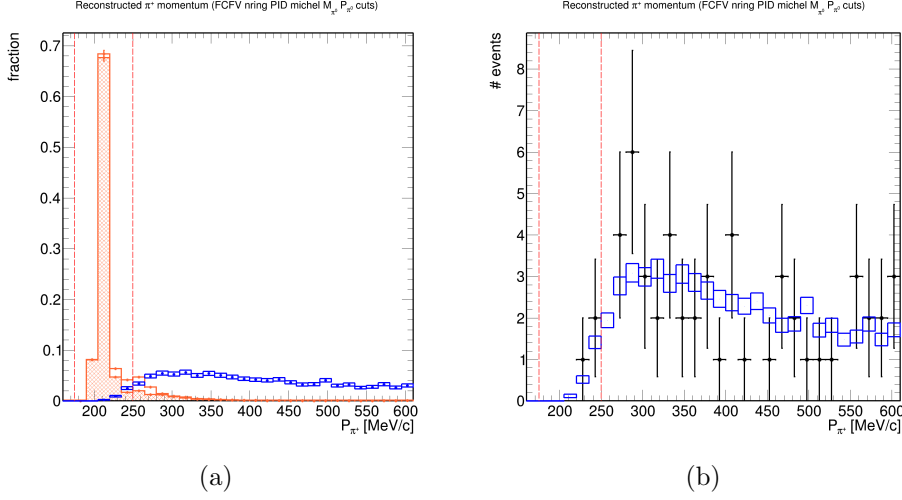


Figure 5.7: Reconstructed π^+ momentum distributions P_{π^+} for FCFV samples, with **nring**, **PID**, **michel**, M_{π^0} and P_{π^0} cuts applied. The left plot shows the PDK MC (orange) the ATM MC (blue) distributions normalized to unity. The shaded area shows true signal events ($K^+ \rightarrow \pi^+\pi^0$, $\pi^0 \rightarrow \gamma\gamma$). The peak at 205 MeV/c is consistent with the expected value. The right plot shows data (black dots) and ATM- ν MC (blue), scaled to data livetime, distributions. Events with reconstructed π^+ momentum between 175 and 250 MeV/c pass the P_{π^+} cut.

Table 5.1: Signal efficiency, remaining background and remaining data events after each cut.

Cuts	Signal efficiency (%)	# Background events (3244.4 days)	# Data events
FCFV	96.02 ± 0.03	27796.70 ± 10.80	27485 ± 88
+nring	9.50 ± 0.04	2851.15 ± 6.32	2848 ± 51
+PID	4.09 ± 0.03	1297.79 ± 4.22	1321 ± 36
+michel	4.08 ± 0.03	1111.78 ± 3.93	1160 ± 34
+ M_{π^0}	3.87 ± 0.03	673.49 ± 3.01	706 ± 26
+ P_{π^0}	2.99 ± 0.02	137.08 ± 1.36	141 ± 12
+ P_{π^+}	2.60 ± 0.02	2.05 ± 0.17	3 ± 2
+ M_{K^+}	2.53 ± 0.02	1.17 ± 0.13	2 ± 1
+ P_{K^+}	2.34 ± 0.02	0.04 ± 0.02	0
+Ntag	2.34 ± 0.02	0.03 ± 0.02	0

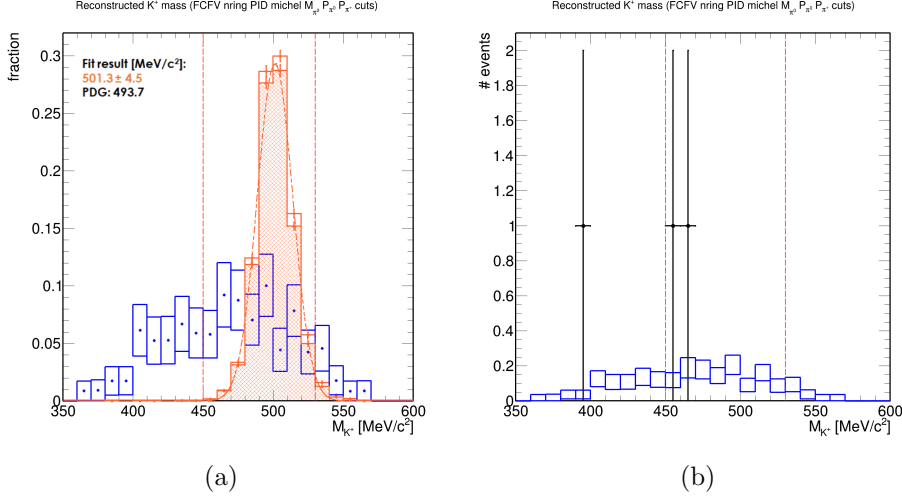


Figure 5.8: Reconstructed K^+ mass distributions M_{K^+} for FCFV samples, with **nring**, **PID**, **micel**, **M_{π^0}** , **P_{π^0}** and **P_{π^+}** cuts applied. The left plot shows the PDK MC (orange) the ATM MC (blue) distributions normalized to unity. The shaded area shows true signal events ($K^+ \rightarrow \pi^+\pi^0$, $\pi^0 \rightarrow \gamma\gamma$). The fitted peak value agrees with the K^+ mass value from the PDG [17]. The right plot shows data (black dots) and ATM- ν MC (blue), scaled to data livetime, distributions. Events with reconstructed K^+ mass between 450 and 530 MeV/c² pass the M_{K^+} cut.

5.5.1 Remaining background events

Table 5.2 summarizes the remaining background interaction modes.

Table 5.2: Remaining background breakdown by interaction mode.

Interaction mode	# Remaining background events (500 years)
$\nu_\mu CC1\pi^0$ from Δ resonance	2 (100%)

The two events in the remaining background are both $\nu_\mu CC1\pi^0$ from Δ resonance:

$$\begin{aligned}
 \nu_\mu + n &\rightarrow \Delta^+ + \mu^- \\
 \Delta^+ &\rightarrow p + \pi^0 \\
 \pi^0 &\rightarrow \gamma\gamma
 \end{aligned} \tag{5.12}$$

Figure 5.12 shows the event displays of the remaining background events: in both cases the γ rings from π^0 decay are well reconstructed and correctly

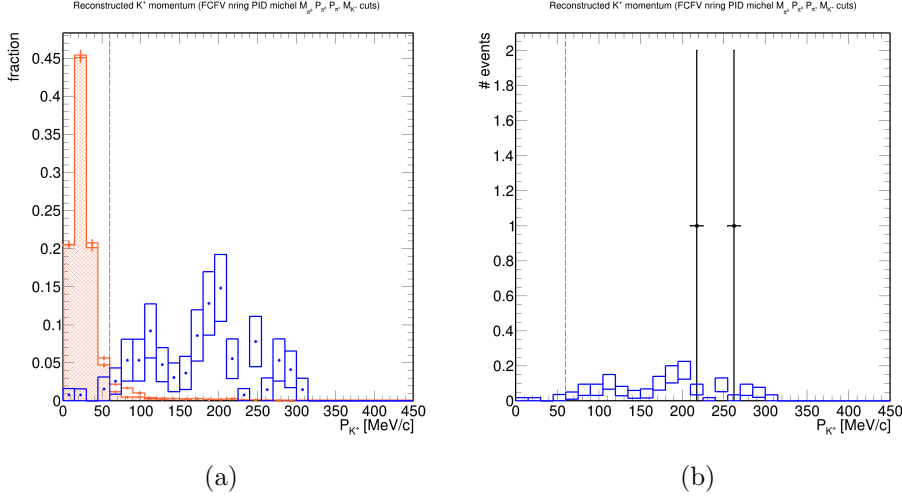


Figure 5.9: Reconstructed K^+ momentum distributions P_{K^+} for FCFV samples, with **nring**, **PID**, **michel**, M_{π^0} , P_{π^0} , P_{π^+} and M_{K^+} cuts applied. The left plot shows the PDK MC (orange) the ATM MC (blue) distributions normalized to unity. The shaded area shows true signal events ($K^+ \rightarrow \pi^+\pi^0$, $\pi^0 \rightarrow \gamma\gamma$). The peak is compatible with the expected momentum of 0 MeV/c, considering reconstruction resolution. The right plot shows data (black dots) and ATM- ν MC (blue), scaled to data livetime, distributions. Events with reconstructed K^+ momentum below 60 MeV/c pass the \mathbf{P}_{K^+} cut.

identified as e-like rings, the μ rings are well reconstructed but misidentified as π -like rings by *fiTQun*. These two events pass all the cuts by chance.

No events with true single K^+ decays remain in the background, as we could naively expect, because the selection cuts are designed to select $K^+ \rightarrow \pi^+\pi^0$ decaying alone, with no other visible particles, while if we consider K^+ producing atmospheric neutrino interactions:

$$\begin{aligned} \nu p &\rightarrow \nu \Lambda K^+ \\ \bar{\nu} p &\rightarrow \bar{\nu} \Lambda K^+ \end{aligned} \quad (5.13)$$

or K^0 producing atmospheric neutrino interactions which can produce a K^+ after K^0 charge exchange:

$$\begin{aligned} \nu n &\rightarrow \nu \Lambda K^0 \\ \bar{\nu} n &\rightarrow \bar{\nu} \Lambda K^0 \end{aligned} \quad (5.14)$$

there is always a Λ produced in association with the kaon. The Λ particle is neutral, so it can't produce any Cherenkov light but its decay modes are [17]:

$$\begin{aligned} \Lambda &\rightarrow n\pi^0 \quad (35.8\%) \\ \Lambda &\rightarrow p\pi^- \quad (63.9\%) \end{aligned} \quad (5.15)$$

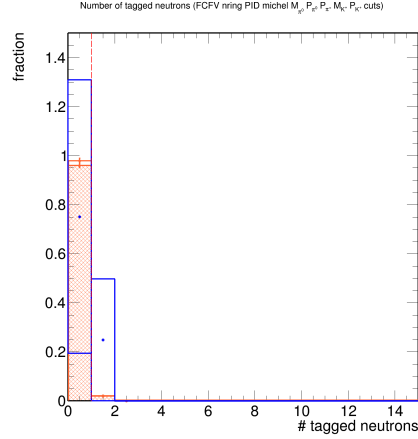


Figure 5.10: Number of tagged neutrons distributions for the PDK MC (orange) and for the ATM MC (blue) FCFV samples with **nring**, **PID**, **Michel**, \mathbf{M}_{π^0} , \mathbf{P}_{π^0} , \mathbf{P}_{π^+} , \mathbf{M}_{K^+} and \mathbf{P}_{K^+} cuts applied, normalized to unity. The shaded area shows true signal events ($K^+ \rightarrow \pi^+\pi^0$, $\pi^0 \rightarrow \gamma\gamma$). Events with 0 tagged neutrons pass the **ntag** cut.

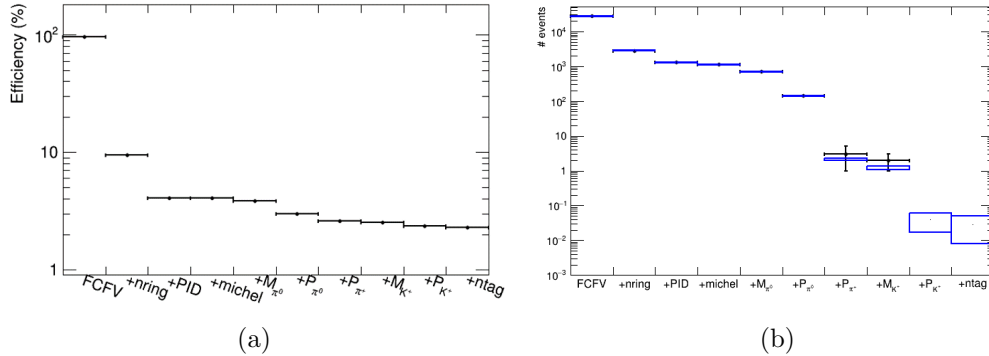
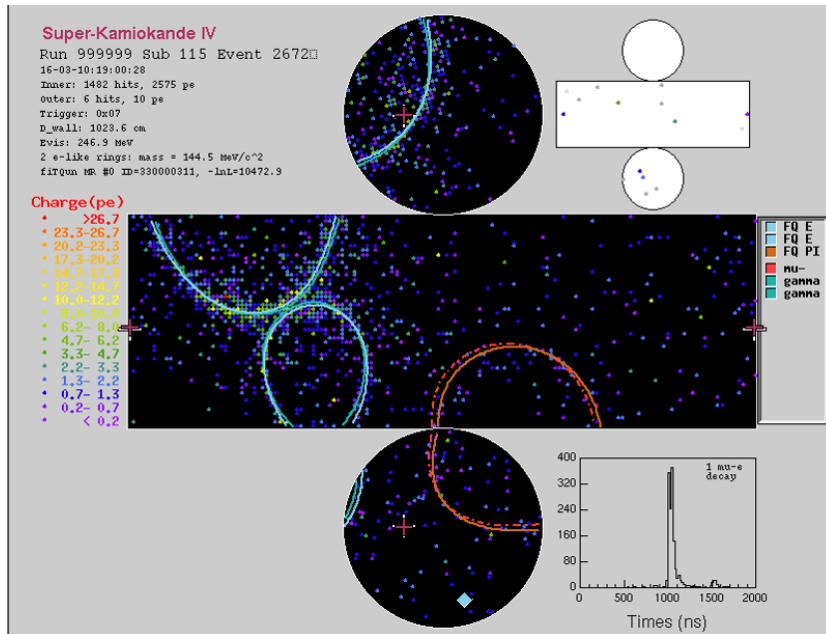
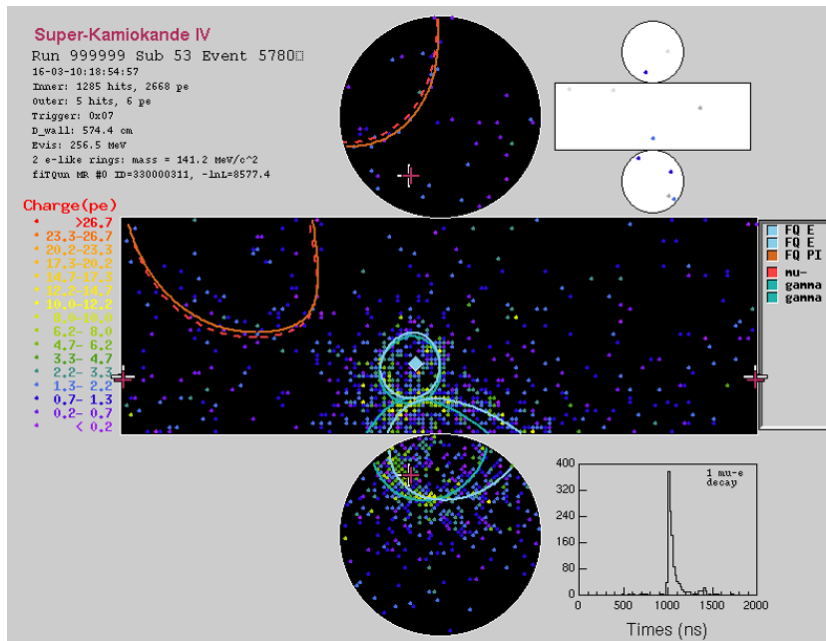


Figure 5.11: The left plot shows selection efficiency after each cut. The right plot shows remaining data events (black) and remaining background from ATM- ν MC (blue) scaled to data livetime after each cut.

and they add visible particles in the final state. Table 5.5.1 summarizes the number of remaining background events, scaled to data livetime, with a true single K^+ decay after each cut: the number of such events entering the analysis is low (6.0) and the dominant reduction happens after **nring** and **PID** cuts, as expected.



(a)



(b)

Figure 5.12: Event display of the two remaining background events after all cuts.

Table 5.3: Remaining background events, scaled to data livetime, with a true single K^+ decay

Cuts	# Background events (3244.4 days) with true single K^+ decay
FCFV	6.00 ± 0.20
+nring	1.30 ± 0.10
+PID	0.43 ± 0.09
+michel	0.34 ± 0.08
$+M_{\pi^0}$	0.25 ± 0.07
$+P_{\pi^0}$	0.13 ± 0.05
$+P_{\pi^+}$	0
$+M_{K^+}$	0
$+P_{K^+}$	0
+Ntag	0

5.5.2 Sideband check

We checked agreement between data and ATM- ν MC outside the signal box i.e. in the *sidebands*. We defined the following cuts to exclude the presence of any possible signal candidate from the selection, aiming at having enough remaining events to evaluate the agreement:

1. **nring**: 3 reconstructed rings,
2. **PID**: 2 e-like and 1 μ or π -like rings,
3. **michel**: 0 or 1 *Michel electrons*,
4. M_{π^0} : reconstructed π^0 mass between 85 and 185 MeV/ c^2 ,
5. P_{π^0} : reconstructed π^0 momentum greater than 330 MeV/ c .

Figure 5.13 shows the reconstructed Kaon mass and momentum distributions for events in the *sidebands*: data and ATM- ν MC scaled to data livetime distributions agree well.

5.6 Estimation of systematic error

We evaluated systematic error coming from physics model and detector uncertainties for both signal efficiency and remaining background.

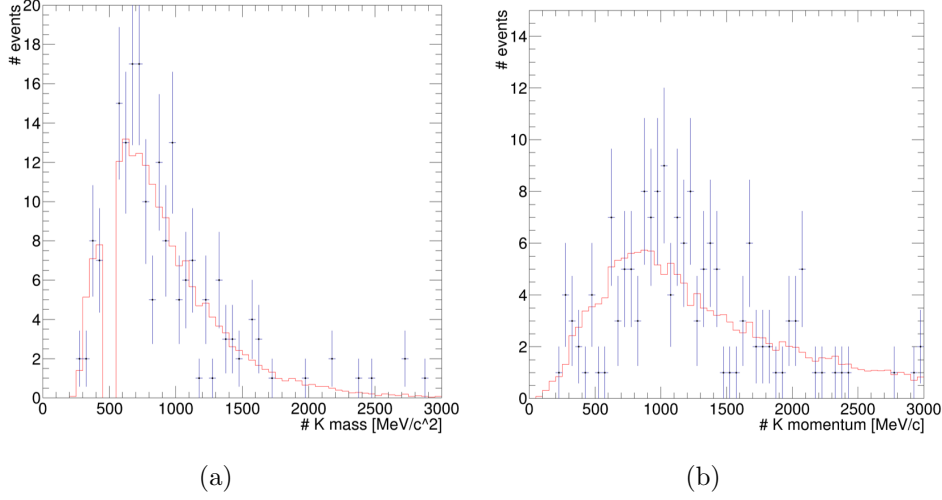


Figure 5.13: Distributions of reconstructed Kaon mass (left) and momentum (right) with *sideband* cuts defined in Section 5.5.2 for data (blue dots) and ATM- ν MC (red histogram) scaled to data livetime.

5.6.1 Physics model uncertainties for signal efficiency

We identified these physics model uncertainties for signal efficiency:

- correlated nucleon decay,
- fermi momentum of nucleon,
- K^+ Final State Interactions (FSI),
- K^+ Secondary Interactions (SI),
- Pion SI.

Correlated nucleon decay

Proton decays in Oxygen are expected to happen under the effect of other nucleons in 10% of the cases, as explained in Section 5.2.1. A conservative 100% uncertainty is assigned to the correlated nucleon decay probability. The related systematic error on signal efficiency is obtained by weighting PDK MC events: correlated and normal proton decays from Oxygen are weighted by $w_{O_{corr}}$ and $w_{O_{norm}}$ respectively:

$$\begin{aligned}
 w_{O_{corr}} &= 1 + \alpha \\
 w_{O_{norm}} &= \frac{N_{O_{norm}} - \alpha N_{O_{corr}}}{N_{O_{norm}}}
 \end{aligned} \tag{5.16}$$

where α is the uncertainty magnitude and $N_{O_{corr}}$ and $N_{O_{norm}}$ are the number of correlated and normal decay in Oxygen events in the true FV respectively. Proton decays from Hydrogen remain unweighted or, equivalently, their weight is 1. Two weighted samples, one with $\alpha = +1$ and one with $\alpha = -1$, are processed with the analysis selection cuts to obtain selection efficiencies $\eta_{\alpha=+1}$ and $\eta_{\alpha=-1}$ respectively. The systematic error is taken as the greatest of the two following fractional differences:

$$\sigma_{\alpha=+1} = \frac{\eta_{\alpha=+1} - \eta_{def}}{\eta_{def}} = -0.5\%, \quad \sigma_{\alpha=-1} = \frac{\eta_{\alpha=-1} - \eta_{def}}{\eta_{def}} = +0.5\% \quad (5.17)$$

where η_{def} is the default selection efficiency for the unweighted sample.

Fermi momentum of nucleon

In the PDK MC sample the momentum of protons decaying in Oxygen is simulated using the experimental spectrum functions (Section 3.4). In the ATM- ν MC the nucleon momentum in Oxygen is modeled by the Fermi Gas Model, which assumes a uniform spherical momentum distribution in 3D phase space whose radius (Fermi surface momentum) is 225 MeV/c: we consider this difference as a systematic uncertainty and we evaluate it by weighting PDK MC proton decay events from Oxygen. Weights are calculated by generating a Fermi Gas Model distribution with a number of entries equal to the number of PDK MC events in true FV and binning it with 25 MeV/c of bin width. The distribution of proton momentum in PDK MC proton decay events from Oxygen is obtained in the same way (Figure 5.14(a)).

The weight w_i for proton decay events from oxygen with proton momentum in the i -th bin is calculated as:

$$w_i = \frac{N_{O_{Fermi,i}}}{N_{O,i}} \quad (5.18)$$

where $N_{O_{Fermi,i}}$ and $N_{O,i}$ are the number of entries in the i -th bin for Fermi Gas Model and PDK MC proton momentum distributions respectively (Figure 5.14(b)). The systematic error σ on signal efficiency is calculated as:

$$\sigma = \frac{\eta_{wei} - \eta_{def}}{\eta_{def}} = -0.6\% \quad (5.19)$$

where η_{wei} is signal efficiency obtained by processing the weighted PDK MC events with analysis selection cuts and η_{def} is the default signal efficiency for the unweighted sample.

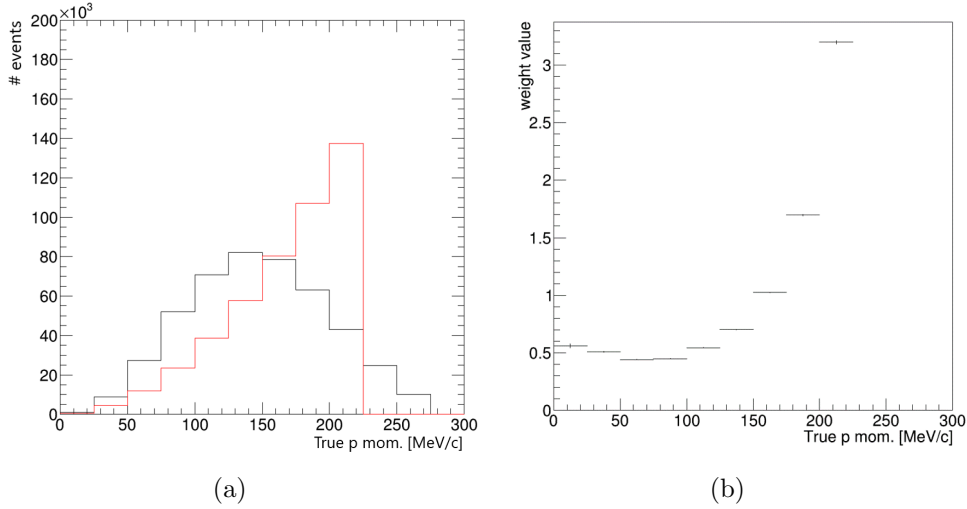


Figure 5.14: The left plot shows the distributions of true proton momentum in Oxygen for PDK MC (black) and Fermi Gas Model (red). The right plot shows the weight values for each momentum bin.

K^+ Final State Interactions (FSI)

We estimated systematic uncertainty from K^+ FSI by comparing the model we used to generate the PDK MC sample with the model in a version of NEUT modified to improve total K^+p cross section (Figure 5.15) consistency with experimental data [19] and to include some bug fixes. The effect of all modifications on Kaon model for FSI are shown in Figure 5.16.

Two contributions to Kaon FSI systematic error on selection efficiency are considered:

- K^+ momentum after FSI,
- K^+ charge exchange.

The first one is evaluated by generating a new PDK MC sample with modified NEUT containing, normalized to the same number of events as the original one, and comparing the distribution of K^+ momentum after FSI in both samples, using the same binning (Figure 5.17). Weights are calculated and applied to PDK MC as in Section 5.6.1.

The same new PDK MC sample is used to evaluate the contribution from charge exchange. Weights are calculated to make the fraction of charge exchange events in the original PDK MC sample equal to that in the new sample. Charge exchange (CX) $K^+ \rightarrow K^0$ events fraction f_{CX} grows from 0.09% in the original PDK MC sample to 1.65% in the new one. The weight

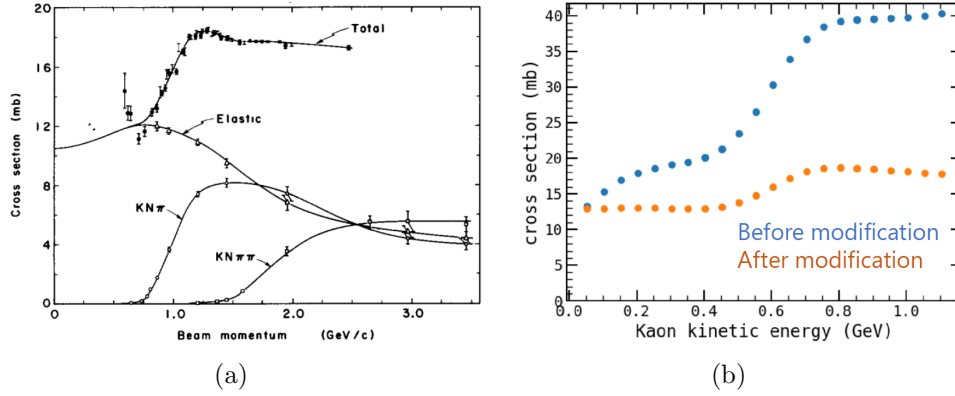


Figure 5.15: The left plot shows K^+p total, elastic, single-pion-production, double-pion-production cross sections as functions of kaon momentum, from [19]. The right plot shows the total K^+p cross section as a function of kaon kinetic energy in NEUT before modification (blue) and after modification (orange) to match the left plot.

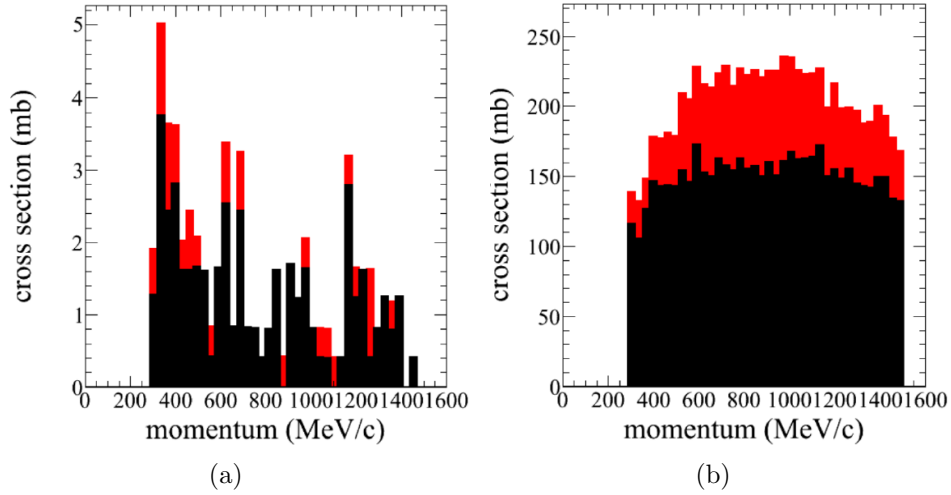


Figure 5.16: Elastic (black) and Charge Exchange (red) $K^{+16}O$ cross sections as functions of K^+ momentum before (left) and after (right) modifications in NEUT.

for true charge exchange events w_{CX} is calculated as:

$$w_{CX} = \frac{f_{CX} \text{ in new sample}}{f_{CX} \text{ in original sample}} = 1.84 \quad (5.20)$$

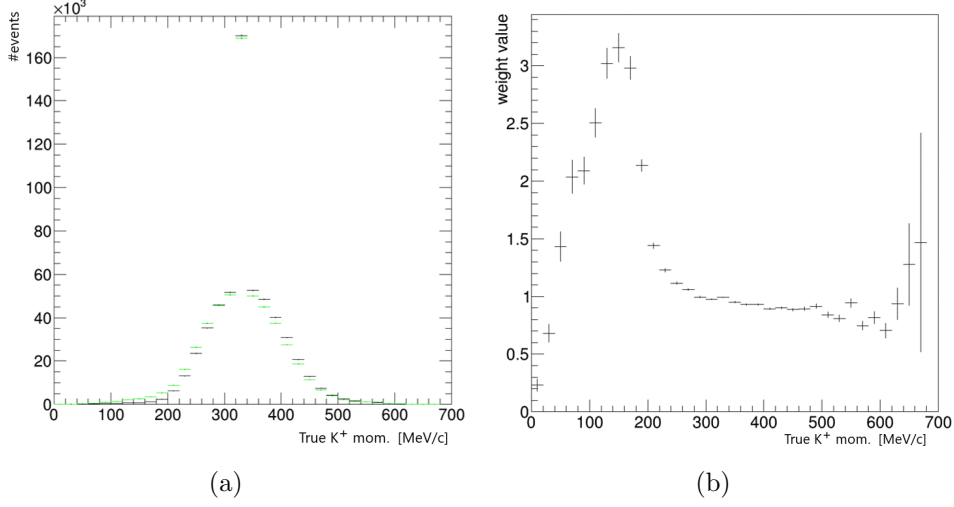


Figure 5.17: The left plot shows true K^+ momentum distributions after FSI for original PDK MC sample (black) and the one generated with modified NEUT (green). The broad distribution represents the contribution of kaons from bound protons while the outlier bin at 339 MeV/c contains the contribution of kaons from free protons as well. The right plot shows the weights calculated from the left plot.

The weight for true non-charge-exchange events w_{noCX} is calculated as:

$$w_{noCX} = \frac{(1 - f_{CX}) \text{ in new sample}}{(1 - f_{CX}) \text{ in original sample}} = 0.99 \quad (5.21)$$

Systematic error on selection efficiency is calculated for each contribution as the fractional difference between selection efficiencies for weighted (η_{wei}) and unweighted (η_{def}) samples:

$$\sigma = \frac{\eta_{wei} - \eta_{def}}{\eta_{def}} \quad (5.22)$$

We found +0.3% for the momentum contribution and -1.6% for the charge exchange contribution.

K^+ Secondary Interactions (SI)

We estimate the systematic uncertainty due to K^+ secondary interactions in water using the same new PDK MC sample and the same method as discussed in Section 5.6.1 for FSI, by comparing true K^+ momentum at decay time distributions (Figure 5.18) and fractions of events with charge

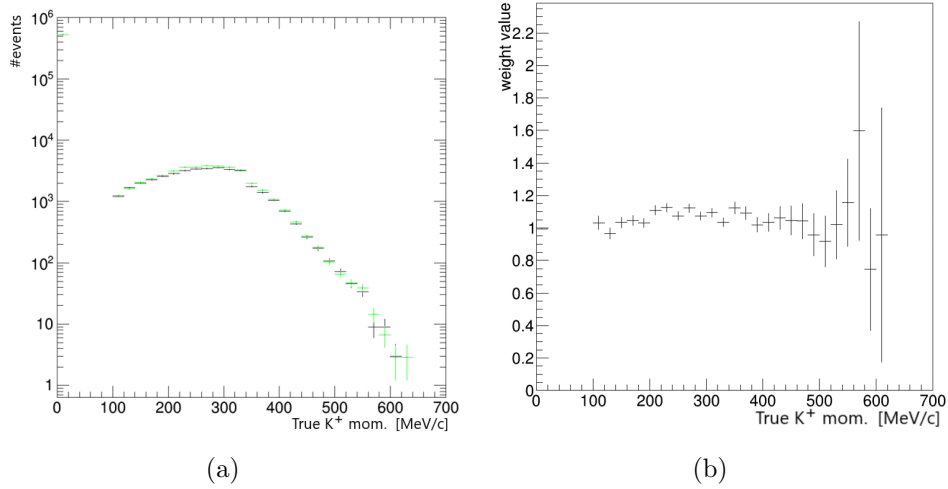


Figure 5.18: The left plot shows true K^+ momentum distributions at decay time after SI simulation for original PDK MC sample (black) and the one generated with modified NEUT (green). The right plot shows the weights calculated from the left plot.

Table 5.4: Fraction of true CX and non-CX events in PDK MC original and new samples and weight values calculated to evaluate systematic error on selection efficiency from K^+ SI.

	in original sample (%)	in new sample (%)	weight value
True CX	0.7	0.2	0.257346
True non-CX	99.3	99.8	1.0055

exchange $K^+ \rightarrow K^0$ in water in both new and original PDK MC samples (Table 5.4).

We found -0.1% for the momentum contribution and +0.5% for the charge exchange contribution.

Pion Secondary Interactions SI

Charged and neutral pion from the decay of K^+ can interact in water: the detector simulator SKDETSIM stores the history and type of these interactions in each event. Possible interactions are: Quasi Elastic (QE), Inelastic Scattering (INEL), Absorption (ABS) and Charge Exchange (CX). 24 sets of coefficients are calculated from experimental results [5] (Table 5.5) and used to change probabilities of interactions and each event probability accordingly: from these coefficients 24 weights are calculated for each event,

one per coefficient set.

Table 5.5: Sets of coefficients to evaluate pion FSI/SI systematic uncertainty. The *High* label means that true pion momentum is over 500 MeV/c at interaction time.

#	QE	QE(High)	INEL	ABS	CX	CX(High)
0(default)	1	1.8	1	1.1	1	1.8
1	0.6	1.8	1	0.7	0.5	1.8
2	0.6	1.8	1	0.7	1.6	1.8
3	0.7	1.8	1	1.6	0.4	1.8
4	0.7	1.8	1	1.6	1.6	1.8
5	1.4	1.8	1	0.6	0.6	1.8
6	1.3	1.8	1	0.7	1.6	1.8
7	1.5	1.8	1	1.5	0.4	1.8
8	1.6	1.8	1	1.6	1.6	1.8
9	0.6	1.1	1.5	0.7	0.5	2.3
10	0.6	1.1	1.5	0.7	1.6	2.3
11	0.7	1.1	1.5	1.6	0.4	2.3
12	0.7	1.1	1.5	1.6	1.6	2.3
13	1.4	1.1	1.5	0.6	0.6	2.3
14	1.3	1.1	1.5	0.7	1.6	2.3
15	1.5	1.1	1.5	1.5	0.4	2.3
16	1.6	1.1	1.5	1.6	1.6	2.3
17	0.6	2.3	0.5	0.7	0.5	1.3
18	0.6	2.3	0.5	0.7	1.6	1.3
19	0.7	2.3	0.5	1.6	0.4	1.3
20	0.7	2.3	0.5	1.6	1.6	1.3
21	1.4	2.3	0.5	0.6	0.6	1.3
22	1.3	2.3	0.5	0.7	1.6	1.3
23	1.5	2.3	0.5	1.5	0.4	1.3
24	1.6	2.3	0.5	1.6	1.6	1.3

The PDK MC is weighted with each of the 24 weighting sets and selection efficiency is evaluated (Figure 5.19). The mean and RMS of the 24 selection efficiencies are calculated and systematic error on selection efficiency is estimated as:

$$\sigma = \frac{\text{RMS}}{\text{Mean}} = 2.3\% \quad (5.23)$$

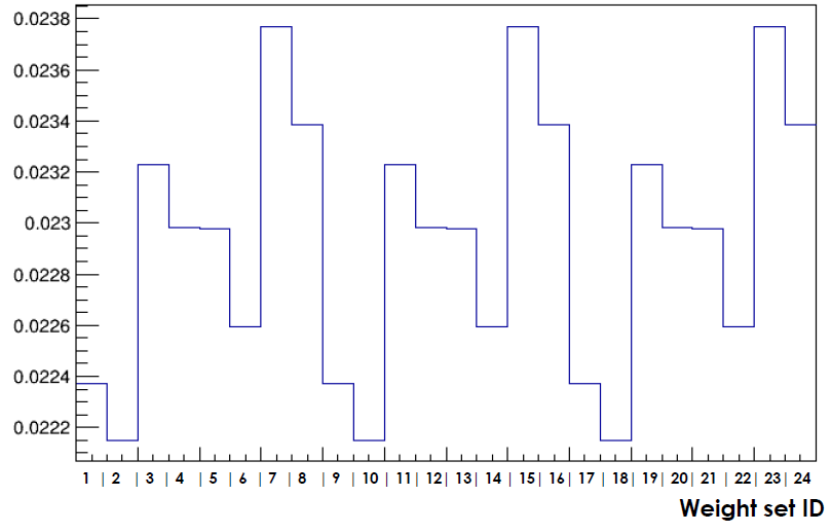


Figure 5.19: Selection efficiency for each pion SI weighting set applied to PDK MC.

5.6.2 Physics model uncertainties for remaining background

We identified these physics model uncertainties for remaining background:

- atmospheric ν flux,
- atmospheric ν cross sections,
- K^+ FSI/SI,
- pion FSI/SI.

Atmospheric ν flux and cross sections

The systematic error on remaining background from atmospheric ν flux and cross sections is evaluated by weighting each event in the ATM- ν MC sample with weighting sets, one per contribution, developed for the atmospheric neutrino analyses in SK as reported in [25] and [50]. The systematic error is taken as the fractional difference between the remaining backgrounds in weighted and unweighted ATM- ν MC samples (Table 5.6 and 5.7).

Table 5.6: Contributions to systematic uncertainty on remaining background from ν flux.

Contribution	Systematic error
0: absolute normalization ($E_\nu < 1$ GeV)	$\pm 10.3\%$
1: absolute normalization ($E_\nu > 1$ GeV)	$< 0.1\%$
2: ν_μ/ν_e ratio ($E_\nu < 1$ GeV)	$\pm 1.0\%$
3: ν_μ/ν_e ratio ($1 \text{ GeV} < E_\nu < 10$ GeV)	$< 0.1\%$
4: ν_μ/ν_e ratio ($E_\nu > 10$ GeV)	$< 0.1\%$
5: anti- ν_e/ν_e ratio ($E_\nu < 1$ GeV)	$< 0.1\%$
6: anti- ν_e/ν_e ratio ($1 \text{ GeV} < E_\nu < 10$ GeV)	$< 0.1\%$
7: anti- ν_e/ν_e ratio ($E_\nu > 10$ GeV)	$< 0.1\%$
8: anti- ν_μ/ν_μ ratio ($E_\nu < 1$ GeV)	$\pm 1.0\%$
9: anti- ν_μ/ν_μ ratio ($1 \text{ GeV} < E_\nu < 10$ GeV)	$< 0.1\%$
10: anti- ν_μ/ν_μ ratio ($E_\nu > 10$ GeV)	$< 0.1\%$
11: up/down ratio	$\pm 0.2\%$
12: horizontal/vertical ratio	$\pm 1.2\%$
13: K/ π ratio	$\pm 4.2\%$
14: ν flight length	$\pm 0.7\%$
Total	$\pm 11.3\%$

 Table 5.7: Contributions to systematic uncertainty on remaining background from ν cross sections.

Contribution	Systematic error
15: M_A in QE and single- π production	$\pm 5.7\%$
16: NCEL and CCQE ratio	$< 0.1\%$
17: CCQE anti- ν/ν ratio	$< 0.1\%$
18: CCQE μ/e ratio	$< 0.1\%$
19: single meson production	$\pm 20.0\%$
20: single- π production anti- ν/ν ratio	$\pm 35.0\%$
21: DIS (model comparison)	$< 0.1\%$
22: DIS	$< 0.1\%$
23: coherent π production	$< 0.1\%$
24: NC/CC ratio	$< 0.1\%$
Total	± 40.7

K^+ FSI/SI

Considering that no background events containing K^+ remain (Section 5.5.1) we assign a systematic error on remaining background of $\sim 0\%$ from system-

atic uncertainty on K^+ FSI/SI model.

Pion FSI/SI

The systematic error on remaining background from Pion FSI/SI model uncertainty is calculated in the same way as described in Section 5.6.1. In particular, information about FSI interactions is stored by NEUT in each event as well as SI interaction information is stored by the detector simulator SKDETSIM. Figure 5.20 shows the remaining background for each Pion FSI weight applied to ATM- ν MC sample. Events in the remaining background (Section 5.5.1) contain only neutral pions that decay after $\sim 10^{-16}$ s: for this reason they are not expected to survive long enough to be subject to Secondary Interactions in water. Therefore systematic error on remaining background from Pion SI model systematic uncertainty is negligible.

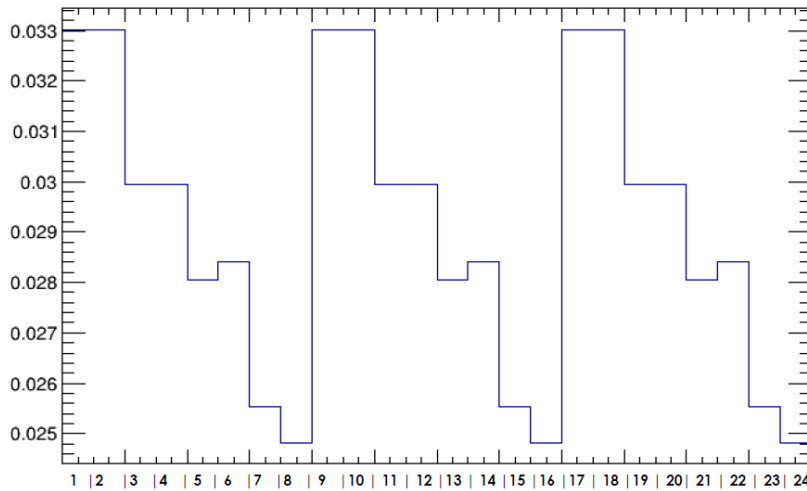


Figure 5.20: Remaining background for each Pion FSI weighting set applied to ATM- ν MC.

We found a value of 10.3% for the systematic error on remaining background from Pion FSI model systematic uncertainty.

5.6.3 Detector uncertainties

There are several sources of uncertainty in our detector that can affect the analysis:

- propagation of light in water,

- reflections of light on inner surfaces,
- PMT responses,
- energy scale.

Even if these items are subject to accurate calibrations (Section 2.4) a perfect knowledge of the detector is unrealistic: this fact impacts on the simulations used to estimate selection efficiency and remaining background. A real proton decay control sample to estimate detector uncertainty impact on this analysis is not available, so we built a control sample made of events obtained by merging real data with simulated data, known as *hybrid sample* (Section 5.6.4).

Other uncertainty sources couldn't be estimated by using the hybrid sample since it's missing all the necessary information:

- *Michel electrons* count,
- tagged neutrons count.

They are estimated separately.

***Michel electrons* count**

The systematic error from *Michel electrons* count is estimated by applying the analysis event selections, as explained in Section 5.3, up to **PID** cut to both FCFV real data and ATM- ν MC and comparing the two distributions of counted *Michel electrons* obtained by normalizing the MC one by total number of events (Figure 5.21).

The systematic error σ is evaluated by calculating the fractional difference ϵ between the number of MC ($\#MC$) and real data ($\#DATA$) events passing the **Michel** cut (as defined in Section 5.3), summed in quadrature with its statistical error σ_ϵ :

$$\epsilon = \frac{\#MC - \#DATA}{\#DATA} \quad (5.24)$$

$$\sigma = \sqrt{\epsilon^2 + \sigma_\epsilon^2} = \sqrt{2.3\%^2 + 1.9\%^2} = \pm 3.0\% \quad (5.25)$$

Tagged neutrons count

The systematic error from tagged neutrons count is estimated by applying the analysis event selections, as explained in Section 5.3, up to **Michel** cut (as defined in Section 5.3) to both FCFV real data and ATM- ν MC and

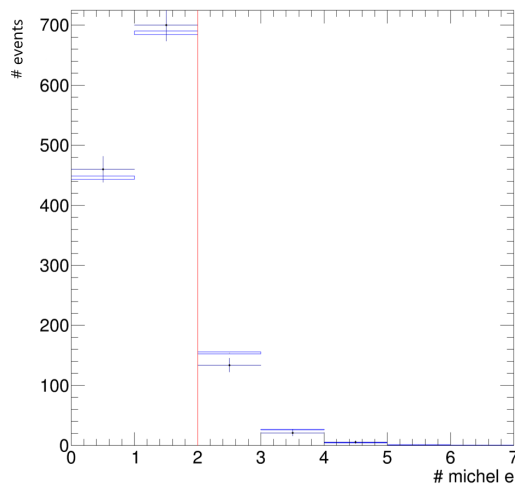


Figure 5.21: Distributions of counted Michel electrons in real FCFV data (black) and ATM- ν MC (blue) samples after **nring** and **PID** cuts. ATM- ν distribution is normalized to the total number of real data events in the plot.

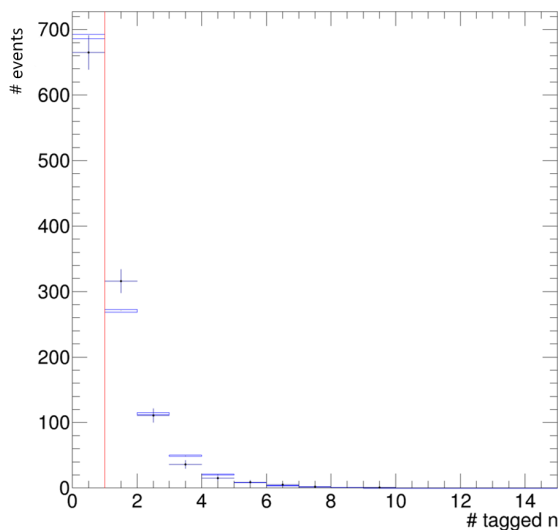


Figure 5.22: Distributions of counted *Michel electrons* in real FCFV data (black) and ATM- ν MC (blue) samples after **nring**, **PID** and **michel** cuts. ATM- ν distribution is normalized to the total number of real data events in the plot.

comparing the two distributions of counted *Michel electrons* obtained by normalizing the MC one by total number of events (Figure 5.21).

The calculation is the same as in the *Michel electrons* count case:

$$\sigma = \sqrt{\epsilon^2 + \sigma_\epsilon^2} = \sqrt{3.7\%^2 + 4.1\%^2} = \pm 5.5\% \quad (5.26)$$

5.6.4 Hybrid sample

Hybrid samples contain events built to mimic the signal final state $\pi^+\gamma\gamma$ kinematics (Section 5.2.1). Four hybrid samples are used, their events are composed as follows (Figure 5.23):

- **primary DATA sample:** a single e-like ring event from real ATM- ν CCQE data is selected, reconstructed and matched by energy and direction to the most energetic photon from a simulated signal event, then the remaining e-like and π -like rings are simulated accordingly and merged to it;
- **primary MC sample:** same as the primary DATA sample, but the single e-like ring event is selected from the ATM- ν MC sample and reconstructed, its Monte Carlo truth is ignored;
- **secondary DATA sample:** same as the primary DATA sample, but the single e-like ring is selected from the ATM- ν CCQE or stopping- μ real data repositories and matched to the least energetic photon from a simulated signal event;
- **secondary MC sample:** same as the primary MC sample, but the single e-like ring from ATM- ν or stopping- μ MC is matched to the least energetic photon from a simulated signal event.

The building process is performed using *APFit* reconstructed information, since its performance is well known compared to *fitQun*. Unfortunately, this prevents us from building a tertiary sample with single π -like ring events from real data since *APFit* has no π -like ring hypothesis. Also, such rings would be too few to have sufficient statistics for this study.

Construction of primary DATA and MC hybrid samples

As a first step, the single e-like ring events from the ATM- ν real data (for DATA sample) or ATM- ν MC (for MC sample) repositories are selected by the following criteria:

1. the event is FCFV,
2. the total visible energy (E_{vis}) is > 30 MeV,

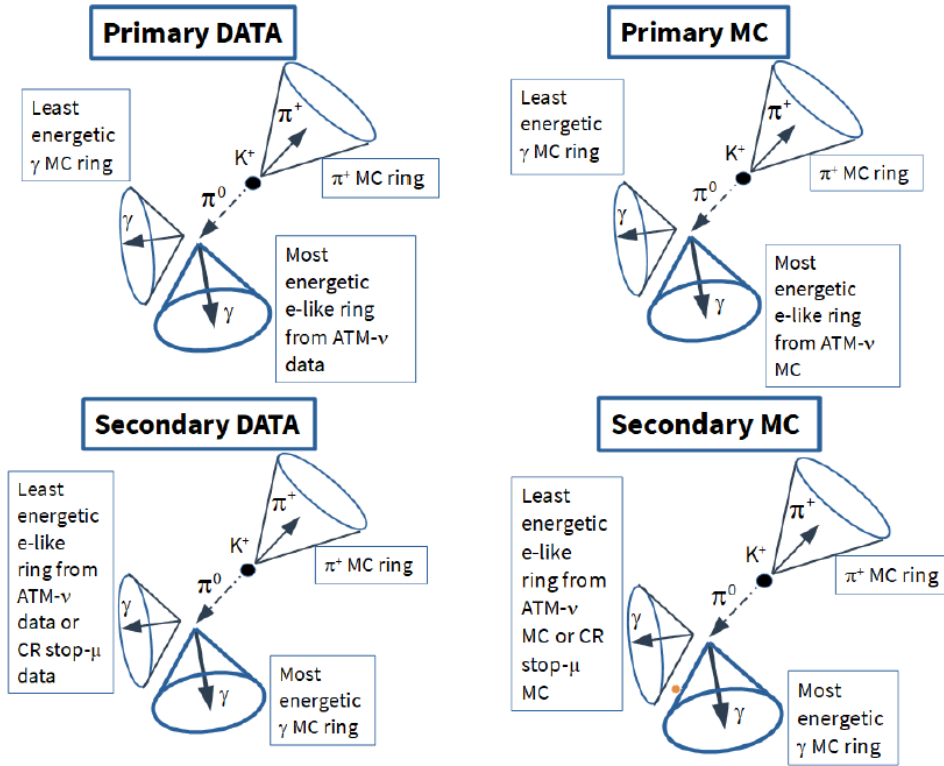


Figure 5.23: Composition of the events in the four evaluated hybrid samples.

3. the number of reconstructed rings is 1,
4. the reconstructed ring is e-like,
5. the goodness of the fit provided by APFit is > 0.6 ,
6. the e-like ring is unlikely to come from a π^0 decay (invariant mass for π^0 hypothesis by APFit $< 100 \text{ MeV}/c^2$).

Each selected event is given an identification number (*iseq*) to track their re-use at analysis time: if multiple events share rings with the same *iseq* they are not independent and this is taken into account when computing statistical errors.

In the second step, for each true $\pi^+\pi^0$ PDK MC event its kinematics are extracted: for each particle in the final state momentum, direction and production vertex are recorded. Production vertexes of photons are corrected for conversion length in water ($\sim 40 \text{ cm}$), since it's only after conversion that Cherenkov light is produced.

In the third step each event kinematics extracted in the second step are associated to one single e-like ring event from the first step. For each single e-like ring, the event particle directions are rotated together to let the most energetic gamma true direction match the e-like ring reconstructed direction. Two rotation axes are defined:

1. the direction of the escaping neutrino from the $p \rightarrow \nu K^+$ decay,
2. the z-axis of the detector, which corresponds to the vertical axis of symmetry of the ID cylinder.

If no matches are found the event is discarded. Among all the found matches, the ring whose reconstructed energy is the closest to the photon true energy is chosen.

In the fourth step, for each vector with a match, the rings from the least energetic photon and charged pion are simulated by SKDETSIM using the rotated kinematics information and merged with the chosen single e-like ring in a single hybrid event (Figure 5.24).

In the fifth step the hybrid events are reconstructed with fitQun.

Construction of secondary DATA and MC hybrid samples

The steps are the same as in the construction of the primary samples but in this case two different kinds of single e-like rings are used to be matched with the least energetic photon of the PDK MC kinematics: single e-like ring events from ATM- ν CCQE interactions, used to match least energetic photons with true energies > 60 MeV, and single e-like rings from the decay electron of cosmic muons stopping in the ID tank produced at least $2.0 \mu\text{s}$ after the primary muon event, used to match least energetic photons with true energies < 60 MeV.

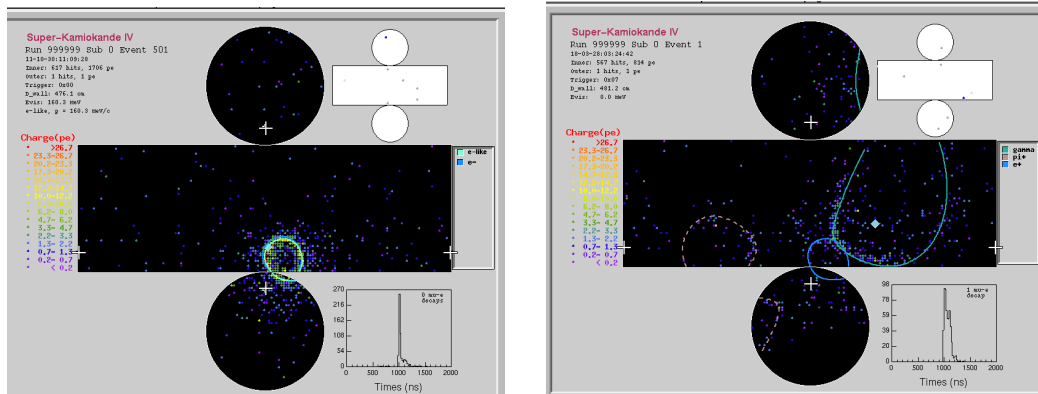
Error calculation taking into account the re-use of rings

Events in the final hybrid samples are not independent from each other: several of them may share the same single e-like rings used during construction, each one identified by its own *iseq* number.

Each *iseq* identifies a class of events: we assume that the number of events from each class passing the cuts, or being counted in a bin, k_{iseq} follows the Poisson distribution, each one with a different expected value.

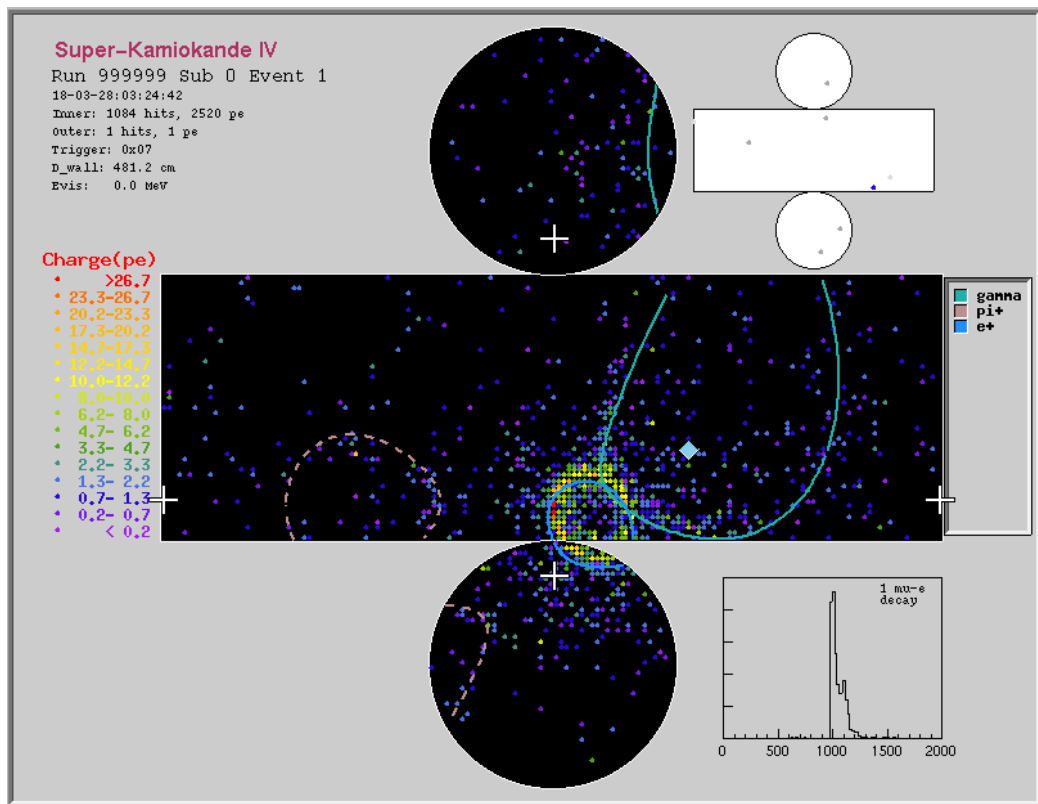
Breaking up the total number of events in a bin, or passing the cuts, k as

$$k = \sum_{\text{iseq}} k_{\text{iseq}} \quad (5.27)$$



(a) ATM- ν CCQE e-like ring

(b) Simulated rings from PDK MC vector



(c) Rings merged in a hybrid event

Figure 5.24: The ring merging process of an event built for this analysis.

from the well known properties of Poisson distributions, it follows

$$\sigma_k^2 = \sum_{\text{iseq}} \sigma_{k_{\text{iseq}}}^2 = \sum_{\text{iseq}} k_{\text{iseq}}^2 \quad (5.28)$$

Finally, the error on signal efficiency can be calculated as:

$$\sigma_\eta = \frac{\sigma_k}{N} = \frac{1}{N} \sqrt{\sum_{\text{iseq}} k_{\text{iseq}}^2} \quad (5.29)$$

where N is the total number of events generated in the Fiducial Volume.

Distributions along cut parameters

Hybrid samples events are selected using the same cuts as the analysis explained in Section 5.3, except neutron tagging since neutron capture is not simulated in the hybrid samples. Distributions along cut parameters are shown in Figures from 5.25 to 5.32. The distributions have the expected shapes, DATA and MC distributions show no significant disagreements for both the primary and secondary samples. Finally, the fitted value for reconstructed π^0 mass and K^+ mass both agree with the expected values from the PDG [17].

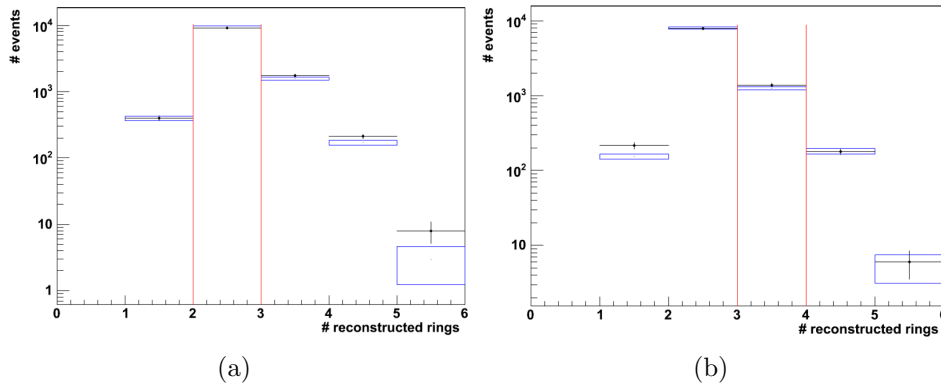


Figure 5.25: Number of reconstructed rings distributions of FCFV hybrid primary (left) and secondary (right) samples. The black dots show the DATA sample, the blue boxes the MC sample in both plots.

Results

The signal efficiencies η after each cut for the primary and secondary samples are shown in Table 5.8 and 5.9 respectively, along with the fractional

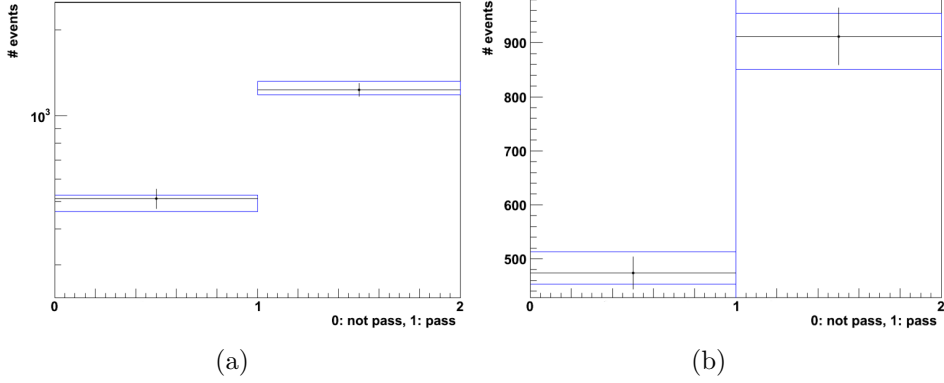


Figure 5.26: Distribution of **PID** after **nring** cut in FCFV hybrid primary (left) and secondary (right) samples. The black dots show the DATA sample, the blue boxes the MC sample in both plots.

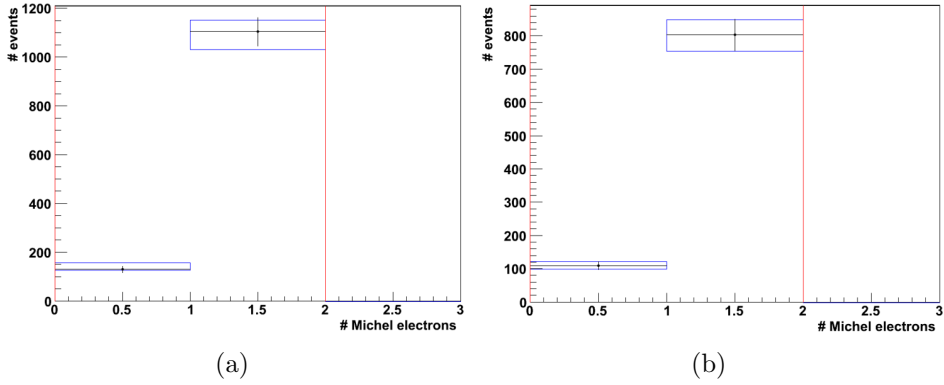


Figure 5.27: Distribution of number of tagged *Michel electrons* after **nring** and **PID** cuts in FCFV hybrid primary (left) and secondary (right) samples. The black dots show the DATA sample, the blue boxes the MC sample in both plots.

differences between MC and DATA efficiencies, defined as:

$$\epsilon = \frac{\eta_{\text{MC}} - \eta_{\text{DATA}}}{\eta_{\text{DATA}}} \quad (5.30)$$

The systematic error for each sample is calculated as:

$$\sigma = \sqrt{\epsilon^2 + \sigma_\epsilon^2} \quad (5.31)$$

where ϵ is the fractional difference after all cuts and σ_ϵ is its statistical error. By substituting numbers we obtain:

$$\sigma_{\text{primary}} = \sqrt{1.81\%^2 + 10.83\%^2} = 10.98\% \quad (5.32)$$

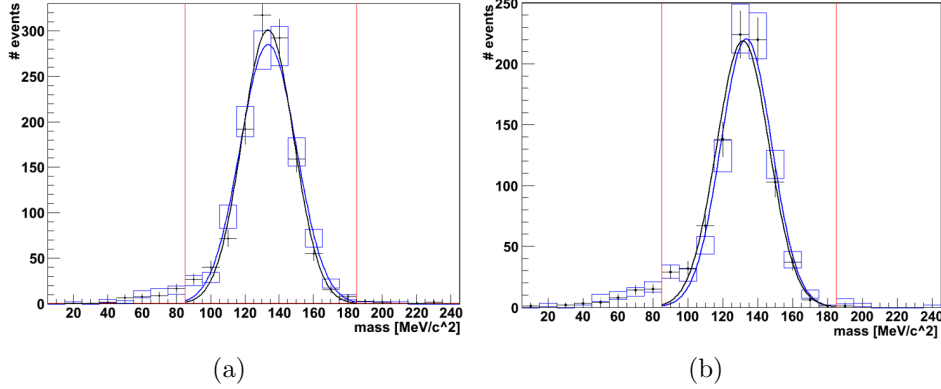


Figure 5.28: Distribution of reconstructed π^0 mass (M_{π^0}) after **nring**, **PID** and **micel** cuts in FCFV hybrid primary (left) and secondary (right) samples. The black dots show the DATA sample, the blue boxes the MC sample in both plots. Solid lines show gaussian fits for DATA and MC samples. Fitted values are: primary DATA $133.4 \pm 4.7 \text{ MeV}/c^2$, primary MC $133.6 \pm 5.2 \text{ MeV}/c^2$, secondary DATA $131.8 \pm 4.8 \text{ MeV}/c^2$, secondary MC $133.7 \pm 4.6 \text{ MeV}/c^2$.

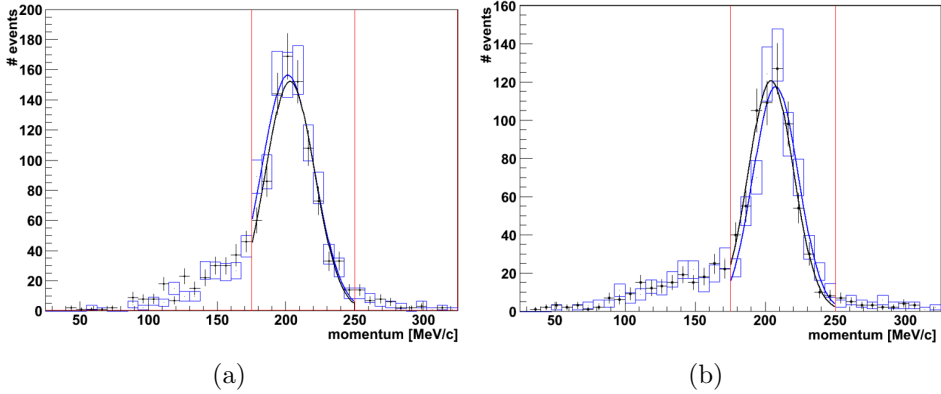


Figure 5.29: Distribution of reconstructed π^0 momentum (P_{π^0}) after **nring**, **PID**, **micel** and M_{π^0} cuts in FCFV hybrid primary (left) and secondary (right) samples. The black dots show the DATA sample, the blue boxes the MC sample in both plots. Solid lines show gaussian fits for DATA and MC samples. Fitted values are: primary DATA $203.1 \pm 5.6 \text{ MeV}/c$, primary MC $201.5 \pm 6.0 \text{ MeV}/c$, secondary DATA $204.3 \pm 5.1 \text{ MeV}/c$, secondary MC $207.6 \pm 5.1 \text{ MeV}/c$.

$$\sigma_{\text{secondary}} = \sqrt{20.96\%^2 + 10.38\%^2} = 23.39\% \quad (5.33)$$

The final systematic error is calculated by summing the systematic error

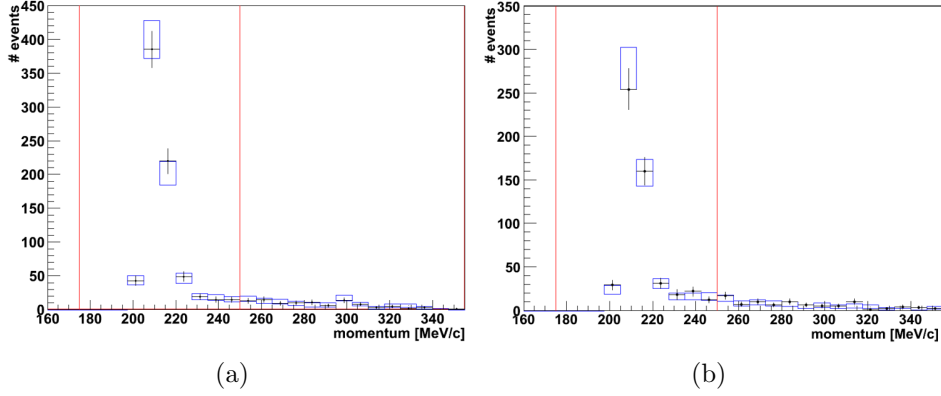


Figure 5.30: Distribution of reconstructed π^+ momentum (P_{π^+}) after **nring**, **PID**, **michel**, M_{π^0} and P_{π^0} cuts in FCFV hybrid primary (left) and secondary (right) samples. The black dots show the DATA sample, the blue boxes the MC sample in both plots.

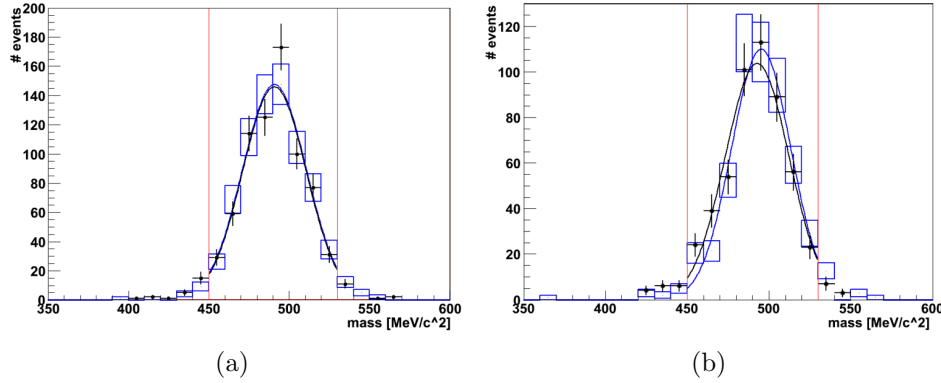


Figure 5.31: Distribution of reconstructed K^+ mass (M_{K^+}) after **nring**, **PID**, **michel**, M_{π^0} , P_{π^0} and P_{π^+} cuts in FCFV hybrid primary (left) and secondary (right) samples. The black dots show the DATA sample, the blue boxes the MC sample in both plots. Solid lines show gaussian fits for DATA and MC samples. Fitted values are: primary DATA 490.8 ± 7.0 MeV/ c^2 , primary MC 490.8 ± 7.0 MeV/ c^2 , secondary DATA 492.9 ± 6.9 MeV/ c^2 , secondary MC 495.3 ± 6.4 MeV/ c^2 .

from primary and secondary sample in quadrature:

$$\sigma_{\text{final}} = \sqrt{\sigma_{\text{primary}}^2 + \sigma_{\text{secondary}}^2} = 25.84\% \quad (5.34)$$

This value for the systematic error is dominated by statistical error and probably overestimated: hybrid sample statistics is limited by the amount of

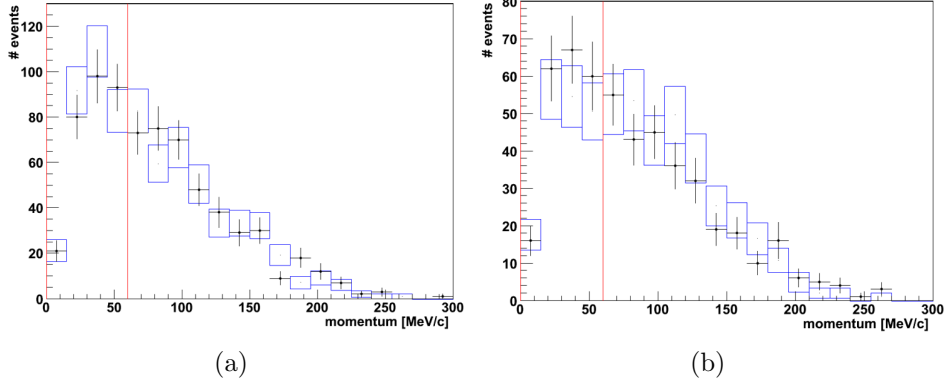


Figure 5.32: Distribution of reconstructed K^+ momentum (P_{K^+}) after **nring**, **PID**, **michel**, M_{π^0} , P_{π^0} , P_{π^+} and M_{K^+} cuts in FCFV hybrid primary (left) and secondary (right) samples. The black dots show the DATA sample, the blue boxes the MC sample in both plots.

Table 5.8: Signal efficiency η after each cut for the primary hybrid MC and DATA samples and their fractional difference ϵ .

Cut	η_{MC} (%)	η_{DATA} (%)	ϵ (%)
nring	13.77 ± 0.68	15.28 ± 0.78	-9.85 ± 6.38
+PID	9.88 ± 0.53	10.79 ± 0.57	-8.51 ± 6.88
+michel	9.85 ± 0.53	10.77 ± 0.57	-8.52 ± 6.90
$+M_{\pi^0}$	9.42 ± 0.52	10.30 ± 0.54	-8.51 ± 6.95
$+P_{\pi^0}$	7.28 ± 0.43	7.40 ± 0.43	-1.56 ± 8.20
$+P_{\pi^+}$	6.34 ± 0.39	6.53 ± 0.39	-2.88 ± 8.31
$+M_{K^+}$	6.05 ± 0.37	6.19 ± 0.38	-2.26 ± 8.45
$+P_{K^+}$	2.60 ± 0.19	2.56 ± 0.19	1.81 ± 10.83

real data used, in this case the whole span of SK-IV data, thus it can't be improved further for SK-IV.

5.6.5 Summary of systematic errors

The results of systematic error estimations are summarized in Table 5.10 for selection efficiency and Table 5.11 for remaining background.

Table 5.9: Signal efficiency η after each cut for the secondary hybrid MC and DATA samples and their fractional difference ϵ .

Cut	η_{MC} (%)	η_{DATA} (%)	ϵ (%)
nring	13.13 ± 0.67	14.44 ± 0.75	-9.08 ± 6.62
+PID	8.55 ± 0.49	9.50 ± 0.55	-10.01 ± 7.34
+michel	8.51 ± 0.49	9.43 ± 0.55	-9.80 ± 7.40
+ M_{π^0}	7.93 ± 0.47	8.91 ± 0.53	-11.01 ± 7.48
+ P_{π^0}	5.65 ± 0.39	6.39 ± 0.43	-11.51 ± 8.59
+ P_{π^+}	4.96 ± 0.35	5.47 ± 0.39	-9.25 ± 9.13
+ M_{K^+}	4.71 ± 0.34	5.19 ± 0.38	-9.29 ± 9.34
+ P_{K^+}	1.69 ± 0.16	2.14 ± 0.19	-20.96 ± 10.38

Table 5.10: Systematic errors for signal efficiency.

Source of uncertainty	Systematic error
Physics model	
Correlated nucleon decay	$\pm 0.5\%$
Fermi momentum of nucleon	- 0.6%
K^+ FSI: momentum	+ 0.2%
K^+ FSI: CX	- 1.6%
K^+ SI: momentum	- 0.1%
K^+ SI: CX	+ 0.5%
Pion SI	$\pm 2.3\%$
Detector	
Propagation of light in water	
Reflections of light on inner surfaces	
PMT responses	
Energy scale	$\pm 25.8\%$
<i>Michel electron</i> count	$\pm 3.0\%$
Total	$\pm 26.1\%$

5.7 Lifetime limit calculation

Since we found no candidate events, we calculated lower limits on the proton partial lifetime using a Bayesian method [40].

The probability to detect n candidate events is calculated by Poisson statistics:

$$P(n|\Gamma\lambda\epsilon b) = \frac{e^{-(\Gamma\lambda+b)} (\Gamma\lambda\epsilon + b)^n}{n!} \quad (5.35)$$

Table 5.11: Systematic errors for remaining background.

Source of uncertainty	Systematic error
Physics model	
Atmospheric ν flux	$\pm 11.3\%$
Atmospheric ν cross sections	$\pm 40.7\%$
K^+ FSI/SI	$\sim 0\%$
Pion FSI/SI	$\pm 10.3\%$
Detector	
Propagation of light in water	
Reflections of light on inner surfaces	
PMT responses	
Energy scale	$\pm 25.8\%$
Michel electron count	$\pm 3.0\%$
Tagged neutrons count	$\pm 5.5\%$
Total	$\pm 50.9\%$

where Γ is the true decay rate, λ is the true detector exposure, ϵ is the true signal selection efficiency and b is the true number of remaining background events. Using Bayes' theorem we obtain:

$$\begin{aligned}
 P(\Gamma\lambda\epsilon b|n)P(n) &= P(n|\Gamma\lambda\epsilon b)P(\Gamma\lambda\epsilon b) \\
 &= P(n|\Gamma\lambda\epsilon b)P(\Gamma)P(\lambda)P(\epsilon)P(b)
 \end{aligned} \tag{5.36}$$

where $P(X)$ stands for the prior probability of X and the second equality holds because Γ , λ , ϵ and b are independent.

The probability density function of the decay rate is defined as follows:

$$\begin{aligned}
 P(\Gamma|n) &= \int \int \int P(\Gamma\lambda\epsilon b|n)d\lambda d\epsilon db \\
 &= \frac{1}{A} \int \int \int \frac{e^{-(\Gamma\lambda\epsilon+b)} (\Gamma\lambda\epsilon+b)^n}{n!} P(\Gamma)P(\lambda)P(\epsilon)P(b) d\lambda d\epsilon db
 \end{aligned} \tag{5.37}$$

where A is the normalization factor:

$$A = \int_0^\infty P(\Gamma|n) d\Gamma \tag{5.38}$$

We assume that $P(\Gamma)$ is uniform and that $P(\lambda)$ and $P(\epsilon)$ are Gaussian:

$$P(\lambda) \propto e^{-\frac{(\lambda-\lambda_0)^2}{2\sigma_\lambda^2}} \tag{5.39}$$

$$P(\epsilon) \propto e^{-\frac{(\epsilon-\epsilon_0)^2}{2\sigma_\epsilon^2}} \quad (5.40)$$

where λ_0 and ϵ_0 are the estimates of exposure and signal selection efficiency respectively, and σ_λ and σ_ϵ their systematic errors. The probability of the number of remaining background events is calculated as a convolution of Poisson and Gaussian distributions:

$$P(b) \propto \int_0^\infty \frac{e^{-B} B^{n_b}}{n_b!} e^{-\frac{(Cb-B)^2}{2\sigma_b^2}} dB \quad (5.41)$$

where n_b is the number of remaining background events in the 500 year ATM- ν MC sample, C is a factor to normalize MC live time to data live time and σ_b is the systematic error on the number of remaining background events.

The lower limit of the decay rate, Γ_{limit} , at 90% Confidence Level (CL) is calculated as:

$$0.9 = \int_{\Gamma=0}^{\Gamma_{\text{limit}}} P(\Gamma|n) d\Gamma \quad (5.42)$$

The lower limit of the partial lifetime of $p \rightarrow \nu K^+, K^+ \rightarrow \pi^+ \pi^0$ is:

$$\tau/B_{p \rightarrow \nu K^+, K^+ \rightarrow \pi^+ \pi^0} = \frac{1}{\Gamma_{\text{limit}}} \quad (5.43)$$

In this analysis we have measured a lower partial lifetime limit:

$$\tau/B_{p \rightarrow \nu K^+, K^+ \rightarrow \pi^+ \pi^0} = 6.7 \times 10^{32} \quad (5.44)$$

which is less stringent than the one in the latest reference analysis using *APFit* (2017) (Table 5.12).

Table 5.12: Summary of results for $p \rightarrow \nu K^+, K^+ \rightarrow \pi^+ \pi^0$ analysis using SK-IV only data (3244.4 days). Reference results are from Super-Kamiokande Collaboration Meeting, November 2017.

	This analysis	2017 analysis
Exposure (kton*year)	200	177
# Remaining background	0.03 ± 0.02	0.14
Sys. err. on remaining background (%)	50.9	31.6
Signal selection efficiency (%)	2.9 ± 0.02	9.4 ± 0.1
Sys. err. on signal selection efficiency (%)	26.1	8.7
# data candidates	0	0
Limit (years)	6.7×10^{32}	2.4×10^{33}

5.8 Conclusions and perspectives

We searched for proton decay $p \rightarrow \nu K^+, K^+ \rightarrow \pi^+ \pi^0$ in the full livetime of SK-IV equivalent to an exposure of 200 kton*years using the reconstruction algorithm *fiTQun*. The final results are shown in Table 5.12. We found no data candidates, same as 2017 reference analysis which used *APFit*. Our method has a signal selection efficiency about 3 times lower than the reference analysis but almost 4 times less remaining background is expected. Even if we didn't provide a more stringent lower partial lifetime limit for the proton, we were successful in reconstructing the charged kaon kinematics with *fiTQun*, which contributed to reduce significantly the remaining background, aiming a single event discovery. We also used the hybrid sample technique to produce for the first time a control sample to estimate detector error in this proton decay mode.

Some ideas for future improvements are:

- extend the analysis to other SK epochs,
- include 2-ring events,
- expand Fiducial Volume [60].

Chapter 6

Perspectives: Hyper-Kamiokande

Hyper-Kamiokande (HK) will be the largest water Cherenkov detector in the world [11], currently (2022) under construction, it is expected to start its operations in 2027.

Hyper-Kamiokande is designed to take advantage of the Kamiokande and Super-Kamiokande experience but with some improvements to overcome the new challenges it brings: a larger detector to improve statistics and improved photo-sensors for better efficiency among all.

With ~ 8 times the SK Fiducial Volume, Hyper-Kamiokande will be a natural candidate experiment to detect proton decay.

In this Chapter we present an overview of the Hyper-Kamiokande detector and two studies towards proton decay detection in $p \rightarrow e^+ \pi^0$ mode. Studies of:

- *fitQun* performance in Hyper-Kamiokande,
- tuning of the ring counting parameters of *fitQun*.

6.1 Detector overview

Hyper-Kamiokande relies on the same detection principles as Super-Kamiokande, explained in Section 2.2.1. The detector will be built in the Tochibora mine of the Kamioka Mining and Smelting Company, near the town of Kamioka, Gifu Prefecture, Japan, about 8 km south of Super-Kamiokande and 650 m below the peak of Mount Nijugo, equivalent to 1750 m of water.

The cylindrical cavern to house the detector will have height of 71 m and a diameter of 68 m (Figure 6.1), plus a 16 m high dome on top. The excava-

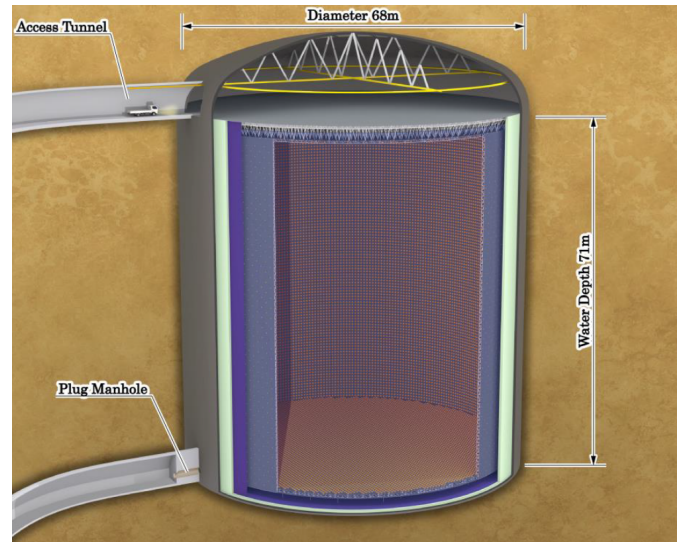


Figure 6.1: Drawing of the HK detector in its cavern

tion works will include smaller caverns for the collateral systems, like water circulation and purification and access tunnels. Two types of photosensors will be employed for physics studies: 20000 Box and Line (B&L) PMTs and a certain number of multi-PMTs (mPMTs), in the order of thousands, yet to be confirmed.

6.1.1 Water tank

The cavern will be covered with a layer of shotcrete and a layer of waterproof lining to prevent ultra pure tank water to leak out and cave water to leak in. A 50 cm thick reinforced concrete layer lined with a 5 mm thick waterproof high-density polyethylene (HDPE) will be added to improve stability and insulation of the tank.

A combination of vertical rectangular coils (y - z plane) and circular coils (x - y plane) will be embedded in the concrete layer to compensate for geomagnetic field in the cave since it negatively affects PMTs collection efficiency.

A stainless-steel structure will separate the inner and outer detector regions and support the PMTs and their covers, as well as front-end electronics (Figure 6.2). While the bottom section will be free-standing on the bottom of the tank, same as in Super-Kamiokande, the barrel and top sections will be suspended from the ceiling of the cavern, reducing frame thickness, weight and cost.

The inner and outer detector regions will be optically insulated to allow

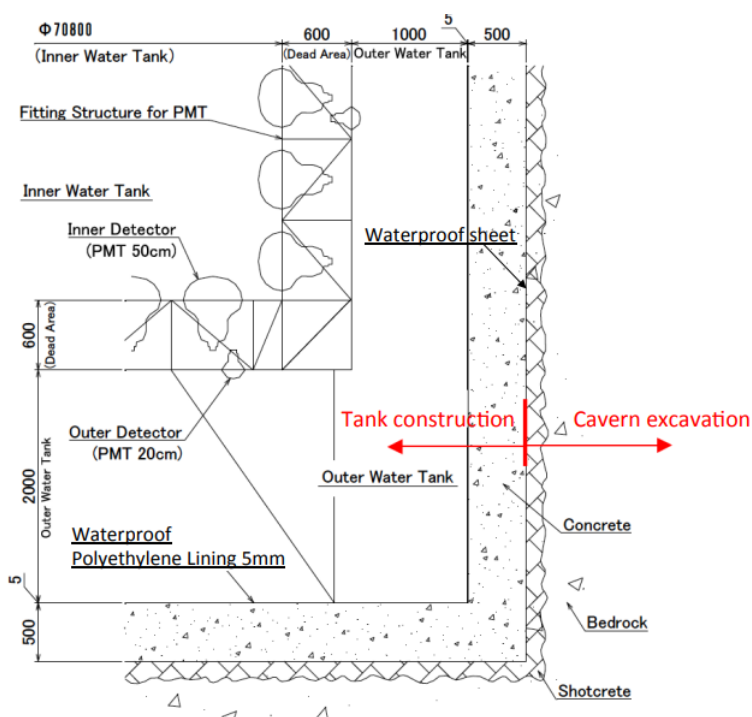


Figure 6.2: Design of the internal structure of the HK detector

the OD to operate as an active veto.

6.1.2 Water purification and circulation system

Water in the tank must be ultra-pure: radon emanating from materials in the tank, like the glass of photosensors and the support structure, and from the surrounding rocks, is a major source of low-energy background that must be removed. Impurities in water can absorb and scatter photons and must be removed as well. In Super-Kamiokande water is constantly re-circulated and purified: a water transparency of over 100 m and a Radon concentration in the ID of less than 1 mBq/m^3 is achieved: in Hyper-Kamiokande the diagonal size is about 100 m, for this reason a similar or better water quality will be required.

The water purification systems will be made of two separate stages: one for tank filling and one for constant re-circulation (Figure 6.3). The water will come from the storage well of the snow-melting system of the town of Kamioka: during filling 105 tons/hour of water will be required to fill the detector with purified water at a rate of 78 tons/hour, such that filling operations will take about six months to be accomplished starting from an

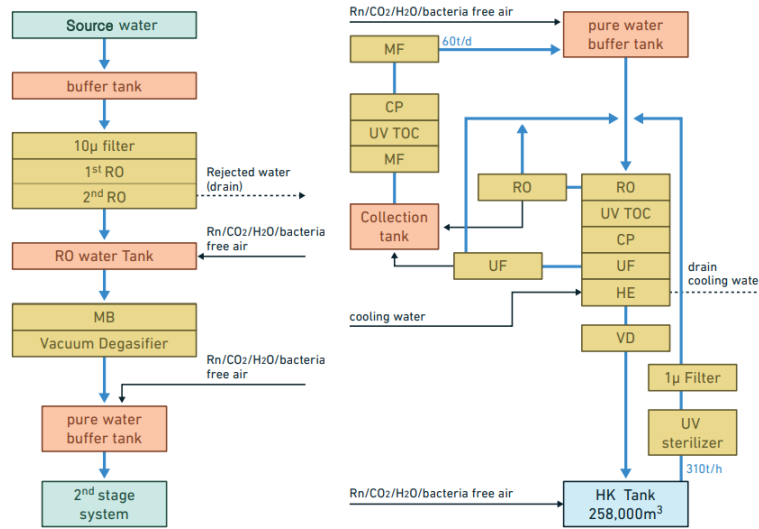


Figure 6.3: Schematic of the HK water system

empty tank. Water will be re-circulated at a rate of 310 tons/hour, such that the total water mass will be re-circulated once per month, same as in Super-Kamiokande.

In the first stage the raw water is passed through a $10\ \mu\text{m}$ filter to remove dust and larger particles and then it's processed with reverse osmosis (RO) and additional filters (MB) to remove smaller particulates. A vacuum degasifier (VD) removes dissolved Oxygen, to quench bacterial growth, and Radon.

In the second stage water coming from the tank is sterilized with UV light and filtered before going through RO, further UV irradiation (UV TOC), a cartridge polisher (CP) that removes heavy ions and more advanced filtration (MV, UF). An heat exchanged (HE) cools water down to remove heath produced by photosensors, electronics and the purification system itself. Finally, cooled water is degasified in a VD and pumped back into the tank.

Radon-free air with a concentration of less than $1\ \text{mBq}/\text{m}^3$ will be used as a cover gas for the tank as well for buffer tanks which are part of the water system. To prevent Radon from entering the inner detector from the surrounding rocks there will be no water exchange between the inner and outer detector.

Water flow will be controlled to improve efficiency of water replacement: simulations show that the best configuration is to supply cold water at the bottom and to drain water at the top, effectively inducing laminar flow and a vertical quality gradient throughout the tank.

6.1.3 Inner Detector (ID)

The inner detector wall is divided into 40000 square cell with a size of 70 cm, which can house a single 50 cm PMT or a single mPMT module each (Figure 6.4).

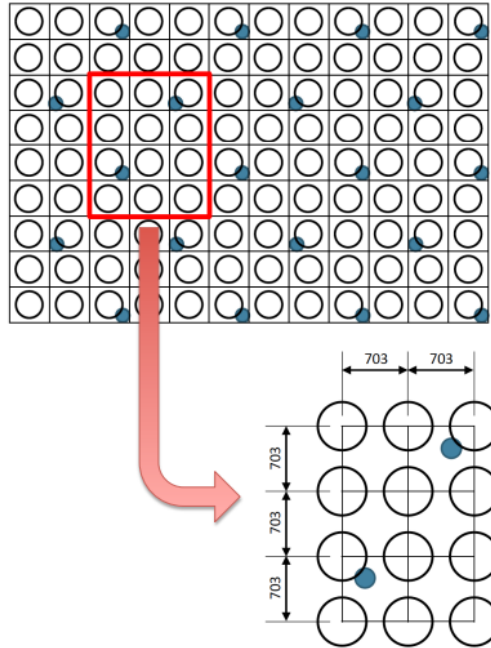


Figure 6.4: Inner detector cells

In this thesis we will consider two ID configurations:

- **20kBL**: 19620 50 cm B&L PMTs,
- **20kBL+10kmPMT**: 19208 50 cm B&L PMTs plus 9616 mPMT modules.

In our simulations the ID has a radius of 32.4 m and it's 65.751 cm high.

B&L PMTs

The Hamamatsu R12860-HQE is a new 50 cm PMT model (Figure 6.5) with a higher quantum efficiency and a box-and-line (B&L) dynode developed for Hyper-Kamiokande. It features twice the total detection efficiency for a single photon with respect to Super-Kamiokande R3600 PMTs by combining an improved quantum efficiency (30% at 390 nm) (Figure 6.6(a)) and capture

them under real conditions and check gain and dark rate stability over time. Current design considers a dark rate of 4.2 kHz.

B&L PMTs also feature mechanical improvements in their bulb shape and thickness, optimized to survive below 60 m of water (0.6 MPa pressure).

Multi-PMT

Multi-PMTs (mPMTs) are composite hemispherical photosensors made of 19 smaller 7.7 cm PMTs (Figure 6.7), developed from an original design by the KM3NeT collaboration to operate in the depths of the Mediterranean Sea.

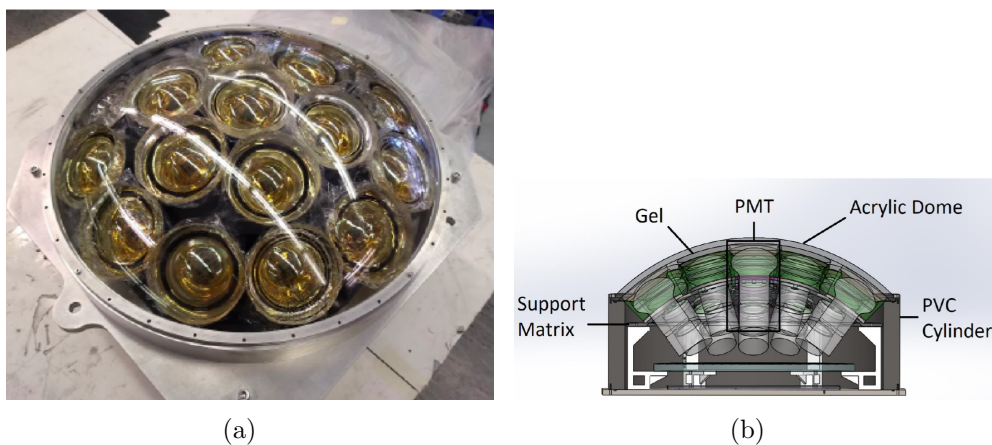


Figure 6.7: Picture (left) and drawing (right) of a mPMT photodetector

The mPMT module to be installed in Hyper-Kamiokande is made of a cylindrical structure, which contains electronics and a support structure holding the PMTs in place. The photosensitive surface of each PMT is surrounded by a conical reflector that increases light collection by 20%. An acrylic window is placed in front of the PMTs and coupled to them with optical gel. The main advantage of mPMTs with respect to B&L PMTs is their higher granularity, which may improve reconstruction performance of events close to the ID wall or for separating overlapping Cherenkov rings in multi-ring events, like proton decay candidates. Different PMTs in the mPMT modules have different fields of view: this can be exploited to identify dark noise in the elements facing away from the reconstructed event vertex, which would improve reconstruction performance especially for low energy events. Finally, the smaller PMTs may be less sensitive to external magnetic fields and show a better timing resolution. All these improvements come at

the cost of a significantly smaller sensitive area with respect to a 50 cm B&L PMT.

6.1.4 Outer Detector (OD)

In Super-Kamiokande the outer detector is approximately 2 m wide and equipped with 1885 20 cm PMTs that provide a photocoverage of 1% and are attached to wavelength shifting plates that increase light collection by about 50%. A 0.6 m wide dead space separates the ID from the OD. In Hyper-Kamiokande 7.7 cm PMTs (0.21% and 0.42% photo-coverage respectively) have been considered by providing a more uniform coverage.

Light collection

Eljen EJ-286 wavelength shifting plates will be optically coupled by contact around each PMT to increase light collection: the plates absorb photons ranging between 280 nm and 400 nm and re-emit them with wavelengths between 410 nm and 460 nm, close to the peak wavelength of PMTs quantum efficiency. Computer simulations and laboratory tests show that adding square plates with a size of 60 cm around each PMT would increase light collection by a factor 3, achieving an effective photocoverage of about 1%, same as Super-Kamiokande.

The outer wall of the OD will be lined with a sheet of highly reflective Tyvek to help recognizing outgoing muon events.

6.1.5 Electronics

Front-end electronics provide PMTs with the necessary high voltage and collect and digitize time and charge data whenever a hit is detected, buffering them if necessary waiting to deliver them to the data acquisition system.

In Hyper-Kamiokande front-end electronics modules are mounted on the PMT support structure and serve 24 nearby PMTs. Only one cable per module descends into the tank from the electronics hut on top, reducing cable cost and weight. Since the connection is digital, no signal degradation is expected to happen due to cable length, which can reach 100 m for some PMTs.

Front-end modules need to be water-tight and pressure-resistant, as well as their connectors. Their case will be constructed from stainless steel to achieve good heat exchange but at the same time power consumption must be limited to avoid convection in nearby water due to heat dissipation.

ID electronics

The electronics module for the ID is made of the following components:

- **power supply:** a single cable delivers DC power from the dome to each electronics module, 48 V by baseline design. A low voltage power supply system (LV PS) feeds the other components, while a separate stable and low-noise high voltage (HV) system feeds photosensors. Power consumption is expected to be below 1 W per channel;
- **signal digitizer:** a single signal digitizer module collects charge information from 24 PMTs and digitizes it at a maximum rate of 1 MHz per PMT;
- **clock and counter system:** the clock system is designed to provide uniform timing across the detector within 100 ps. A master clock generator is located above the water tank: it uses GPS and an atomic clock to generate reference clock and counter signals, and sends them over optical fiber connections to a distribution network serving the modules in the tank. Each module contains a clock and counter component with two optical interfaces for fault tolerance. It also works as a communication module for the digitizer, sending status and number of digitized hits to the dome via the distribution network;
- **data handling and digitizer control:** the data handling and digitizer control component stores data from the digitizer in a dedicated 8 GB buffer, enough for several minutes of operation, before sending it to the read-out system. This block implements data error checking and can include data compression;
- **slow control:** the slow control component monitors environmental conditions inside the electronics module using temperature and humidity sensors. It also monitors low and high voltages and can control HV and current for each channel following commands from the digitizer control component;
- **system control and network interface:** the system control and network interface component routes communications between components inside the module and between the module and the main electronics in the dome via multiple redundant optical interfaces. Data transfers use TCP/IP for error detection and correction while control commands and monitoring use UDP/IP.

OD electronics

The electronics modules for the OD are likely to be very similar to those for the ID: 7.7 cm PMTs require lower HV (600 V to 1100 V) and their use as a veto requires less precise charge and timing information. The cost reduction from the replacement of some components with cheaper versions competes with the cost reduction due to mass manufacturing of a single type of electronics module.

Multi-PMT electronics

The mPMT modules contain individual front-end boards for every PMT and one main board per module, which has the same functions as the ID electronics modules.

The Hyper-Kamiokande mPMT electronics has been designed to fulfill the following requirements:

- **timing resolution:** it should be about 500 ps for 1 p.e. and about 200 ps for large p.e. pulses;
- **charge resolution:** 0.1% FWHM in the range ~ 0.05 p.e. up to 25 p.e.;
- **power consumption:** it should be less than 4 W per mPMT module to prevent interference with water circulation and its temperature stability.

6.1.6 DAQ

The data acquisition system (DAQ) collects all PMTs digitized data from the front-end modules in the water tank, combines them to identify events and store them into mass storage for further analysis. The system is made of four components:

- **Readout Buffer Units (RBUs):** the DAQ system will contain 70 RBUs connected to the front-end electronics modules via a Gigabit network switch for load balance and re-routing in case of failure. Each RBU reads digitized signals from about 30 front-end modules: it buffers all data in memory for 100 seconds and temporarily saves older data to hard drives for one hour. RBUs also reduce data by removing all PMT signals below hit threshold (0.25 photoelectrons, same as Super-Kamiokande) and makes them available to trigger processing and event building modules upon request;

- **Trigger Processor Units (TPUs):** The TPUs analyze time windows in reduced data, searching for possible events by applying several trigger algorithms. The simplest trigger, which is the one used in this study, is the *NDigits* or *Simple Majority*: if the number of hits in a sliding time window meets a threshold an event is tagged. This is a trigger suitable for high-events but low-energy events require a more complex approach to cope with the unavoidable dark-noise hits. The Vertex Reconstruction trigger exploits the fact that a low-energy lepton travels only a few centimeters in water before its energy falls below Cherenkov threshold, so its track can be approximated as a point-like source that emits all Cherenkov photons at the same time and from the same position. This algorithm uses a uniformly spaced three-dimensional grid of test vertices inside the tank. For each vertex it corrects the recorded hit times by the time-of-flight and applies an *NDigits* trigger with a reduced time window of 20 ns. If the test vertex is close to the true vertex of an event a narrow peak is produced while dark noise remains randomly distributed.

All triggers are software-based, so they can be updated;

- **Event Builder Units (EBUs):** once a TPU has identified an event it requests an EBU to associate data from the RBUs with event timestamps. The EBU retrieves relevant data and stores them to disk for long-time preservation;
- **brokers:** two identical machines act as brokers, balancing load to TPUs and EBUs, managing failing modules for seamless detector operation.

6.2 HK data

For this study in Hyper-Kamiokande we used a simulated proton decay $p \rightarrow e^+ \pi^0$ sample: here we describe the steps followed to generate it and the tools used for this purpose.

6.2.1 Proton decay kinematics

Free protons decay back-to-back into a positron and a neutral pion, each carrying a momentum of 459 MeV/c (Figure 6.8). Then neutral pions promptly ($\sim 10^{-16}$ s) decay into two photons in 98.8% of the times.

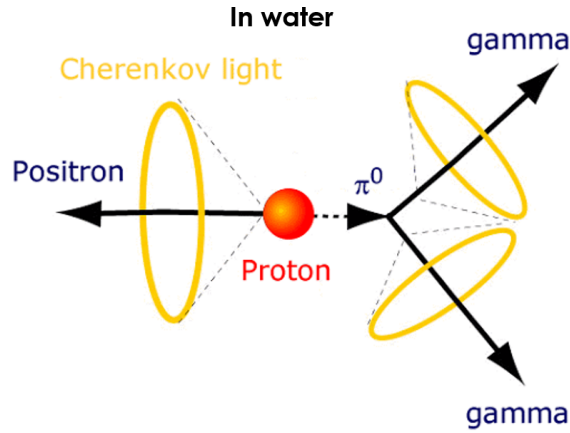


Figure 6.8: $p \rightarrow e^+ \pi^0$ free proton decay scheme.

In the final state we expect three well visible e-like rings and well defined kinematics: this is the reason why we chose this decay mode for our preliminary study.

For the decay of protons bound in Oxygen nuclear effects and pion FSI must be considered as explained in Section 3.4: since this complicates the final states, we restrict this preliminary study to free proton decays only.

6.2.2 Proton decay event generation

We generated proton decay events using NEUT [36] with primary vertexes uniformly distributed inside the ID volume with a true distance from its wall (d_{wall}) > 100 cm (Figure 6.9), to improve our statistics and to avoid non physical simulation: events too close to the wall with light produced towards it would have required the simulation of PMT saturation, which was not implemented yet.

We generated 10000 events, of which 1942 (19.42%) are free proton decays. Table 6.1 shows the breakdown of final states in the events. While the positron always escapes the Oxygen nucleus, the neutral pion undergoes nuclear effects (FSI), as explained in Section 3.2.1, that produce different meson configurations in the final state for bound proton decays.

Figure 6.10 shows true momentum distributions for positron and neutral pion in events with true final state $e^+ \pi^0$ for both free and bound proton decays. The distributions agree with the expected shapes and values: while momentum distributions of free proton decay products are monochromatic, in the case of bound protons the decay products carry part of the nuclear momentum of their parent which broadens their momentum distributions.

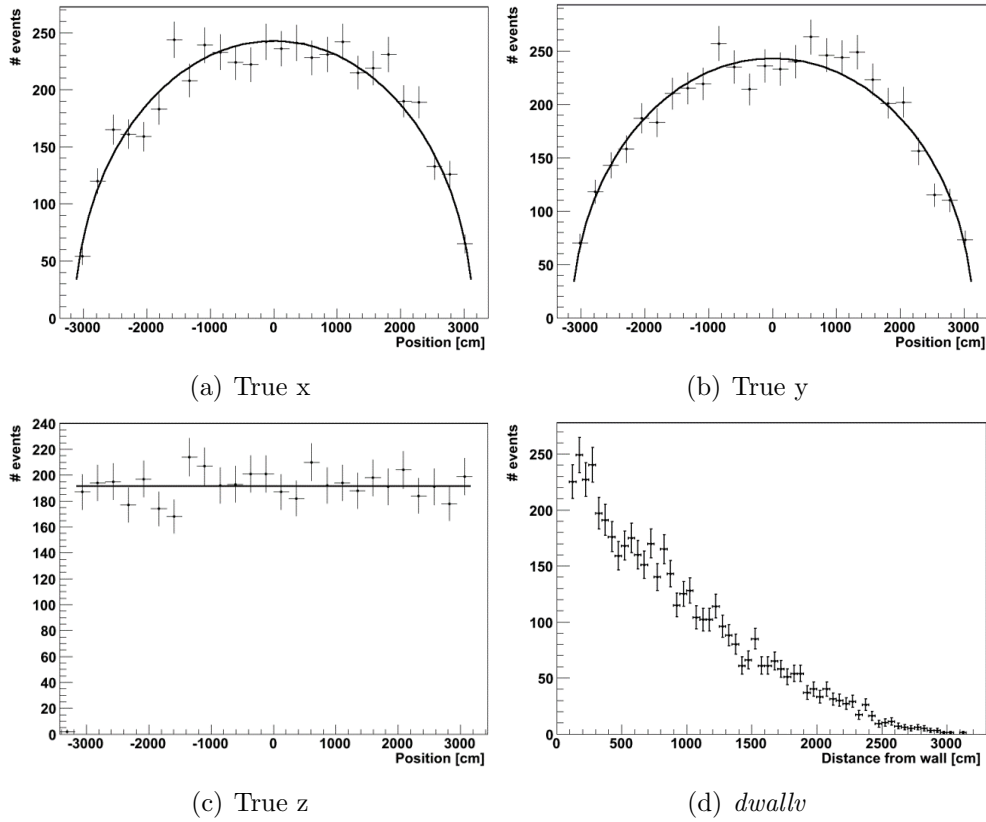


Figure 6.9: True proton decay vector primary vertex coordinates distributions and true distance from ID wall distributions (d_{wall}). The black solid lines show the expected coordinates distributions assuming uniform primary vertex generation in the ID volume with $d_{wall} > 100$ cm.

In the case of neutral pions from bound proton decays a minor peak in momentum distribution is due to scattering with nucleons.

Figure 6.11 shows the true cosine of the opening angle between positron and neutral pion in proton decay vectors after nuclear effects for both free and bound proton case. The distributions agree with the expected shapes and values: in the free proton case the opening angle is exactly 180° , as expected for a two body decay at rest, while in the bound proton case the opening angle is less than 180° due to the conservation of the parent proton momentum.

Table 6.1: Breakdown of $p \rightarrow e^+\pi^0$ events final states after nuclear effects.

	Total # events	10000
	Free protons	1942
Breakdown:	$e^+\pi^0$	1942
	Bound protons	8058
Breakdown:	$e^+\pi^0$	4713
	e^+	1814
	$e^+\pi^-$	759
	$e^+\pi^+$	740
	$e^+\pi^0\pi^+$	8
	$e^+\pi^0\pi^-$	5
	$e^+\pi^+\pi^-$	5
	$e^+\pi^0\pi^+\pi^-$	4
	$e^+\pi^0\pi^0$	4
	$e^+\pi^0\pi^0\pi^-$	2
	$e^+\pi^+\pi^-\pi^-$	2
	$e^+\pi^+\pi^+$	1
	$e^+\pi^-\pi^-$	1

6.2.3 Detector simulation

The Water Cherenkov Simulation (WCSim) package is a flexible, Geant4-based code that is designed to simulate the geometry and physics response of user-defined water Cherenkov detector configurations [11]. Geant4 [20] is used to track the particles as they pass through the detector and compute the final deposited energy. Geant4 also simulates Secondary Interactions (SI) of particles in water, their decays and Cherenkov light emission, in particular. Particles that reach photodetector glass and pass the quantum efficiency and collection efficiency thresholds are registered as a hit. WCSim implements both B&L PMTs and mPMTs and simulates electronics response to photodetector hits: each event contains information about hits before (*raw*) and after (*digitized*) front-end electronics simulation for both photodetector types.

We used WCSim to generate one proton decay sample for each of the following configurations from the events we generated:

- **20kBL**
- **20kBL+10kmPMT**

as defined in Section 6.1.3.

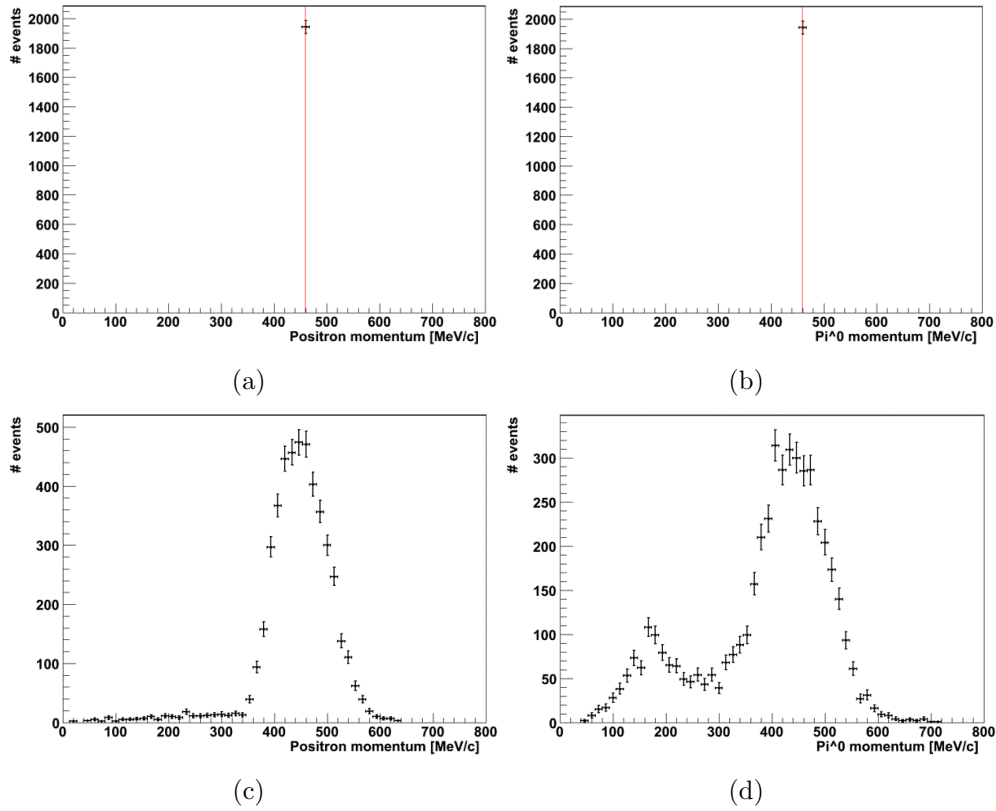


Figure 6.10: True positron (left) and neutral pion (right) momentum distributions for free proton (top) and bound proton (bottom) proton decay vectors with true $e^+\pi^0$ final state after nuclear effects. The vertical red line shows the expected momentum value in the free proton case of 459 MeV/c.

6.2.4 Reconstruction

The reconstruction algorithm for HK is *fiTQun*: the version we used was still in development and for this reason it had four main important limitations with respect to *fiTQun* for SK:

- the maximum number of rings per multi-ring events is 4, instead of 6, to save computational time during development;
- the prediction of charge from indirect light (Section 4.3.2) was not implemented;
- no ring correction algorithm to reject fake rings is applied;
- no refitting of the selected hypothesis is performed, thus all the rings in one event share the same reconstructed vertex.

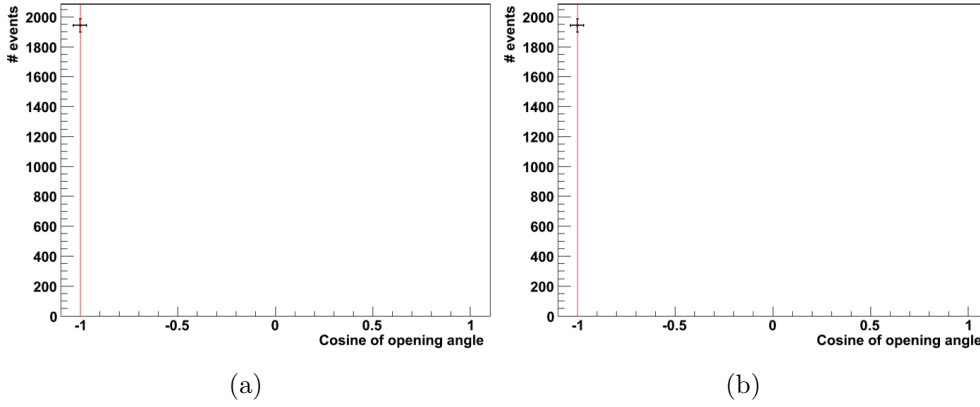


Figure 6.11: True cosine of the opening angle between positron and neutral pion for free proton (left) and bound proton (right) proton decay vectors with true $e^+\pi^0$ final state after nuclear effects. The vertical red line shows the expected cosine value for the free proton case of -1, corresponding to a back-to-back two body decay.

We applied the same version of *fiTQun* to reconstruct both samples.

6.3 First study: *fiTQun* performance

We studied the signal selection efficiency for proton decay $p \rightarrow e^+\pi^0$ search for both 20kBL and 20kBL+10kmPMT configurations. The reference studies in Super-Kamiokande for this decay mode are [56] and [41].

For this preliminar study we used the Ea_0 , Mua_0 and a_1 multi-ring fitter ring counting parameters (see Section 4.3.9) obtained from the tuning for Long Baseline neutrino analysis. A tuned a_0 parameter was not available, so we set it to the same value as Ea_0 in both configurations. All values are shown in Table 6.2.

Table 6.2: Multi-ring fitter ring counting parameters used for both 20kBL and 20kBL+10kmPMT configurations.

Configuration	Ea_0	Mua_0	a_0	a_1
20kBL	167.5	167.5	167.5	1.65
20kBL+10kmPMT	227.5	227.5	227.5	1.55

6.3.1 Event selections

We apply the same event selections as those in [56], except for FC reduction, since the OD is not simulated in our samples, and neutron tagging, for the same reason:

1. **FV**: Distance of reconstructed vertex from wall $d_{wall} > 150$ cm,
2. **nring**: 2 or 3 reconstructed rings,
3. **PID**: all reconstructed rings are e-like,
4. **micHEL**: no *Michel electrons* tagged,
5. **M_{π⁰}**: reconstructed π^0 mass is between $85 \text{ MeV}/c^2$ and $185 \text{ MeV}/c^2$ for 3-ring events,
6. **M_{tot}**: total reconstructed invariant mass is between $830 \text{ MeV}/c^2$ and $1050 \text{ MeV}/c^2$,
7. **P_{tot}**: total reconstructed momentum is below $250 \text{ MeV}/c$.

6.3.2 Distributions along cut parameters

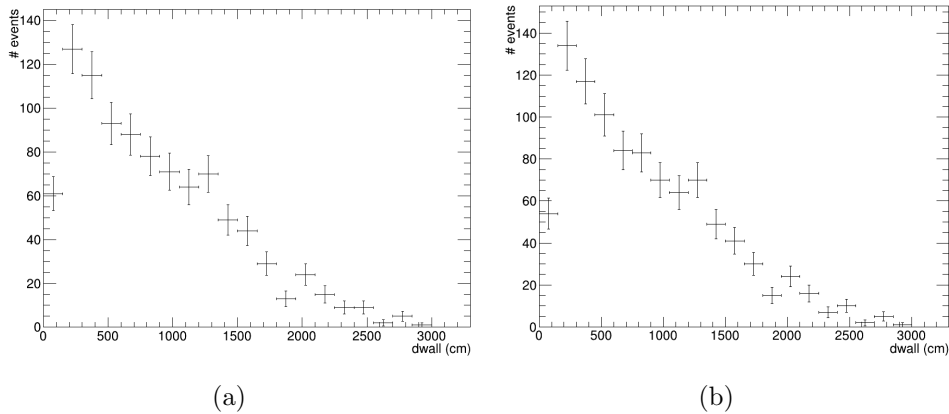


Figure 6.12: Reconstructed distance of primary vertex from ID wall distributions for free proton decay samples $p \rightarrow e^+ \pi^0$ events in 20kBL (left) and 20kBL+10kPMT (right) configurations.

Figures from 6.12 to 6.18 show distributions along cut parameters for both 20kBL and 20kBL+10kPMT configurations.

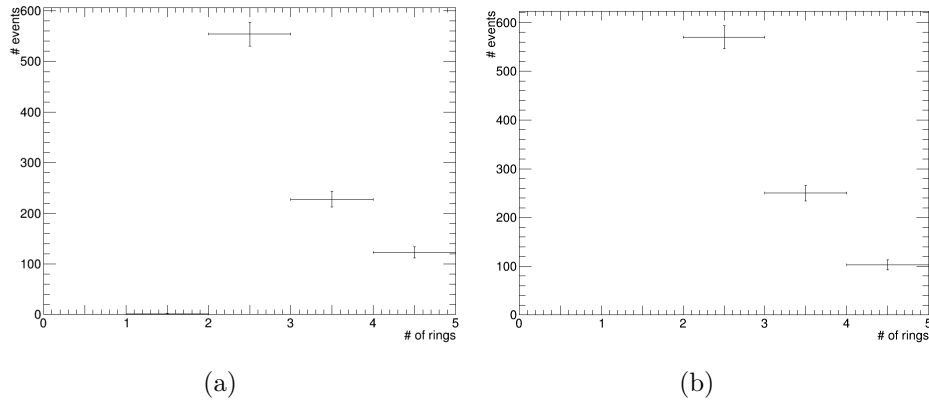


Figure 6.13: Number of reconstructed rings distributions for free proton decay $p \rightarrow e^+\pi^0$ samples in 20kBL (left) and 20kBL+10kmPMT (right) configurations, after **FV** cut.

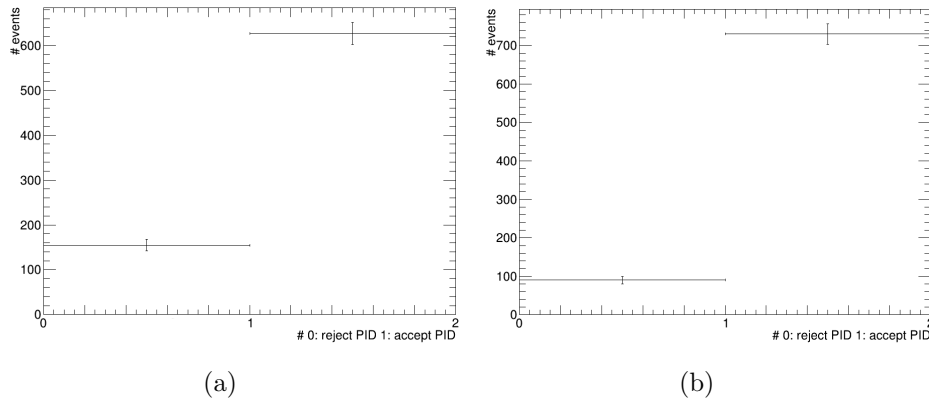


Figure 6.14: PID distributions for free proton decay $p \rightarrow e^+\pi^0$ samples in 20kBL (left) and 20kBL+10kmPMT (right) configurations, after **FV** and **nring** cuts.

By comparing the distributions of the number of reconstructed rings for free proton decays from the reference study [56] (Figure 6.19) and this study (Figure 6.13), we can spot an important discrepancy: in the reference study the fraction of 3-ring events before ring correction dominates (68.9%), as expected since three rings should be visible in each free proton event while in this study the 2-ring events fraction dominates instead in both 20kBL (24.4%) and 20kBL+10kmPMT (26.6%) configurations. This effect is the subject of the second preliminary study we performed (Section 6.4).

Reconstructed π^0 mass fitted values for 20kBL and 20kBL+10kmPMT configurations are 1.9% and 3.1% higher than the expected value of 135.0

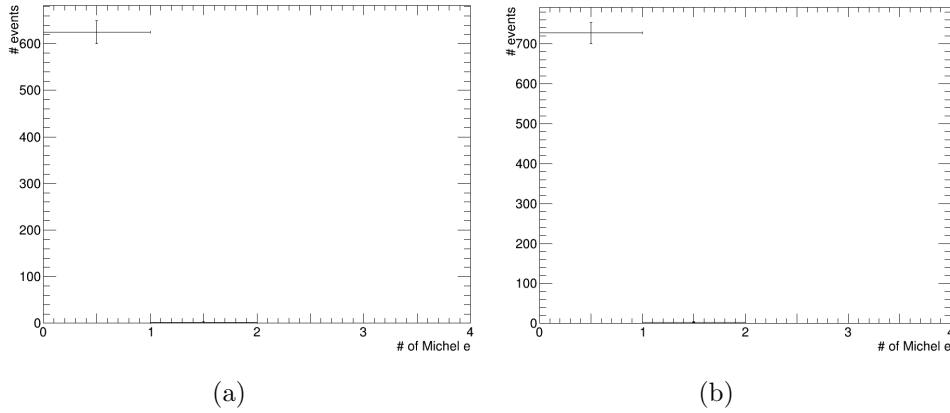


Figure 6.15: Counted Michel electrons distributions for free proton decay $p \rightarrow e^+ \pi^0$ samples in 20kBL (left) and 20kBL+10kmPMT (right) configurations, after **FV**, **nring** and **PID** cuts.

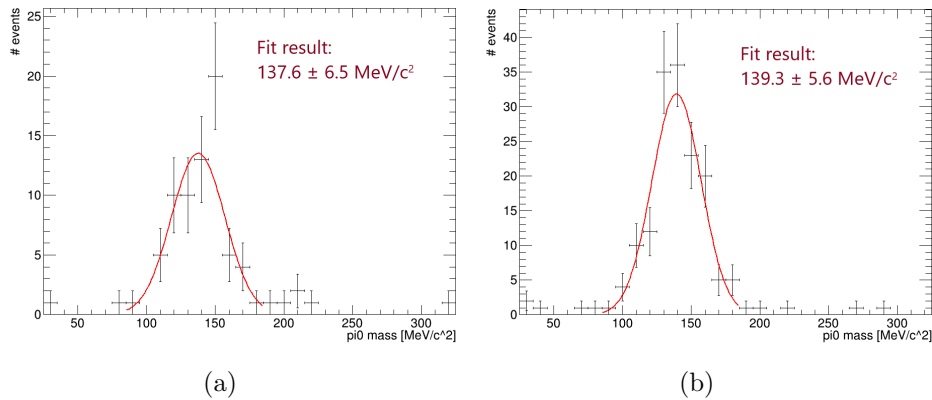


Figure 6.16: Reconstructed π^+ mass (M_{π^+}) distributions for free proton decay $p \rightarrow e^+ \pi^0$ samples in 20kBL (left) and 20kBL+10kmPMT (right) configurations, after **FV**, **nring**, **PID** and **michel** cuts.

MeV/c² but still compatible with it within statistical error. Reconstructed total mass fitted values for 20kBL and 20kBL+10mPMT are significantly higher than the expected value of 938.3 MeV/c² by 4.2% and 4.4% respectively.

6.3.3 Results

Table 6.3 summarizes signal selection efficiencies η along cuts for both 20kBL and 20kBL+10mPMT configurations.

Signal selection efficiency for the configuration with mPMTs is signifi-

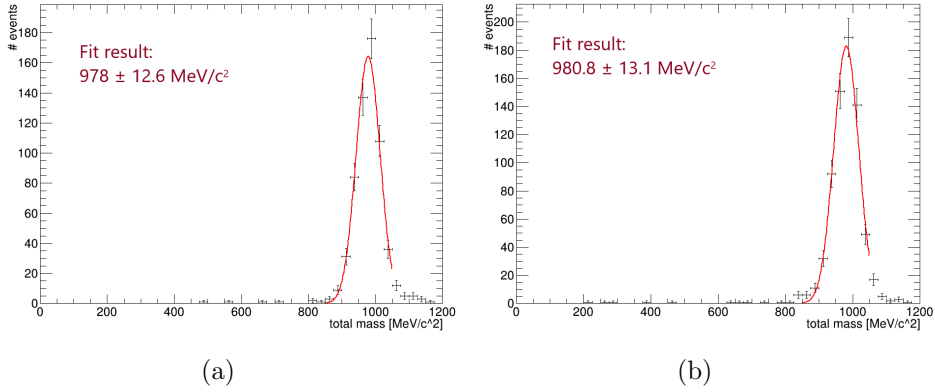


Figure 6.17: Total reconstructed mass (M_{tot}) distributions for free proton decay $p \rightarrow e^+\pi^0$ samples in 20kBL (left) and 20kBL+10kmPMT (right) configurations, after **FV**, **nring**, **PID**, **micel** and M_{π^+} cuts.

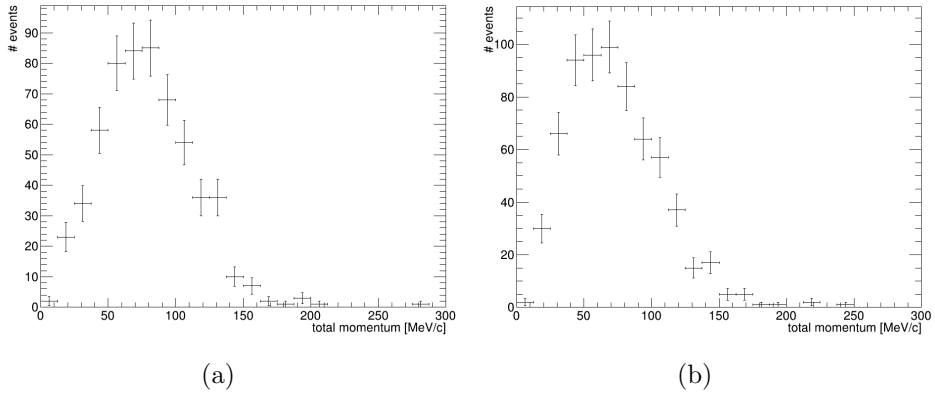


Figure 6.18: Total reconstructed momentum (P_{tot}) distributions for free proton decay $p \rightarrow e^+\pi^0$ samples in 20kBL (left) and 20kBL+10kmPMT (right) configurations, after **FV**, **nring**, **PID**, **micel**, M_{π^+} and M_{tot} cuts.

cantly higher than that of the one without, even if well below the signal selection efficiency for the free proton case 85% from the reference study [56].

Figure 6.20 shows signal selection efficiencies for both configurations as a function of true distance of primary vertex from the ID wall: signal selection efficiency for the configuration with mPMTs is significantly higher than that of the configuration with BL PMTs only in the region closest to ID wall. This hints that, as expected, the addition of mPMTs improves performance of events close to the wall.

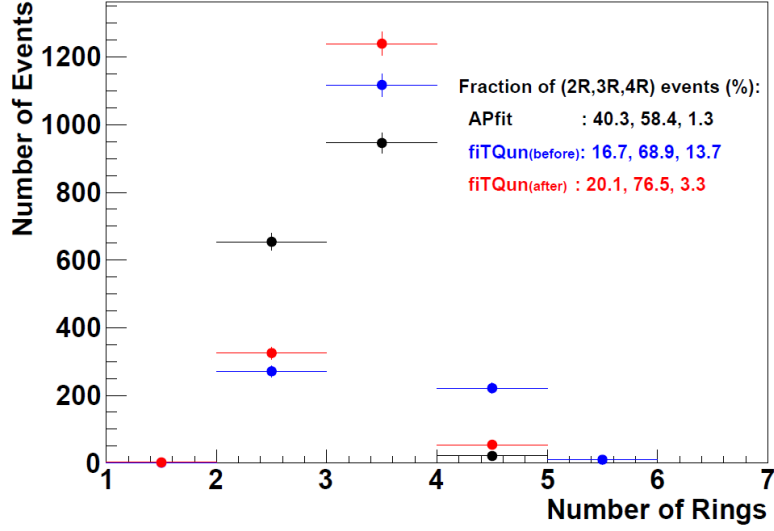


Figure 6.19: Number of reconstructed rings distributions for proton decay $p \rightarrow e^+ \pi^0$ MC sample from reference study [56] in Super-Kamiokande, reconstructed with *APFit* (black) and with *fiTQun* before (blue) and after (red) ring correction.

Table 6.3: Signal efficiency, remaining background and remaining data events after each cut

Cuts	$\eta_{20\text{kBL}}$ (%)	$\eta_{20\text{kBL}+10\text{kmPMT}}$ (%)
FV	97.8 ± 0.5	98.9 ± 0.3
+nring	84.4 ± 1.2	87.9 ± 1.1
+PID	67.7 ± 1.5	78.2 ± 1.3
+michel	67.5 ± 1.5	77.9 ± 1.3
+ M_{π^0}	66.6 ± 1.5	76.7 ± 1.4
+ M_{tot}	63.2 ± 1.6	72.4 ± 1.5
+ P_{tot}	63.1 ± 1.6	72.4 ± 1.5

6.4 Second study: tuning of *fiTQun* ring counting for proton decay

In the first preliminary study we performed (Section 6.3), we found that the fraction of $p \rightarrow e^+ \pi^0$ MC events with 2 reconstructed rings is dominant while according to expectations and the reference study [56] the dominant fraction should be that of events with 3 reconstructed rings.

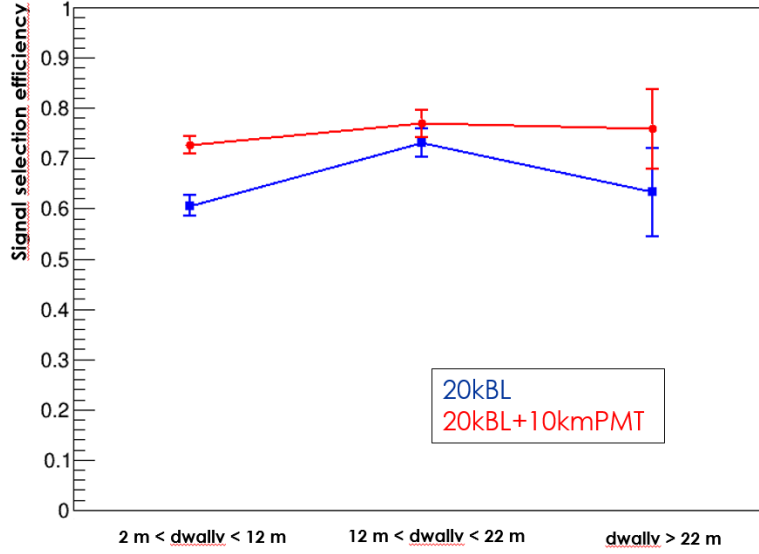


Figure 6.20: Signal selection efficiencies for $p \rightarrow e^+ \pi^0$ samples in both 20kBL (blue) and 20kBL+10kmPMT (red) as a function of true distance of primary vertex from the ID wall (d_{wall}) ranges.

We tuned the a_0 *fiTQun* ring counting parameter in order to maximize the 3-ring event fraction in both 20kBL and 20kBL+10kmPMT configurations: its value rules ring counting for a number of reconstructed rings greater than one, as explained in Section 4.3.9. We kept the other *fiTQun* ring counting parameters from the previous study.

The tuning plots are shown in Figure 6.21: the optimal values for a_0 are 43 for 20kBL and 44 for 20kBL+10kmPMT, the distributions of the number of reconstructed rings with these preliminary optimized a_0 values are shown in Figure 6.22).

The expected 3-ring events fraction is 68.9% (Figure 6.19). The fractions obtained from our optimization procedure are 57.6% for 20kBL and 60.5% for 20kBL+10kmPMT, both dominant but still lower than expected.

Moreover, the 4-ring events fractions are 23.9% for 20kBL and 23.4% for 20kBL+10kmPMT, both higher than 13.7% as in the reference. In this study *fiTQun* doesn't consider indirect light contribution: there is no easy way to estimate its impact and to understand if it can explain these differences.

For this reason we tried to estimate how much the 4-ring fractions could be reduced by applying the ring correction from the reference study by hand.

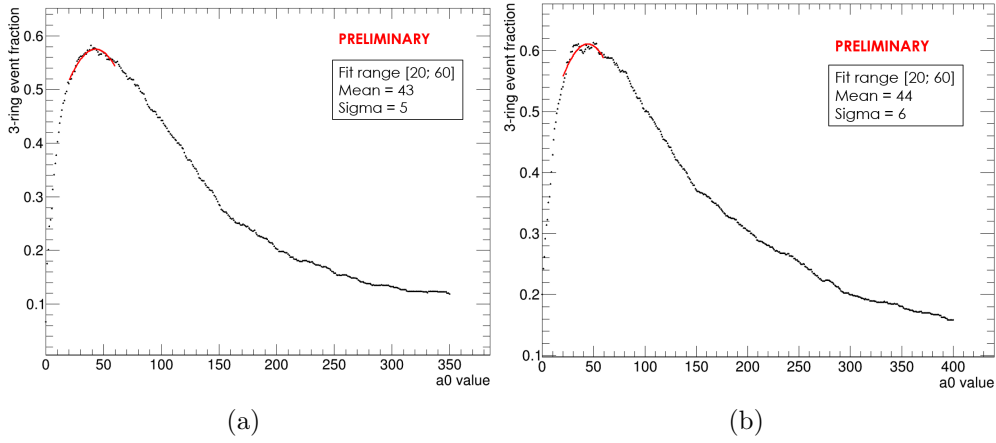


Figure 6.21: Fraction of free proton $p \rightarrow e^+\pi^0$ MC events with 3 reconstructed rings, after **FV** cut, as a function of $fiTQun$ ring counting parameter a_0 in both 20kBL (left) and 20kBL+20kmPMT (right) configurations. The red solid lines show gaussian fits of the peaks.

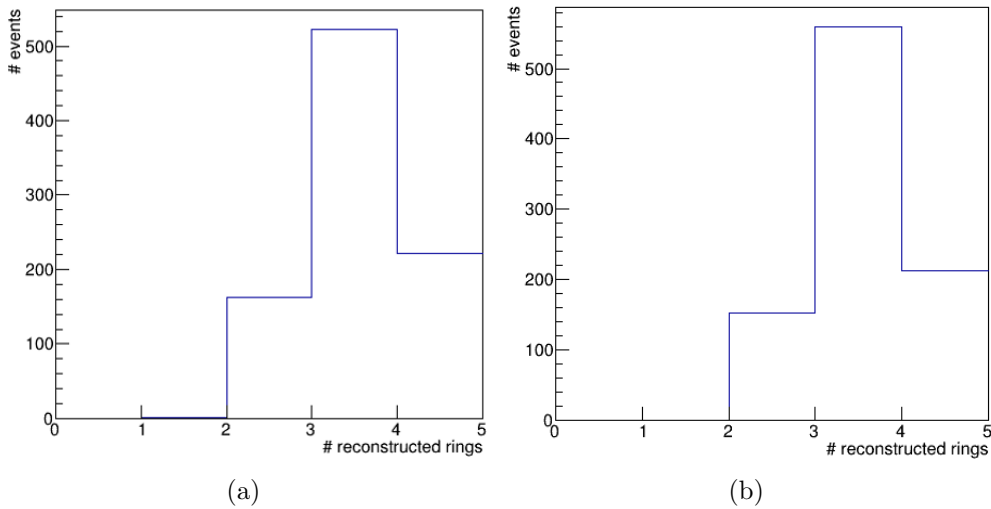


Figure 6.22: Distributions of the number of reconstructed rings in $p \rightarrow e^+\pi^0$ MC events, after **FV** cut, in both 20kBL with (left) and 20kBL+10kmPMT (right) configurations, using a_0 values that maximize the 3-ring events fractions.

6.4.1 Manual check of ring correction

The ring correction algorithm from the reference study works by merging the most energetic reconstructed ring with the closest ring within 20° from its reconstructed direction.

We manually scanned 5 events with 4 reconstructed rings and checked if they can trigger this algorithm: 1/5 events would trigger it bringing a reduction of $20\% \pm 18\%$, which is not sufficient to explain the excess of 4 ring events.

6.4.2 Results

We found the preliminar optimal value for the *fiTQun* ring counting parameter a_0 for $p \rightarrow e^+\pi^0$, in both 20kBL and 20kBL+10kmPMT configurations. We still see a significant excess of events with 4 reconstructed rings that can't be fixed by tuning and that is only partially explained by the absence of a ring correction algorithm.

Conclusions

We searched for proton decay $p \rightarrow \nu K^+$ in 3244.4 days of data acquired by the Super-Kamiokande experiment equivalent to an exposure of 200 kton*year: we found no data candidates. The *fiTQun* reconstruction algorithm enabled us to successfully reconstruct kaon kinematics and to develop a low-background analysis. Finally, we checked *fiTQun* performance in reconstructing proton decay $p \rightarrow e^+ \pi^0$ events in Hyper-Kamiokande. We found that the introduction of multi-PMT photosensors significantly improves selection efficiency. Finally, we tuned *fiTQun* ring counting parameters: we found a significant excess of events with 4 reconstructed rings which deserves further investigation in the future.

Bibliography

- [1] *Geant3, CERN-DD-EE-84-1.*
- [2] S.M. Bilenky and B. Pontecorvo. Lepton mixing and neutrino oscillations. *Physics Reports*, 1978.
- [3] P. A. Cherenkov. Visible emission of clean liquids by action of γ radiation. *Doklady Akademii Nauk SSSR*, 1934.
- [4] M. K. Parida D. Lee, R. N. Mohapatra and M. Rani. Predictions for proton lifetime in minimal nonsupersymmetric so(10) models: An update. *Phys. Rev. D*, 1995.
- [5] P. de Perio. Neut pion final state interactions. In *AIP Conf. Proc.*
- [6] A. Einstein. Ueber einen die erzeugung und verwandlung des lichtetes betreffenden heuristischen gesichtspunkt. *Annalen der Physik*, 1905.
- [7] A. Suzuki et al. Improvement of 20-inch diameter photomultiplier tubes. *Nucl. Instrum. Meth. A*, 1999.
- [8] G. Aad et al. Observation of a new particle in the search for the standard model higgs boson with the atlas detector at the lhc. *Phys. Rev. Lett.*, 2016.
- [9] H. Ikeda et al. Front end hybrid circuit for super-kamiokande. *Nucl. Instrum. Meth. A*, 1992.
- [10] H. Nishino et al. High-speed charge-to-time converter asic for the super-kamiokande detector. *Nucl. Instrum. Meth. A*, 2009.
- [11] Hyper-Kamiokande Proto-Collaboration: K. Abe et al. Hyper-kamiokande design report. Technical report, 2018.
- [12] K. Abe et al. Calibration of the super-kamiokande detector. *Nucl. Instrum. Meth. A*, 2014.

- [13] K. Nakamura et al. The reaction $c-12$ ($e, e' p$) at 700-mev and dwia analysis. *Nucl. Phys. A*, 1976.
- [14] M. Honda et al. Calculation of the flux of atmospheric neutrinos. *Phys. Rev. D*, 1995.
- [15] M. Honda et al. Calculation of atmospheric neutrino flux using the interaction model calibrated with atmospheric muon data. *Phys. Rev. D*, 2007.
- [16] M. Honda et al. Improvement of low energy atmospheric neutrino flux calculation using the jam nuclear interaction model. *Phys. Rev. D*, 2011.
- [17] M. Tanabashi et al. Particle data group. *Phys. Rev. D*, 2018.
- [18] R. Becker-Szendy et al. Imb-3: A large water cherenkov detector for nucleon decay and neutrino interactions. *Nucl. Instrum. Meth. A*, 1993.
- [19] R.W. Bland et al. The k^+p interaction from 864 to 1585 mev/c: Cross sections and mass distributions. *Nuclear Physics*, 1969.
- [20] S. Agostinelli et al. The super-kamiokande detector. *Nuclear Instruments and Methods in Physics Research A*, 2003.
- [21] S. Chatrchyan et al. Observation of a new boson at a mass of 125 gev with the cms experiment at the lhc. *Phys. Lett. B*, 2012.
- [22] S. Fukuda et al. The super-kamiokande detector. *Nuclear Instruments and Methods in Physics Research A*, 2003.
- [23] S. Jadach et al. The tau decay library tauola: Version 2.4. *Comput. Phys. Commun.*, 1993.
- [24] U. Amaldi et al. Comparison of grand unified theories with electroweak and strong coupling constants measured at lep. *Phys. Lett.*, 1991.
- [25] Y. Ashie et al. A measurement of atmospheric neutrino oscillation parameters by super-kamiokande i. *Physical Review D*, 2005.
- [26] C. McGrew et al. (IMB Collaboration). Search for nucleon decay using the imb-3 detector. *Phys. Rev. D*, 1999.
- [27] K. S. Hirata et al. (Kamiokande Collaboration). Experimental limits on nucleon lifetime for lepton + meson decay modes. *Phys. Lett. B*, 1989.

- [28] K. Eguchi et al. (KamLAND Collaboration). First results from kamland: evidence for reactor antineutrino disappearance. *Phys. Rev. Lett.*, 2003.
- [29] Q. R. Ahmad et al. (SNO Collaboration). Direct evidence for neutrino flavor transformation from neutral-current interactions in the sudbury neutrino observatory. *Phys. Rev. Lett.*, 2002.
- [30] H. Nishino et al. (Super-Kamiokande Collaboration). Search for proton decay via $p \rightarrow e^+\pi^0$ and $p \rightarrow \mu^+\pi^0$ in a large water cherenkov detector. *Phys. Rev. Lett.*, 2009.
- [31] M. Shiozawa et al. (Super-Kamiokande Collaboration). Search for proton decay via $p \rightarrow e^+\pi^0$ in a large water cherenkov detector. *Phys. Rev. Lett.*, 1998.
- [32] Y. Fukuda et al. (Super-Kamiokande Collaboration). Evidence for oscillation of atmospheric neutrinos. *Phys. Rev. Lett.*, 1998.
- [33] C. L. Cowan F. Reines and M. Goldhaber. Conservation of the number of nucleons. *Phys. Rev.*, 1954.
- [34] H. Georgi and S. L. Glashow. Unity of all elementary particle forces. *Phys. Rev. Lett.*, 1974.
- [35] Jeffrey D. Gustafson. *A search for baryon number violation by two units at the Super-Kamiokande detector*. PhD thesis, Boston University, Graduate School of Arts and Sciences, 2016.
- [36] Y. Hayato. A neutrino interaction simulation program library neut. In *Acta Phys. Polon.*
- [37] T. J. Irvine. *Development of Neutron-Tagging Techniques and Application to Atmospheric Neutrino Oscillation Analysis in Super-Kamiokande*. PhD thesis, University of Tokyo, 2014.
- [38] F. Reines J. Learned and A. Soni. Limits on nonconservation of baryon number. *Phys. Rev. Lett.*, 1979.
- [39] S. Kelley J. R. Ellis and D. V. Nanopoulos. Implications of precision electroweak experiments for m_t , ρ_0 , $\sin^2(\theta_w)$ and grand unification. *Phys. Rev. D*, 1991.
- [40] The Super-Kamiokande collaboration K. Abe et al. Search for proton decay via $p \rightarrow \nu k^+$ using 260 kiloton-year data of super-kamiokande. *Phys. Rev. D*, 2014.

- [41] The Super-Kamiokande collaboration K. Abe et al. Search for proton decay via $p \rightarrow e^+ \pi^0$ and $p \rightarrow \mu^+ \pi^0$ in 0.31 megaton*years exposure of the super-kamiokande water cherenkov detector. *Phys. Rev. D*, 2017.
- [42] B. Bajc K. S. Babu and Z. Tavartkiladze. *Phys. Rev. D*, 2012.
- [43] J. C. Pati K. S. Babu and Z. Tavartkiladze. *JHEP*, 2010.
- [44] P. Langacker and M. Luo. Probing the desert using gauge coupling unification. *Phys. Lett.*, 1991.
- [45] P. Langacker and N. Polonsky. Uncertainties in coupling constant unification. *Phys. Rev. D*, 1993.
- [46] V. Lucas and S. Raby. *Phys. Rev. D*, 1997.
- [47] P. Ramond M. Gell-Mann and R. Slansky. Complex spinors and unified theories. *Conf. Proc.*, 1979.
- [48] Lucas Machado. *Pre-supernova alert system for Super-Kamiokande with gadolinium*. PhD thesis, University of Naples Federico II, 2021.
- [49] P. Minkowski. $\mu \rightarrow e\gamma$ at a rate of one out of 10^9 muon decays? *Phys. Lett. B*, 1977.
- [50] G. Mitsuka. “*Study of Non-Standard Neutrino Interactions with Atmospheric Neutrino Data in Super-Kamiokande*”. PhD thesis, University of Tokyo, 2009.
- [51] H. Murayama and A. Pierce. Not even decoupling can save minimal supersymmetric su(5). *Phys. Rev. D*, 2002.
- [52] Euan Richard. *Studies of the energy, azimuthal, and time spectra of the atmospheric neutrino flux at Super-Kamiokande*. PhD thesis, University of Tokyo, 2015.
- [53] N. T. Shaban and W. James Stirling. Minimal left-right symmetry and so(10) grand unification using lep coupling constant measurements. *Phys. Lett. B*, 1992.
- [54] M. Shiozawa. Reconstruction algorithms in the super-kamiokande large water cherenkov detector. *Nucl. Instrum. Meth. A*, 199.
- [55] T. Sjostrand. Pythia 5.7 and jetset 7.4 physics and manual. 1994.

- [56] Yusuke Suda. *Search for Proton Decay Using an Improved Event Reconstruction Algorithm in Super-Kamiokande*. PhD thesis, University of Tokyo, 2017.
- [57] San Diego Surface Optics Corp. Report no. soc-r950- 001-0195. Technical report, 1995.
- [58] Y. Akaishi T. Yamazaki. Nuclear medium effects on invariant mass spectra of hadrons decaying in nuclei. *Physics Letters B*, 1999.
- [59] Yumiko Takenaga. *Atmospheric neutrino oscillation analysis with solar terms in Super-Kamiokande*. PhD thesis, University of Tokyo, 2008.
- [60] Akira Takenaka. *Search for Proton Decay via $p \rightarrow e^+ \pi^0$ and $p \rightarrow \mu^+ \pi^0$ with an Enlarged Fiducial Mass of the Super-Kamiokande Detector*. PhD thesis, University of Tokyo, 2020.
- [61] Y. Fukuda et al. The Super-Kamiokande collaboration. Evidence for oscillation of atmospheric neutrinos. *Phys.Rev.Lett.*, 1998.
- [62] Shinpei Tobayama. *An Analysis of the Oscillation of Atmospheric Neutrinos*. PhD thesis, University of British Columbia (Vancouver), 2016.
- [63] R.D. Woods and D.S. Saxon. Diffuse surface optical model for nucleon-nuclei scattering. *Phys. Rev.*, 1954.
- [64] T. Yanagida. Horizontal symmetry and masses of neutrinos. *Prog. Theor. Phys.*, 1980.
- [65] C. Zeitnitz and T.A. Gabriel. The geant-calor interface and benchmark calculations of zeus test calorimeters. *Nucl. Instrum. Meth. A*, 1994.